

Gravitational wave sources in the era of multi-frequency gravitational wave astronomy

Monica Colpi^{1,2,*}, Alberto Sesana^{3,†}

¹ Dipartimento di Fisica G. Occhialini, Università degli Studi di Milano Bicocca,
Piazza della Scienza 3, I-20126 Milano, Italy

² INFN, Sezione di Milano-Bicocca, Piazza della Scienza 3, I-20126 Milano, Italy

³ School of Physics and Astronomy, The University of Birmingham, Edgbaston,
Birmingham B15 2TT, UK

to appear in the book

*An Overview of Gravitational Waves:
Theory, Sources and Detection*

edited by G. Auger and E. Plagnol (World Scientific, 2016)

* email: Monica.Colpi@mib.infn.it

† email: asesana@star.sr.bham.ac.uk

Contents

1 Key science objectives of the multi-band gravitational wave astronomy	2
2 Prologue: GW150914 - the first cosmic source of gravitational waves	5
3 A new cosmic landscape	7
3.1 Black holes, neutron stars and supermassive stars as basic equilibrium objects	8
3.2 Gravitational wave sources: a first glimpse	14
4 The electromagnetic universe	16
4.1 Neutron stars and stellar origin black holes in the realm of observations	16
4.2 Forming stellar origin compact binaries	19
4.3 Massive black holes in the realm of observations	23
4.4 The black hole desert	27
4.5 Formation of gravitational wave sources: the cosmological perspective	31
4.6 Massive black hole binary mergers across cosmic ages	33
4.6.1 Reconstructing the cosmic evolution of massive black hole binary coalescences across the ages	36
5 The sources of the gravitational wave universe	37
5.1 The high frequency gravitational universe	37
5.2 The low frequency gravitational universe	42
5.3 The very low frequency gravitational universe	48
6 Binaries as key sources of the gravitational universe	50
6.1 Description of the inspiral	51
6.2 Spin effects in black hole binary inspirals	60
6.3 Gravitational recoil	62
6.4 Modelling the final spin and mass of coalescing black holes	64
7 Waveforms and the Laws of Nature	68
7.1 Black hole binary coalescences	69
7.2 Extreme Mass Ratio Inspirals	70
7.3 Neutron star binary coalescences	71
7.4 Electromagnetic counterparts of CBCs	74
7.5 Core-collapse supernovae	78
7.6 Signal from a cosmological background of supermassive black holes	78
8 Conclusion	82

Abstract

The focus of this Chapter is on describing the prospective sources of the gravitational wave universe accessible to present and future observations, from kHz, to mHz down to nano-Hz frequencies. The multi-frequency gravitational wave universe gives a deep view into the cosmos, inaccessible otherwise. It has as main actors core-collapsing massive stars, neutron stars, coalescing compact object binaries of different flavours and stellar origin, coalescing massive black hole binaries, extreme mass ratio inspirals, and possibly the very early universe itself. Here, we highlight the science aims and describe the gravitational wave signals expected from the sources and the information gathered in it. We show that the observation of gravitational wave sources will play a transformative role in our understanding of the processes ruling the formation and evolution of stars and black holes, galaxy clustering and evolution, the nature of the strong forces in neutron star interiors, and the most mysterious interaction of Nature: gravity. The discovery, by the LIGO Scientific Collaboration and Virgo Collaboration, of the first source of gravitational waves from the cosmos GW150914, and the superb technological achievement of the space mission LISA Pathfinder herald the beginning of the new phase of exploration of the universe.

1 Key science objectives of the multi-band gravitational wave astronomy

Gravitational wave sources have been anticipated and studied in the literature quite extensively during the last twenty years. These studies flourished in parallel to the building on Earth of the interferometric detectors Advanced LIGO and Virgo designed to explore the high frequency gravitational wave universe, and the proposal to construct in space a Laser Interferometer Space Antenna (LISA) to investigate lower frequency sources. The Pulsar Timing Array experiment (PTA) has been joining this world-wide effort by exploiting millisecond pulsars as high precision clocks to investigate the very low frequency domain.

With time, it has become clear that exploring the universe with gravitational waves from kHz to nano Hz makes it possible to discover new sources never anticipated before, and to provide complementary avenues for expanding our knowledge on the *Laws of Nature*, on *Cosmology*, and on the processes ruling the formation and evolution of compact objects as black holes within the realm of *Relativistic Astrophysics* and *Galaxy Structure Formation*. Exploring the universe with gravitational waves will help answering a number of fundamental questions in all these domains:

Laws of Nature

- Is gravity in the strong field regime and dynamical sector as predicted by

Einstein's theory?

- Are the properties of gravitational radiation as predicated by Einstein's theory?
- Does gravity couple to other dynamical fields, such as, massless or massive scalars?
- Are (astrophysical) black holes described by the Kerr metric?
- Are black holes hairless?
- Are there naked singularities?
- What is the behaviour of the short-range interaction at supra-nuclear densities?
- What is the lowest energy state of baryonic matter at supra-nuclear densities?
- Is gravitational collapse to a Kerr black hole unescapable?
- Is the signal of coalescence from close pairs of neutron stars or/and black holes as predicted from Einstein's theory?

Relativistic Astrophysics and Galaxy Structure Formation

- What is the maximum mass of a neutron star and the minimum and maximum mass of a stellar origin black hole?
- What is the mass function and redshift distribution of stellar origin neutron stars and black holes?
- How do neutron star and black hole masses and spins evolve in relation to the environment and with cosmic epoch?
- What is the physical mechanism behind supernovae and how asymmetric is their collapse?
- How do stellar origin compact binaries form? Do they form in binary stars, or dynamically in dense star clusters or both?
- Do black hole coalescence events of any flavour have an associated electromagnetic counterpart?
- How can we identify the counterparts of neutron star binary mergers and of black hole-neutron star mergers? Are they related to known sources as short gamma-ray bursts (GRBs) and kilo-novae?
- How many compact binaries of all flavours exist in the Milky Way and what do they tell us about the star formation history of our own galaxy?

- Are ultra-compact white dwarf binaries the progenitors of Type Ia supernovae?
- How do massive black hole form? Via accretion or/and aggregation of stellar origin black holes, or via the direct collapse of supermassive stars?
- How do seed black holes grow to become giant through accretion and mergers, and how fast do they grow over cosmic time?
- How often compact object binaries of the different flavours coalesce in galaxies and how does their coalescence rate evolve with redshift?
- When did the first black holes form in pre-galactic halos, and what is their initial mass and spin distribution?
- How do massive black holes pair in galaxy mergers and how fast do they coalesce?
- What is the role of black hole mergers in galaxy formation?
- Are massive black holes as light as $10^{3-5} M_{\odot}$ inhabiting the cores of all dwarf galaxies?
- What is the mass distribution of stellar remnants at the galactic centres and what is the role of mass segregation and relaxation in determining the nature of the stellar populations around the nuclear black holes in galaxies?
- What is the merger rate of extreme mass ratio inspirals in galactic nuclei?

Cosmography-Cosmology

- What is the architecture of the universe?
- Using precise gravitationally calibrated distances and redshift measurements of coalescence events to what precision can we measure the Hubble flow?
- What is the equation of state of dark energy, and to what precision can it be inferred from gravitational wave sources?
- What can gravitational waves tell us about the physics beyond the Standard Model?
- Can we measure or set bounds on cosmological gravitational wave backgrounds from the very early universe?

2 Prologue: GW150914 - the first cosmic source of gravitational waves

In the last years the detection of gravitational waves was perceived as imminent, following the rebuild of the LIGO interferometers at Hanford and Livingston,¹ and of the interferometer Virgo in Pisa. Operating in the frequency interval between 10 Hz and 1000 Hz, Advanced LIGO and Virgo are designed to detect gravitational waves emitted by highly perturbed/deformed neutron stars, core collapsing massive stars and by the merger of pairs of neutron stars and stellar origin black holes. The rates of these events were so uncertain to prevent any definite prediction on the nature of the first signal, whether coming from neutron stars or black holes, or a combination of the two. But, on February 11th 2016, during the drafting of this chapter, from the LIGO Scientific Collaboration and The Virgo Collaboration came the announcement of²

- *the first direct detection of gravitational waves from a cosmic source;*
- *the discovery of the most powerful astronomical event ever observed since the Big Bang;*
- *the first detection of two stellar origin black holes coalescing in a single black hole, according to general relativity, and observed through the inspiral, merging and ringdown phases.*

The discovery of this event, named GW150914, confirms, within statistical uncertainties and current precision^a,

- *Einstein's theory of gravity in the dynamical strong field regime, never tested before;*
- *Einstein's theory on the generation of gravitational radiation;*
- *the unimpeded propagation of gravitational waves across the universe;*
- *the existence of highly dynamical space-times that can form in the cosmos;*
- *the existence and overall simplicity of black holes.*

From an astrophysical perspective, the discovery of GW150914 provides

- *the first measure of the mass and spin of stellar black holes through gravity's own messenger: the gravitational waves;*
- *the first identification of "heavy" stellar origin black holes with mass $\sim 30 M_\odot$;*

^aWe remark that the current signal from GW150914 is not sufficient to exclude more exotic configurations than black holes as described in general relativity. Only precision observations of the late-time ringdown signal, where the differences in the quasinormal-mode spectrum eventually emerge, can be used to rule out exotic alternatives to black holes and to test quantum effects at the horizon scale.^{3,4}

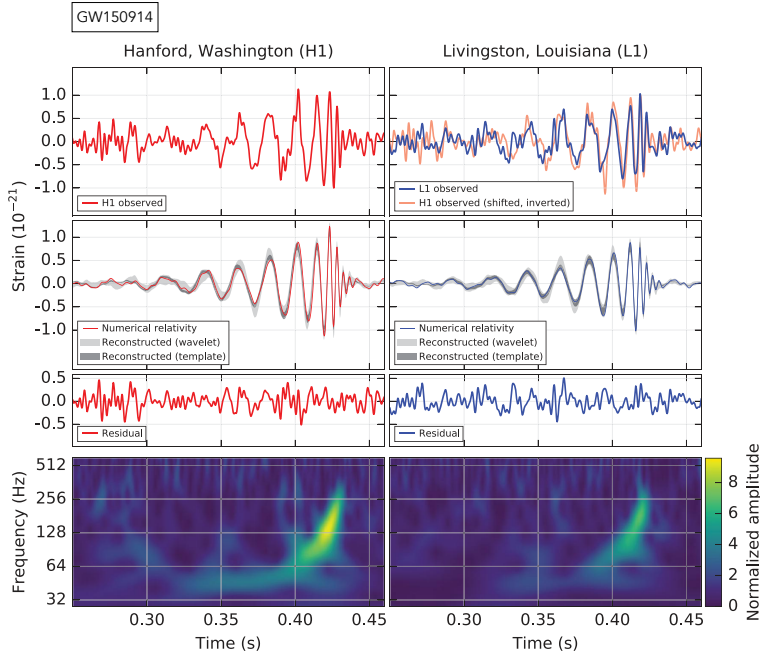


Figure 1: The gravitational wave signal from the first cosmic source detected in gravitational waves: GW150914 observed by the LIGO Hanford (H1, left panel) and Livingston (L1, right panel) interferometers.² The first row gives the strain with time in the two detectors. The second row gives the gravitational wave strain projected onto each detector in the 35–350 Hz band, and the solid lines show the numerical relativity waveform for a source with parameters consistent with the inspiral, merger and ringdown of two coalescing black holes of $36^{+5}_{-4} M_{\odot}$ and $29^{+4}_{-4} M_{\odot}$, forming a new black hole of $62^{+4}_{-4} M_{\odot}$. The bottom row gives a time-frequency representation of the strain data, showing the signal frequency increasing over time. Courtesy of the LIGO Scientific Collaboration and Virgo Collaboration.²

- the first definite proof of the existence of "binary black holes";
- the most massive stellar origin black hole known to date, resulting from a merger product: $62 M_{\odot}$.

The signal from GW150914, lasting less than 0.45 seconds, is extraordinary simple.² As shown in Figure 1, the signal sweeps upwards in amplitude and frequency of oscillation from 30 Hz to 250 Hz, with a peak gravitational wave strain h of 1.0×10^{-21} and significance of 5.1σ . The signal matches the waveform predicted by general relativity of the *inspiral*, *merger*, and *ringdown* of two black holes of $36^{+5}_{-4} M_{\odot}$ and $29^{+4}_{-4} M_{\odot}$ in the source-frame. The new black hole that

formed has rest-frame mass $62_{-4}^{+4} M_\odot$ and spin $s_{\text{spin}} = 0.67_{-0.07}^{+0.05}$. The energy radiated in gravitational waves corresponds to $3.0_{-0.5}^{+0.5} M_\odot c^2$, and to a peak luminosity of $3.6_{-0.4}^{+0.5} \times 10^{56} \text{ erg s}^{-1}$ equivalent to $200_{-20}^{+30} M_\odot c^2 \text{ s}^{-1}$. The source was observed with a matched filter signal-to-noise ratio of 23.7, and lies at a luminosity distance of $410_{-180}^{+160} \text{ Mpc}$, corresponding to a redshift $z = 0.09_{-0.04}^{+0.03}$ (assuming the current Λ -CDM cosmological model).

During the editing of this Chapter, the LIGO Scientific Collaboration and the Virgo Collaboration announced the discovery of a second signal: GW151226, detected at a significance greater than 5σ .⁵ Again a remarkable finding. The signal lasted in the LIGO frequency band for approximately 1 second, increasing in frequency and amplitude over about 55 cycles from 35 to 450 Hz (higher than that of the first event), and reached a peak gravitational strain of $3.4_{-0.9}^{+0.7} \times 10^{-22}$. The event detected with a signal-to-noise ratio of 13 is consistent again with the coalescence of two stellar origin black holes of $14.2_{-2.3}^{+8.3} M_\odot$ and $7.5_{-2.3}^{+2.3} M_\odot$ and a final mass of $20.8_{-1.7}^{+6.2} M_\odot$, in the rest frame of the source. The long lasting signal allowed the measure of the spin of one of the component black holes, which has spin parameter greater than 0.2. GW151226 is located at a distance of $440_{-190}^{+180} \text{ Mpc}$, corresponding to a redshift $z = 0.09_{-0.04}^{+0.03}$, similar to that of GW150914. While the high black hole masses in GW150914 lie in an almost unexplored interval, the masses in GW151226 are in line with those inferred in X-ray binaries.⁶ In §4.1 we will discuss the repercussions of these findings on the origin and nature of stellar mass black holes.

In general, the signal expected from *coalescing binaries* of all flavours carries exquisite, and unique information on the *masses* and *spins* of the sources and of their *internal* structure: in the case of GW150914 and GW151226 the simplicity of two colliding black holes. Masses and spins will be the leitmotif of this Chapter on gravitational wave sources, as they are key parameters with which we will be describing the gravitational wave universe in a way complementary to that offered by electromagnetic observations, and often unaccessible otherwise. Key sources of the gravitational wave universe have been already presented in^{7–10} and will be described ahead in this Chapter. ^b

3 A new cosmic landscape

The theory of general relativity by Einstein makes five key predictions: the existence of

- black holes;
- an upper limit on the compactness of any self-gravitating object endowed of a surface (neutron stars being a chief example);

^bRegretfully, the references have been limited to a minimum, due to the vastness of the topic. We will be mentioning main key and recent papers supplemented by specific reviews, which do include more extensive references.

- a maximum mass for stable, degenerate matter at nuclear densities, known as Oppenheimer Volkoff limit;
- a maximum mass for (idealised) supermassive stars dominated by radiation pressure;
- gravitational waves emitted by accelerated masses in non spherical motion.

The electromagnetic observations of the universe reveal the existence of

- neutron stars, endowed by strong gravity, rapid rotation, intense magnetic fields, and high temperatures. Powered either by rotation or accretion or magnetic field dissipation, neutron stars are living in isolation or in binaries with stars or neutron stars as companions. They are ubiquitous and widespread in all the galaxies;
- stellar origin black holes, powered by accretion and observed in a variety of X-ray binary systems with stars as companions. They are ubiquitous and widespread in all the galaxies;
- active and quiescent supermassive black holes at the centres of galaxies;
- galaxies with central supermassive black holes on their way to collide and merge;
- an expanding universe changing and evolving on all scales, with gas fragmenting into stars inside dark matter halos (on the smallest scales), and galaxies embedded in dark matter halos assembling in galaxy's clusters (on the largest scales);
- an expanding universe at large, dominated by a dark energy component of unknown origin.

The *combination* of these two items set the frame for constructing a new cosmic landscape, that of the *gravitational wave universe*. By observing the universe with gravitational waves as messengers we will be able to answer to the deep questions outlined in §1. We now explore the content of each item, establishing connections among the different voices.

3.1 Black holes, neutron stars and supermassive stars as basic equilibrium objects

• Black Holes

The simplest object to describe in nature is a *black hole*, representing the exact solution for the metric tensor of a *point mass* M , in otherwise empty space.¹¹ The black hole solution found by Schwarzschild in 1916 describes the static, isotropic gravitational field generated by an uncharged point mass M . The mass M confined into a null volume, at $r = 0$, is surrounded by an *event horizon*, i.e.

a boundary in spacetime defined with respect to the external universe inside of which events cannot affect any external observer. M is not the baryonic mass only, but it includes the gravitational energy. Within the event horizon of a black hole all paths that electromagnetic waves could take are warped so as to fall farther into the black hole. In Schwarzschild coordinates, the event horizon, i.e. the surface of no return, appears as a critical spherical surface of radius $R_S = 2GM/c^2$, the Schwarzschild's radius of the point mass M . For the Sun the Schwarzschild radius of 2.95 km is deep in the solar interior, where Einstein's equations in matter space exhibit no singularity. A key property of the Schwarzschild metric, which has no Newtonian analogue, is that below a radius, $R_{\text{isco}} = 3R_S$, all circular orbits of massive particles are unstable ("isco" is acronym of innermost stable circular orbit). Massive particles moving on these geodesics are fated to cross the horizon, if subjected to an infinitesimal perturbation.

The Schwarzschild solution is a limiting case of a more general solution of the Einstein's field equations found by Roy Kerr,¹² which describes the spacetime metric of an *axially-symmetric* point mass M surrounded by an event horizon, and describes an uncharged, *rotating black hole* with mass M : here M includes the negative contribution from the gravitational energy and the positive contribution by rotation, besides the matter load. The finding by Kerr is remarkable as it shows, contrary to Newtonian gravitation, that a mass endowed with rotation warps spacetime as the energy content from rotation becomes source of gravity itself, due to the non linearity of Einstein's equation. Rotation is described by the spin vector $\mathbf{S} = \mathbf{s}_{\text{spin}} GM^2/c$, where the norm of the vector \mathbf{s}_{spin} is the spin parameter taking values between 0 and 1. Counterintuitively, the horizon of a Kerr black hole is smaller than R_S and takes a simple expression: $R_{\text{horizon}} = (G/c^2)[M + (M^2 - s_{\text{spin}}^2 M^2)^{1/2}]$. Also R_{isco} depends on s_{spin} , and for $s_{\text{spin}} = 1$, a test particle in co-rotation (counter-rotation) has R_{isco} placed at GM/c^2 ($9GM/c^2$).

Kerr black holes have become central for understanding the nature of singularities in general relativity, and a conjecture has been posed, known as *cosmic censorship conjecture* which asserts that no *naked* singularities form in Nature. In other words, it asserts that singularities (present in the classical description of gravity) are enclosed by a horizon so that information does not propagate into the rest of the universe, hidden from any observer at infinity by the event horizon of a black hole. For this reason the spin of a Kerr black hole is limited to values $s_{\text{spin}} \leq 1$, with $s_{\text{spin}} = 1$ corresponding to a maximally rotating Kerr black hole (for $s_{\text{spin}} > 1$ a naked singularity would appear).

Black holes are fundamentally geometrical objects and a theorem, known as *uniqueness* theorem, states that Kerr black holes are the unique end-state of gravitational collapse.^{13–15} This created the belief that all "astrophysical" black holes (that form in Nature) are Kerr black holes, being the Kerr solution the only stationary solution of Einstein's equation. The uniqueness theorem paved the way to a further conjecture, known as *no-hair theorem*. The no-hair theorem postulates that all black hole solutions of the Einstein-Maxwell equations of gravitation and electromagnetism in general relativity can be completely char-

acterised by only three externally observable parameters: the mass M , angular momentum \mathbf{S} , and electric charge. All other information (for which "hair" is a metaphor) about the matter which formed a black hole or fall into it, disappears behind the black hole event horizon and is therefore permanently not accessible to external observers. A corollary of the no-hair conjecture asserts that the only deformations that black holes admit are those obtained by a change of mass and angular momentum as it occurs during the merger of two black holes, or during their substantial growth by accretion of in-falling matter. Any residual deformation is then radiated away by gravitational waves.^c

While the theory of general relativity poses a limit on the angular momentum, *no upper limit* exists on the *mass* of a classical Kerr black hole. Only a lower bound exists, imposed by quantum mechanics natural units: the Planck mass $M_{\text{Pl}} = (\hbar c / 8\pi G)^{1/2} = 4.34 \mu\text{g}$ below which a quantum description of gravity is desired.¹⁶ Astrophysical black holes are grouped in three classes or flavours possibly because of their different origin: the stellar black holes with masses in the interval $[3 M_{\odot}, 100 M_{\odot}]$, the (super-)massive black holes of $[10^5 M_{\odot}, 10^{10} M_{\odot}]$, and the middleweight or intermediate mass black holes of $[100 M_{\odot}, 10^5 M_{\odot}]$. The boundaries of each interval are loosely defined and still arbitrary, as the physical mechanisms leading to the formation of massive black holes are uncertain. Detecting black holes of all flavours as gravitational wave sources will shed light into these mechanisms, and their potential connections.

• Compactness

Let us now proceed on considering the limit on the compactness of any astrophysical object endowed by a *surface*. A consequence of the Oppenheimer-Volkoff equation for the equilibrium of a self-gravitating spherical body, of mass M and radius R , is that its *compactness* defined as $\mathcal{C} \equiv GM/Rc^2$ can not exceed a limiting value $\mathcal{C} < \mathcal{C}_{\max} = 4/9$, which holds for all stars, incompressible or not. *An equilibrium object with $\mathcal{C} > \mathcal{C}_{\max}$ can not exist with a finite surface.* Note that the Schwarzschild radius R_S (and in general R_{horizon}) violates this condition, implying the presence of a singularity in the interior solution of the Einstein's equations.

Not only this condition poses a *lower limit* on the radius R of any star, but paves the way to the idea that Kerr black holes inevitably form in nature, as soon as the condition $\mathcal{C} < \mathcal{C}_{\max}$ is violated. Instability to collapse occurs when the pressure support against gravity, determined by the *microphysical* properties of matter, drops to the point that the total energy E of the configuration is no longer a minimum.¹⁷^d The consequent loss of stability and evolution toward gravitational collapse occurs for a variety of reasons and here we highlight the most important.

^cWe do not consider here charged black holes and they are of no interest in astrophysics. Astrophysical black holes do not live in isolation and thus do not carry a charge. If charged, matter of opposite charge would fall in to obliterate any charge excess, making the black hole neutral.

^dThe minimum here is computed with respect to all variations in the density profile $\rho(r)$ that leave the number of particles N unchanged, and unchanged and uniform the entropy per nucleon and chemical composition.

- Neutron stars

In Newtonian gravity, gravitational collapse occurs when a stellar core supported by the degeneracy pressure of cold electrons becomes massive enough that electrons in their quantum states become ultra-relativistic, i.e. when their Fermi energy exceeds the electron rest mass energy $m_e c^2$. The reduced pressure support implied by this microphysical state transition occurs at the *Chandrasekhar mass limit* of $M_{\text{Ch}} \sim 1.4 M_\odot$ (whose exact value depends on the chemical composition of the stellar core). Stellar evolution models show that when the iron core of a massive evolving star increases above M_{Ch} , core collapse ensues promptly. The dynamical contraction comes to a halt when the entire iron core at the Chandrasekhar mass limit has been transformed in a core of neutrons plus few exotic nuclei, at around or even above nuclear density $\rho_{\text{nuc}} \equiv 1.4 \times 10^{14} \text{ g cm}^{-3}$. A new equilibrium, i.e. a *neutron star* endowed with a surface (of radius $R \sim 10 \text{ km}$) forms, supported by neutron degeneracy. The transformation of nuclear matter occurs following photodissociation of iron group nuclei and helium present in the core, and deleptonization of matter via weak interactions (mostly electron captures by protons) with the concomitant emission of neutrinos of all flavours. The universality of the process leads to the prediction that neutron stars at birth carry a mass M_{NS} close to the Chandrasekhar mass limit M_{Ch} .

The Oppenheimer-Volkoff equation, which describes non-rotating neutron stars, does not admit stable equilibria above a *maximum mass*, $M_{\text{max}}^{\text{NS}}$, whose exact value depends on the details of the equation of state (EoS) of matter above nuclear density.¹⁸ If the Chandrasekhar mass limit refers to a Newtonian instability driven by microphysical processes (change in the degree of degeneracy) inside the star, the instability of neutron stars above the maximum mass limit is induced by general relativity only.¹⁷ What triggers the instability in a neutron star above the maximum mass is the pressure source term in the right hand side of the Oppenheimer-Volkoff equation. The huge pressure (from microphysical processes) requested to counteract relativistic gravity acts as gravity source (before the degenerate neutrons become ultra-relativistic).

Rotation can contrast gravity, and uniformly rotating neutron stars can carry a mass higher than the corresponding static limit. The maximum mass of a uniformly rotating star is determined by the spin rate at which a fluid element at the equator moves on a geodesic so that any further speed-up would lead to mass shedding. This maximum mass can be determined numerically and is found to be at most $\sim 20\%$ larger than the non-rotating value.¹⁹ Only differentially rotating neutron stars can support significantly more mass than their non-rotating or uniformly rotating counterparts.²⁰ *Hyper-massive neutron stars* are differentially rotating neutron stars with masses exceeding the maximum mass of a uniformly rotating neutron star. Because of the large angular momentum and shear, the hyper-massive neutron star is dynamically unstable to nonlinear instabilities leading to a bar mode deformation.²¹ In general, the collapse of the hyper-massive neutron star to a rotating black hole is temporarily prevented by its differential rotation, but a number of dissipative processes, such as magnetic fields, viscosity, or gravitational wave emission, will act so as to remove differential rotation. The hyper-massive neutron star can collapse directly to a black

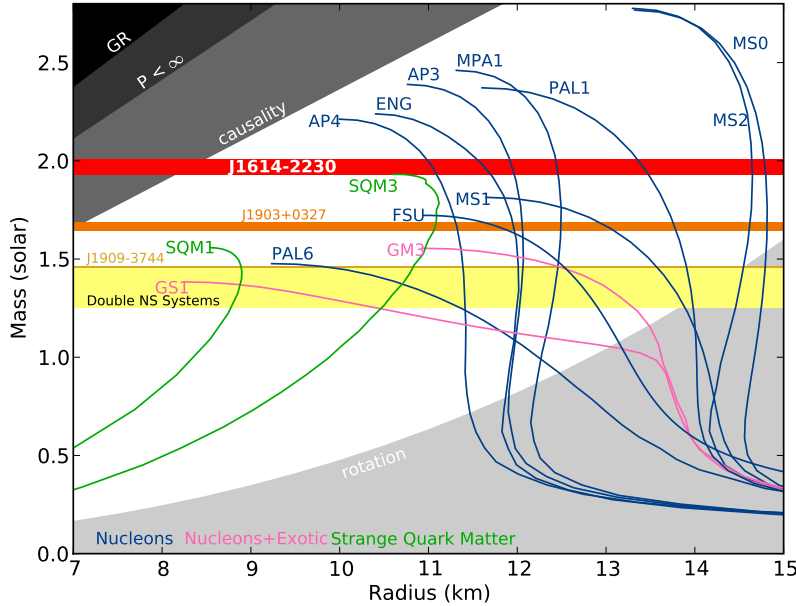


Figure 2: Sequences of neutron star equilibria for selected Equations of State (EoS).¹⁸ The figure shows the mass M versus radius R relation, for non-spinning neutron star models. The yellow band shows the interval of masses inferred from the sample of double neutron star binaries. The orange (red) band indicates the mass of the neutron star in J1903+0327 (J1614-2230). The largest mass currently measured is that in J1614-2230, of $1.97 \pm 0.04 M_{\odot}$. Thus, any EoS line that does not intersect the J1614-2230 band is ruled out by this measurement.²² In particular, most EoS involving exotic matter, such as kaon condensates or hyperons, tend to predict maximum neutron star masses below $2.0 M_{\odot}$, and are therefore ruled out. Green lines refer to strange star models. The upper left grey areas of different intensity refer to regions excluded by general relativity and causality, and the lower grey area is excluded by observations of the fastest pulsars. Courtesy of P. Demorest.

hole on the dynamical timescale. Alternatively, the star by loosing its differential rotation may evolve into a so-called *supra-massive* neutron star, i.e., an axisymmetric and uniformly rotating neutron star with mass exceeding the limit for non-rotating neutron stars (defined in the static limit). Magneto-rotational energy losses ultimately drive the star to collapse secularly to a black hole. In Nature, hyper-massive neutron stars likely form in the aftermath of a neutron star-neutron star merger that we will describe in §7.3.

According to many theoretical studies, there exists a range of values for the mass M_{\max}^{NS} in the static limit, between $1.5 M_{\odot}$ and $2.7 M_{\odot}$, due to current uncertainties in the behaviour of matter at supra-nuclear densities as shown in Figure 2. Quantum chromodynamics is expected to give a complete description of matter at the energy-densities of neutron stars. At present no unique model exists for describing the many-body (10^{57} baryons) nuclear interaction, understood as a residual coupling of the more fundamental interactions among quarks, and a phase transition to a free quark state may occur inside the star. A strange star made of strange quarks, representing the lowest energy state of matter at zero temperature, may also form in Nature.¹⁸

- Supermassive stars

A second example of a relativistic instability which conducts to the black hole concept is that of an equilibrium configuration dominated by *radiation*.¹⁷ This is called *supermassive star*, with hypothetical masses clustering around $10^5 M_{\odot}$, but unknown dispersion.

Consider a supermassive star dominated by radiation, in convective equilibrium and with uniform chemical composition. Its mass M_{sms} is determined uniquely by the value of the photon entropy per baryon $s_{\text{rad}} = (4/3)aT^3/n$, where T is the temperature of radiation and matter, n the baryon number density and $a = \pi^2 k_B/(15c^3 \hbar^3)$ the radiation constant (with k_B and \hbar the Boltzmann and Planck constants). Since a supermassive star has the structure of a Newtonian polytrope of index $\gamma = 4/3$, supermassive stars can cover a wide mass spectrum, depending only on s_{rad} , and their mass is

$$M_{\text{sms}} = 1.127 \left(\frac{s_{\text{rad}}}{k_B} \right)^2 M_{\odot}, \quad (1)$$

independent on the central density.¹⁷ The interesting fact is that one can relate s_{rad} to the baryon load of the star. A simple calculation shows that $s_{\text{rad}}/k_B = 8\beta^{-1}$, where β is the matter to radiation pressure ratio. Arbitrarily large masses can be assembled for arbitrarily small values of β , since $M_{\text{sms}} \propto \beta^{-2}$. Since a polytropic relation connects the mass, radius and central density, one can compute the compactness parameter C which turns out to be very small $\ll 0.39$ since supermassive stars are rarefied, loosely bound objects (for $M_{\text{sms}} = 10^4 M_{\odot}$ the radius is $R \gg 10^4$ km) with low surface gravity owing to radiation pressure.

Although general relativity does not intervene in determining the overall structure of the star, it affects instead its stability, as a polytrope of $\gamma = 4/3$ is, in stellar structure, the trembling limit between stability and instability of the star, so it is necessary to take into account the small effect of matter pressure and general relativity which play little or no role in their structure calculation. A further important fact is that a supermassive star radiates energy at a rate very close to the Eddington limit $L_{\text{Edd}} = 4\pi GM_{\text{sms}}mc/\sigma_T = 1.3 \times 10^{42}(M_{\text{sms}}/10^4 M_{\odot}) \text{ erg s}^{-1}$ (where m is the mean baryon mass and σ_T the Thomson cross section), and therefore its total energy E continues to decrease. Thus, the star evolves over time toward states of lower energy (more bound) and higher compaction. When plasma and general relativity effects

are included in the stability analysis, one can show that the supermassive star loses its stability when its central density has reached a limiting value $\rho_{\text{crit}} = 1.996 \times 10^4 (10^4 M_{\odot}/M_{\text{sms}})^{7/2} \text{ gr cm}^{-3}$ after having radiated away an energy $E_{\text{rad}} = 3.583 \times 10^{54} \text{ erg}$, over its lifetime, a quite large value which is independent on the mass of the supermassive star. At the critical point of instability, the core temperature $T_{\text{crit}} = 4 \times 10^9 (10^4 M_{\odot}/M_{\text{sms}}) \text{ K}$ is large enough to ignite nuclear reactions which can affect the final fate. Once the supermassive star has reached the instability line through a progression of quasi-static equilibrium states, it can either explode or collapse to a black hole.

General relativity calculations¹⁷ have shown that the nominal range of supermassive stars collapsing into a black hole lies between $\sim 5 \times 10^5 M_{\odot}$ and $\sim 10^8 M_{\odot}$.^e The collapse is homologous, with a velocity essentially linear with radius, and density profiles self-similar, although increasing in magnitude. Due to the homologous nature of the collapse, the entire mass moves inward coherently, crossing the event horizon in only a few light travel times GM_{sms}/c^3 .¹⁷ The concept of supermassive star has now evolved into the modern one of DCBH, acronym of a process which call for the Direct Collapse of a equilibrium structure as a supermassive star into a massive Black Hole.^{23,24} Supermassive stars, should they exist, are believed to grow via accretion onto an embryo of solar mass, in pristine, non-fragmenting gas clouds. In the context of structure formation models, they are viewed as equilibrium structures transiting through progressively more massive states (typically of $10^5 M_{\odot}$) that are conducive to stable episodes of hydrogen and helium burning. Later, they collapse into a black hole when crossing the general relativity instability limit either after exhaustion of the fuel or during the nuclear-burning phase.²⁵ Ahead in this chapter we will return on this issue.

3.2 Gravitational wave sources: a first glimpse

Neutron stars and black holes are the most bound, lowest-energy states of self-gravitating matter known in the universe where gravity is in the *strong field regime* and the field is *stationary*. No processes can lower their energy state. When do neutron stars and black holes become sources of gravitational waves?

Gravity is the weakest interaction in nature but when high compactness combines with large scale, non-spherical coherent mass motions with velocity v near the speed of light (as in a merger of two compact objects), then an immense luminosity can be emitted in gravitational waves, the luminosity scaling as $L \sim (c^5/G)(R_S/R)(v/c)^6$. GW150914 is the first extraordinary example of a merger of two black holes moving at near 1/2 of the speed of light releasing a luminosity in excess of $10^{56} \text{ erg s}^{-1}$.

^eThe maximum mass of a supermassive star is set by the comparison of two timescales: the thermal timescale τ_{thermal} and the timescale for the star to adjust to a new hydrostatic equilibrium, i.e. the dynamical timescale τ_{dyn} . If τ_{thermal} is shorter than τ_{dyn} the star can not any longer recover equilibrium, and rapid cooling leads the whole star to collapse. The thermal timescale at the boundary of stability $\tau_{\text{thermal}} \sim E_{\text{crit}}/L_E$ equals $\tau_{\text{dyn}} \sim (G\rho_{\text{crit}})^{-1/2}$ at a mass $M_{\text{max}}^{\text{sms}} \sim 10^8 M_{\odot}$.¹⁷

When perturbed out of equilibrium, during their formation or when colliding, neutron stars and black holes become often, and for a short time lapse, among the loudest sources of gravitational radiation in the universe. In particular, binary coalescences of compact objects are among the most powerful emitters that theory predicts. For binary coalescence we refer to the process of inspiral of two compact objects in a binary terminating with their merger into a new single unit, as is the case of GW150914 and GW151226.

In essence, the trait of a powerful gravitational wave source stems in its exquisite high degree of disequilibrium, leading to non-spherical dynamics under extreme conditions of compactness. Neutron stars, and black holes over a wide spectrum of masses are the protagonists of most of the violent events detectable by both current and next generations of interferometers, on Earth and in space.

- The frequency of gravitational waves

Gravitational wave sources emit over a broad frequency range, and there is a close link between the frequency of the gravitational wave f and mass M and compactness \mathcal{C} of the source. The natural unit for f is

$$f_o \equiv \frac{c^3}{GM} = \frac{c}{R_G} = 2 \times 10^5 \frac{M_\odot}{M} \text{ Hz}, \quad (2)$$

where $R_G \equiv GM/c^2$. In any self-bound system of mass M and size R , the natural frequency of oscillation, rotation, orbital revolution and dynamical collapse is of the order of

$$f_{\text{source}} \sim \left(\frac{GM}{R^3} \right)^{1/2} = f_o \left(\frac{R_G}{R} \right)^{3/2} = f_o \mathcal{C}^{3/2} \quad (3)$$

Since gravitational waves are emitted by accelerated, asymmetric mass motions, the frequency f of the gravitational wave is expected to be close to the frequency f_{source} of the source's mass motions; $f \simeq f_{\text{source}}$, and in general $f < f_o$, as $\mathcal{C} < 1$.

We focus now on the case of compact binary *coalescences* (CBCs). For *black holes*, whose horizon R_{horizon} is between 2 and 1 R_G (depending on the spin parameter s_{spin}), the characteristic frequency of the wave near coalescence is $\sim f_o$, so that the total mass M of the binary system determines the highest frequency of a coalescence signal. It is customary to introduce the frequency $f_{\text{isco}} \equiv f_o/(\pi 6^{3/2})$, equal to twice the Keplerian frequency of a test mass at the innermost stable circular orbit R_{isco} , as the characteristic frequency of a binary near coalescence. For stellar black holes with typical mass of $\sim 10 M_\odot$

$$f_{\text{isco}}^{\text{BH}*} \approx 0.44 \times 10^3 \left(\frac{10 M_\odot}{M} \right) \text{ Hz}, \quad (4)$$

whereas for massive black holes

$$f_{\text{isco}}^{\text{BH,massive}} \approx 4.4 \times 10^{-3} \left(\frac{10^6 M_\odot}{M} \right) \text{ Hz}. \quad (5)$$

During the inspiral and merger f sweeps upwards for $f \ll f_{\text{isco}}$, up to f_{isco} . As neutron stars carry masses $\sim 1.35 M_{\odot}$ they can extend their gravitational wave emission at slightly higher frequencies $f_{\text{isco}}^{\text{NS}} \simeq 1.6$ kHz than stellar black holes.

According to the above relations, coalescing *massive black holes* are intrinsically *low frequency* sources, whereas coalescing *stellar origin black holes* and *neutron stars* combined in different arrangements are *high frequency* sources. In the case of a binary composed by a massive and a stellar black hole (denoted as extreme mass ratio inspiral, EMRI) the reference mass is that of the largest hole. Thus, *EMRIs* belong to the *low frequency* universe as the mass of the big black hole sets the frequency of emission.

In more detail, if f_{\min} is the minimum (f_{\max} is the maximum) frequency of operation of an interferometer, equation (4) sets an upper (lower) limit on the mass of a binary that can be detected when nearing the final phase of plunge and coalescence. In the case of high frequency sources, this leads to

$$2.20 \left(\frac{2000 \text{ Hz}}{f_{\max}} \right) M_{\odot} < M < 440 \left(\frac{10 \text{ Hz}}{f_{\min}} \right) M_{\odot}. \quad (6)$$

In the case of low-frequency sources

$$4.4 \times 10^4 \left(\frac{0.1 \text{ Hz}}{f_{\max}} \right) M_{\odot} < M < 4.4 \times 10^7 \left(\frac{10^{-4} \text{ Hz}}{f_{\min}} \right) M_{\odot}. \quad (7)$$

At nanoHz frequencies, the typical mass of a black hole binary near coalescence would be far in excess of $10^{10} M_{\odot}$. At these very low frequencies, it is possible to detect the signal from supermassive black holes of $10^{8-9.5} M_{\odot}$ far from coalescence, i.e. at $f \ll f_{\circ}$. The signal in this case is continuous and nearly monochromatic. By contrast, the signal from coalescing binaries is transient in nature and peaks during the latest phases of inspiral and plunge when the two objects reach separations comparable to their sizes: ~ 60 km for neutron stars, ~ 200 km for stellar origin black holes, and a few AU up to $\lesssim 10 - 100$ AU for massive black holes, depending in their mass. How this variety of coalescing binaries form in Nature is the subject of the following section. To this purpose we here overview key observational properties and key notions in the realm of current astronomical observations.

4 The electromagnetic universe

4.1 Neutron stars and stellar origin black holes in the realm of observations

Neutron stars are known to form in the aftermath of the gravitational collapse of massive stars ($\gtrsim 10 M_{\odot}$) whose degenerate iron core is driven above the Chandrasekhar mass limit. The collapse releases $\sim 10^{53}$ erg. Most of the energy (99%) is emitted in neutrinos and only about 10^{51} erg into kinetic energy of the supernova explosion which is associated to the propagation of a shock wave,

emerging when the infalling star's envelope impacts on the dense neutronized core that settles into equilibrium: that of a young, hot neutron star. During shock break-out, the stellar envelope unbinds producing a luminous supernova.²⁶ Crab with its remnants is a magnificent example of a successful supernova explosion. However, if the shock break-out is weaker, as for the case of heavier stars, a stellar black hole forms by *fall back* of part of the envelope onto the proto-neutron star driven above its maximum mass. At the extremes, *direct collapse* to a black hole can occur.

The mass of a compact object can be measured when it is a member of a binary system. At present, data from a variety of observations indicate that *neutron stars* likely show a bimodal, asymmetric distribution in their masses, with a low mass component centred around $1.393 M_{\odot}$ and dispersion $0.064 M_{\odot}$, and a heavier component with a mass mean of $1.807 M_{\odot}$ and dispersion $0.177 M_{\odot}$.²⁷ The yellow strip in Figure 2 shows the range of neutron star masses observed in double neutron star binaries, and the red line shows the heaviest neutron star ever detected of $1.97 \pm 0.04 M_{\odot}$ ²² consistent with the expectation that neutron stars in "binaries" experience *re-cycling*, i.e. a long-lived phase during which they accrete matter from the companion star. In this case, the mass of the compact object may not represent the mass at birth and gives information on the interaction of the neutron star with its companion. As shown in Figure 2, this finding already rules out the softest EoS for nuclear matter.

For *stellar origin black holes*, reliable dynamical mass measurements in low mass X-ray binaries are best described by a narrow mass distribution peaked around $7.8 \pm 1.2 M_{\odot}$ ⁶ with a clear divide between neutron stars and black holes, i.e. no remnants between ~ 3 and $5 M_{\odot}$,²⁸ often referred to as *gap*. Higher mass values are inferred in high mass X-ray binaries, and the mass of Cyg X-1, the first black hole discovered in X-rays is bound to values $\sim 14 - 16 M_{\odot}$. The currently observed range of black hole masses is indicated in Figure 3 as lower grey strip, and the two black holes in GW151226 fall in the same range. But, the discovery of the two "heavy" stellar black holes of 29 and $36 M_{\odot}$ in GW150914 came as a surprise,²⁹ though hypothesised by^{30,31} in their studies on binaries. Heavy stellar black holes, resulting from low metallicity progenitor stars, were considered earlier by³² in the context of a class of sources known as Ultra Luminous X-ray sources, which often inhabit low metallicity galaxies.

The fate of massive stars and nature of the relic is a complex process to model. Studies by³⁴⁻³⁶ show that the nature of the remnant depends to a large extent: (i) on the mass loss by stellar winds during the different evolutionary stages, driven by the opacity of the metals present in the star's envelope and measured by the metallicity Z (defined as the logarithm in power of ten of the iron to hydrogen abundance ratio, and often expressed in units of the solar metallicity $Z_{\odot} = 0.02$); (ii) on rotation; (iii) on the strength of the shock break-out through the stellar envelope after core collapse and bounce; (iv) on the interplay between neutrino cooling and heating at the interface between the neutrino-sphere and the (stalled) shock; and (v) on the amount of fall-back material accreted onto the newly born hot neutron star, after formation of a reverse shock. These processes establish whether the collapse is delayed (lasting

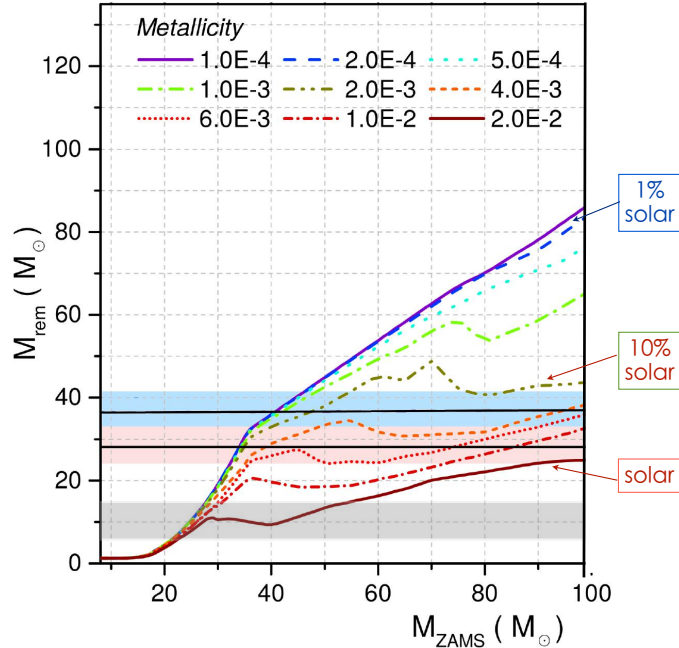


Figure 3: The figure shows the mass of the remnant as a function of the mass of the progenitor star in the interval between $[10 M_{\odot}, 100 M_{\odot}]$ for different values of the stellar metallicity, from³³. The lower (solid red) line refers to $Z = 0.02$ (Sun's metallicity). The upper line refers to $Z = 10^{-4}$. In between the metallicities (from bottom to top) are $0.01, 0.006, 0.004, 0.002, 0.0001, 5 \times 10^{-4}, 2 \times 10^{-4}$. (A black hole is assumed to form above $M_{\text{max}}^{\text{NS}} = 3 M_{\odot}$.) The upper horizontal bands indicate the two values of the black hole masses of GW150914 (and uncertainty interval), prior to merger, and the lower pink strip indicates the interval of black hole masses measured electromagnetically in galactic X-ray binaries.⁶ The black holes in GW151226 fall in this lower strip. Courtesy of M. Mapelli.

longer than 0.5 sec) or prompt (lasting less than 250 msec) and determine the value of the mass of the relic star.

Figure 3 shows the mass of the compact remnants as a function of the star's initial mass, in the interval between $[10 M_{\odot}, 100 M_{\odot}]$ for different values of the absolute metallicity Z , predicted by the models of³³. The figure indicates that lower metallicity progenitor stars leave heavier relic black holes. The upper

horizontal bands in the figure indicate the masses of the two black holes in GW150914 (with their uncertainties). Metallicities of the order of $0.1 - 0.2 Z_{\odot}$ are necessary to form stellar origin black holes as heavy as those in GW150914, from stellar evolution models.^{30,33,37} We further note that black holes with masses $\lesssim 15 M_{\odot}$ form in any metallicity environment. Thus the black holes in GW151226 do not pose constraints on the metallicity of the host galaxy.^{5,38}

Following the discovery of GW150914^{2,29} and of GW151226⁵ new questions arise:

- What is the shape and normalisation of the mass function of relic stars?
- How far does the black hole mass function extend at high masses?
- How can pairs of relativistic objects as those in GW150914 and GW151226 form in binaries and coalesce within the age of the universe?
- Which are the astrophysical conditions for the rise of a substantial population of gravitational wave sources as GW150914?

4.2 Forming stellar origin compact binaries

Tutukov and Yungelson were the first to study the evolution of isolated massive binaries, and predicted the formation of merging binary compact objects of the different flavours.^{39,40} The formation of neutron star binaries (NS,NS) became the subject of intense studies soon after the discovery of PSR1913+16, the first binary pulsar for which we had evidence, albeit indirect, of the existence of gravitational waves.^{41,42} Formation models of neutron star-black hole (NS,BH*) and black hole-black hole (BH*,BH*) binaries have been developed in parallel despite lacking of any observational evidence. Compact binaries can form in the galactic field as outcome of stellar evolution in primordial binaries;^{30,31,43,44} in dense star clusters via stellar dynamical exchanges involving stars and black holes;⁴⁵⁻⁴⁸ or in more exotic environments as in the discs of active galactic nuclei.⁴⁹

Stellar population synthesis models are a powerful tool to establish how and in which fraction close pairs of compact objects can form in primordial binaries and coalesce within a Hubble time. The input parameters for starting a simulation are: (i) the shape of the underlying gravitational potential, (ii) the initial mass function (IMF) of massive stars on the zero-age main sequence, (iii) the metallicity of the parent gas cloud, (iv) the fraction of primordial binaries (and triplets), and (v) the distribution of the initial binary separation and eccentricity, which affect the degree of interaction of the two stars over their lifetime.

Stars lose mass via winds, but in binaries they can also donate their mass to the companion via mass exchange, as illustrated in Figure 4, which depicts the evolution of a binary system in a simplified way. Mass transfer occurs when the most massive star, which evolves first away from the main sequence,

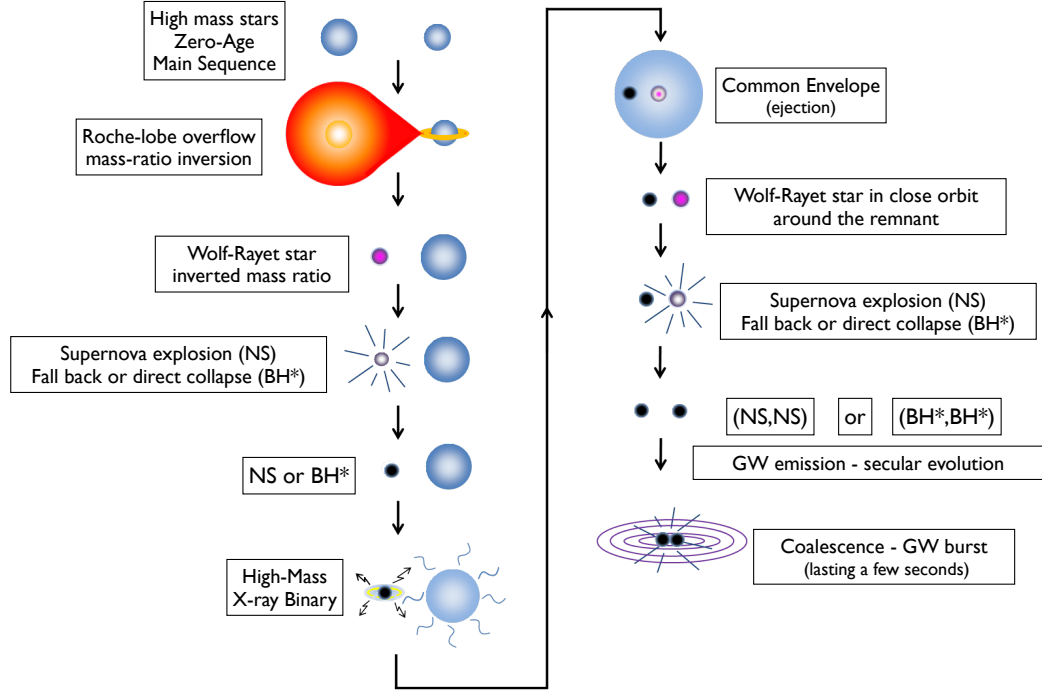


Figure 4: The path of formation of compact binaries in the primordial binary scenario. The initial mass of the stars determine the nature of the compact binary. To reproduce the data of GW150914, Belczynski et al.³⁷ start with two stars of $96 M_{\odot}$ and $60 M_{\odot}$, at a separation of $2463 R_{\odot}$ in a low metallicity environment, with $Z = 0.03 Z_{\odot}$ (we defer to Figure 1 of³⁷). The figure is rearranged from.⁵⁰ Courtesy of T. Tauris.

fills its Roche lobe. The pouring of mass on the companion star leads to a re-equilibration of the mass ratio and in general makes the less massive star the heaviest in the system as time evolves. After mass exchange, the star that evolves first becomes a Wolf-Rayet or a helium star (depending on the initial mass) that can go supernova. The supernova explosion can unbind the binary due to mass loss and recoil that accompany anisotropic core-collapse. Neutron stars are known to receive natal kicks at the time of their formation, with mean velocities of $\sim 400 \text{ km s}^{-1}$,⁵¹ so that the binary can break up. In fact, as many as $\sim 90\%$ of potential binaries may end up being disrupted after the first supernova explosion. This makes (NS,star) binaries very rare objects. Black holes which

form either through fall back (with supernova display) or direct collapse, likely receive lower kicks but the three-dimensional distribution of their natal velocities is unknown.⁵² Thus, the weaker mass loss that may accompany their formation, and lower natal kicks may help a heavy binary to survive almost intact after the formation of the first compact object. Thus the rate of formation of (NS,star), (BH*,star) systems is not directly set by the shape of the IMF, as disruption mechanisms that break lighter binaries can limit the number of double neutron star systems that may form.

After birth of the first remnant, evolution continues, through a phase of Common Envelope evolution (depicted in Figure 4) when the second star becomes a giant and starts engulfing the companion remnant which spirals inwards via gas dynamical friction losing orbital angular momentum and energy, which is deposited as heat in the largely convective envelope. Then, the remnant star either merges plunging inside the dense core of the companion star, or lands on a close, very tight orbit after having ejected the entire envelope. In this last case, the core of the star evolves into a relic object and may go supernova, fall-back or direct collapse depending on its mass, so that binaries of all the three flavours can form. After common envelope and mass ejection, the tight binary that forms is less fragile against break up and can survive. If the two relic stars that managed to remain bound are sufficiently close (a few solar radii in separation), gravitational waves will drive the binary toward coalescence (as described in §6), on timescales that may vary between a few Myr to Gyr or more. This avenue is affected by uncertainties on the common envelope evolution process, the kick distribution, and supernova modelling, so that the formation of compact binaries is a genuine statistical process and the rate of coalescences largely undetermined.

Within the scenario of primordial field binary formation, the effect of metallicity was anticipated by³⁰ who pointed out that heavy black hole binaries could form in low-metallicity environments. Figure 5 shows the distribution of (NS,NS), (NS,BH*), and (BH*,BH*) mergers as a function of the chirp mass of the binary M_c (defined in the caption) from a population synthesis model and for two different metallicities. Depending on Z , whether it is solar or sub-solar, the expected number of compact binaries in all their arrangements changes dramatically, with black holes filling the high end of the mass distribution in the low metallicity channel. In the upper panel of Figure 5, we show the broad distribution of delay times as a function of the chirp mass. The *delay time* is defined as the time it takes a binary to coalesce since its formation as primordial stellar system. The distribution of delay times is broad, going from a Myr up to 10^9 Myr. In general, population synthesis models suggest that the delay times follow a power-law distribution with slope -1 , in the interval from 10 Myr up to 10^4 Myr, i.e. a uniform distribution for logarithmic bin. In the context of primordial, isolated binaries, Belczynski et al.³⁷ find that the typical channel for the formation of GW150914 like binaries involves two very massive stars $40\text{-}100 M_\odot$ formed in a low metallicity environment with $Z < 0.1 Z_\odot$ that interacted once through stable mass transfer and once through a phase of common envelope evolution, with both black holes forming without no supernova display

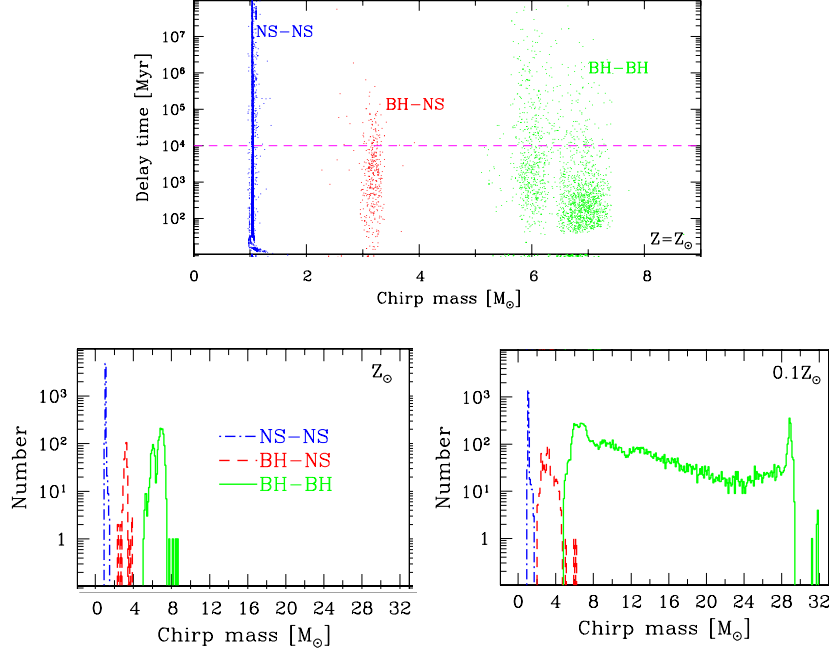


Figure 5: Upper panel: Distribution of (NS,NS), (NS,BH*), and (BH*,BH*) delay times as a function of the chirp mass $M_c = \nu^{3/5} M$ of the binary, where M is the total mass, μ the reduce mass and $\nu = \mu/M$ the symmetric mass ratio ($\nu = 0.25$ for equal mass binaries). (For equal mass (NS,NS) binaries the chirp mass is $\sim 1.2 M_\odot$.) The plot rearranged from³¹ refers to a simulated population of primordial binaries of solar metallicity. Note that the delay time to coalescence can by far exceed the age of the universe (horizontal dashed line). Lower panels depict the distribution of compact binaries that form in the three different flavours as a function of the chirp mass M_c , for two different metallicities: solar (sub-solar) in the left (right) panel. The chirp mass of GW150914 is $27.9 M_\odot$ and that of GW151226 is $8.9 M_\odot$. Courtesy of T. Bulik.

and low natal kick.

Recently and again in the context of primordial binaries, an alternative channel has been proposed for the origin of GW150914, named MOB (massive over-contact binary), which involves two very massive low-metallicity ($Z \sim 0.1 Z_\odot$) stars in a tight binary which remains fully mixed due to their high spins induced by orbit synchronism driven from tides.^{44,50,53} Rotation and tides transport the products of hydrogen burning throughout the stellar envelopes, enriching the entire star with helium and preventing the build-up of an internal chemical gradient. In this scenario there is no giant phase: both stars remain in stable

contact filling their Roche lobes and eventually form two massive black holes, because the cores that collapse are massive.

Compact binaries can also form in dense, young star clusters or globular clusters and galactic nuclei, via dynamical processes.⁴⁷ The high stellar densities, of the order of 10^{3-6} stars pc⁻³, present in star's clusters, favour the formation of black hole binaries via exchange interactions with other stars.⁵⁴ In particular three body exchange interactions $(\text{BH}^*, \text{star}) + \text{BH}^* \rightarrow (\text{BH}^*, \text{BH}^*) + \text{star}$ can lead to the built up of a population of massive compact object binaries.⁴⁸ Being the heaviest objects in the cluster, these binaries mass segregate at the cluster centre on a timescale shorter than the two-body relaxation time, and continue to experience exchange encounters with other black holes that can further rearrange them in progressively heavier binaries, that can be as massive as GW150914.⁴⁶ Hardening due to scattering off stars can drive these binaries to coalesce within $\sim 1 - 10$ Gyr, and may also escape the parent cluster due to dynamical recoil.^{47,48}

4.3 Massive black holes in the realm of observations

There is compelling evidence that besides stellar origin black holes, there exists a substantial population of *supermassive* black holes of $10^5 M_\odot - 10^9 M_\odot$ that inhabit the centres of galaxies. This "other flavour" is observed in two states: an *active* and a *dormant* state.^{55,56}

Active supermassive black holes are *accreting* black holes at the centre of galaxies, which power the luminous, highly variable QSOs, and the less luminous Active Galactic Nuclei (AGN). The accretion paradigm states that outside the event horizon of a supermassive black hole, radiation is generated with high efficiency ($\varepsilon_{\text{acc}} \sim 10\%$, higher than nuclear reactions) through the viscous dissipation of kinetic energy from gas orbiting deep in the gravitational potential of the hole. The energy escapes in the form of radiation, high velocity plasma outflows, and relativistic particles to produce luminosities of $10^{44} - 10^{47}$ erg s⁻¹ emitted over a wide spectrum and in 10% of the cases in the form of collimated radiation.

Dormant supermassive black holes appear ubiquitous in nearby bright galaxy spheroids. When dormant, their presence in inactive galaxies is revealed, albeit indirectly, through the measure of Doppler displacements in the spectral lines of stars and/or gas in the nuclear region of the galaxy. Often line-of-sight velocities show a Keplerian rise attributed to the presence of a point like gravitational potential dominating that of stars in the centre-most region of the galaxy. The Galactic Centre provides the most compelling evidence of a supermassive black hole. The Milky Way hosts a $4 \times 10^6 M_\odot$ "dark object" surrounded by a swarm of stars in Keplerian motion as close as $(1 - 10) \times 10^3 R_S$. The distance of the nearest star to the central object poses a lower limit on its compactness, found of the order of $10^{15} M_\odot$ pc⁻³.⁵⁷ No nuclear star cluster can remain in dynamical equilibrium at these densities, so that the black hole is the most simple and elegant hypothesis.

Figure 6 illustrates how broad is the mass distribution inferred from a sample

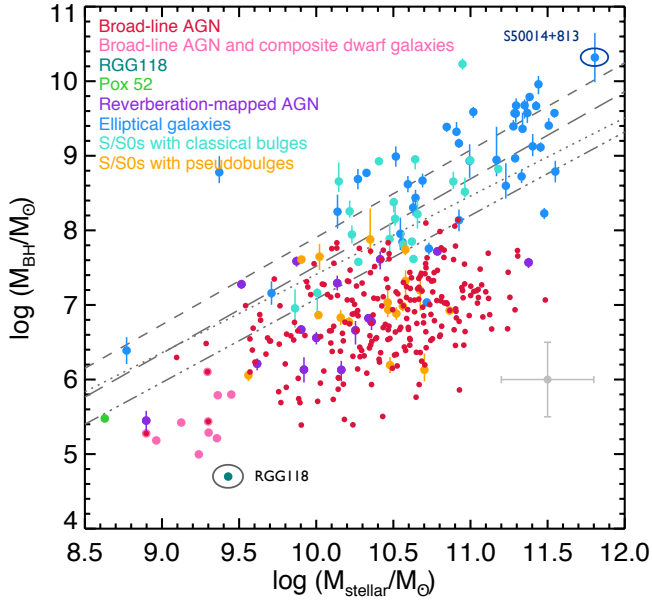


Figure 6: Black hole mass versus total host galaxy’s stellar mass. The figure rearranged from⁵⁸ illustrates the vastness of the mass spectrum of supermassive black holes residing at the centres of galaxies. The sample comprises 244 broad-line AGN, 15 reverberation-mapped AGN, and a sample of dormant supermassive black holes for which the mass is inferred from dynamical measurements. Elliptical galaxies are shown in blue, S/S0 galaxies with classical bulges in turquoise, and S/S0 galaxies with pseudo-bulges in orange points. Dashed lines show the $M_{\text{BH}} - M_*$ correlation from different authors. The two data points with a circle and associated name indicate the lightest and heaviest black holes observed as of today. Details on the plot can be found in.⁵⁸ Courtesy of M. Volonteri.

of both dormant and active close-by supermassive black holes in galaxies of different morphology, kinematics and stellar masses M_* . It extends from $5 \times 10^4 M_\odot$ (the lightest black hole discovered in RGG118) to $4 \times 10^{10} M_\odot$ (the giant black hole in S50014+831). (Recently, the mass of S50014+813 as been revised downwards to $7 \times 10^9 M_\odot$: see e.g.⁵⁹).^f

^fThe mass of the black hole M_{BH} in bright, massive spheroids correlates with properties of the host galaxy in ellipticals and S/S0s with classical bulges. Two are the correlations, the $M_{\text{BH}} - M_*$, where M_* is the stellar mass of the host galaxy, and a second (tighter) between M_{BH} and the velocity dispersion σ of the stars, measured far from the black hole.⁵⁶ These correlations (often referred to as $M_{\text{BH}} - \sigma$, and $M_{\text{BH}} - M_*$ relations, the last shown as dashed

From the study of the kinematics of stars and gas in nearby galaxies, one can estimate the black hole local mass density: $\rho_\bullet \sim (2 - 5) \times 10^5 M_\odot \text{ Mpc}^{-3}$. This mass density is remarkably close to the mass density increment $\Delta\rho_\bullet = 3.5 \times 10^5 (\varepsilon_{\text{acc}}/0.1)^{-1}$ that black holes experience over cosmic history (between $0.5 < z < 3$) due to efficient accretion.^{9,55} This last value is inferred considering that active black holes in galaxies contribute to the rise of the cosmic X-ray background resulting mostly from unresolved, obscured AGN of mass $10^8 M_\odot - 10^9 M_\odot$. As the contribution to the local black hole mass density ρ_\bullet results from black holes in the same mass range, the close match between the two independent measures, ρ_\bullet and $\Delta\rho_\bullet$, indicates that radiatively efficient accretion ($\varepsilon_{\text{acc}} \approx 0.1$) played a large part in the building of the mass of the supermassive black holes in galaxies, from redshift $z \sim 3$ to now. It further indicates that information residing in the initial mass distribution of the, albeit unknown, black hole seed population is erased during events of copious accretion, along the course of cosmic evolution. Thus, QSOs and AGN are believed to emerge from a population of *seed black holes* with masses in a range largely unconstrained (from $100 M_\odot$ up to $10^{4-6} M_\odot$). This is because the mass of black holes increases sizeably due to accretion, over a relatively short *e*-folding timescale $\tau_{\text{BH}} \approx 4.7 \times 10^8 \varepsilon_{\text{acc}} f_E^{-1} (1 - \varepsilon_{\text{acc}})^{-1}$ yr compared to the age of the universe (where $f_E = L/L_E \sim 0.1$ gives the luminosity in units of the Eddington luminosity, and $(1 - \varepsilon_{\text{acc}})$ the fraction of mass accreted by the hole in order to radiate a luminosity f_E with efficiency ε_{acc}).

The *spin* of a black hole is also a key parameter in the context of gravitational wave astronomy, as together with the mass it can be inferred from the rich structure of the waveform (as illustrated ahead in this Chapter). Mass and spin are strongly coupled across the accretion history of a growing black hole. Spins determine directly the radiative efficiency, and thus also the rate at which the black hole mass is increasing. In radiatively efficient accretion discs, the efficiency ε_{acc} varies from 0.057 (for $s_{\text{spin}} = 0$) to 0.15 (for $s_{\text{spin}} = 0.9$) and 0.43 ($s_{\text{spin}} = 1$, for a maximally rotating black hole). Accretion on the other hand determines black hole's spins since matter carries with it angular momentum (the angular momentum at the innermost stable circular orbit R_{isco}). A non rotating black hole is spun-up to $s_{\text{spin}} = 1$ after increasing its mass by a factor $\sqrt{6}$, for prograde accretion.^g Conversely, a maximally rotating black hole

or dotted lines in Figure 6: see⁵⁸ for details) state that bright galaxy spheroids with higher stellar velocity dispersions, i.e. with deeper gravitational potential wells, grow heavier black holes, and that brighter, more massive galaxies host more massive black holes. Despite being black holes tiny objects, with an influence gravitational radius $R_{\text{inf}} \sim GM_{\text{BH}}/\sigma^2$ extending out to ~ 1 pc (much smaller than the galaxy's size of tens of kpc), black holes "see" the galaxy they inhabit, and galaxies "see" the central black hole they host. Consensus is rising that the $M_{\text{BH}} - \sigma$ relation is fossil evidence of a symbiotic co-evolution of black holes and bright spheroids. Most likely, the relation was established during the course of galaxy formation and assembly in episodes of self-regulated accretion and mergers when the black holes were active, creating a balance between accretion flows with their radiated power and gas at disposal for triggering both/either star formation and accretion. The correlation is poor instead when extended to a larger sample of galaxies types and galaxy masses, indicating that particularly in lower mass systems co-evolution never got to completion, or never started.

^g Gas accretion from a geometrically thin disc limits the black-hole spin to $s_{\text{spin}}^{\text{acc}} = 0.9980$,⁶⁰

is spun-down by retrograde accretion to $s_{\text{spin}} \sim 0$, after growing by a factor $\sqrt{3/2}$.⁶²

The direction and norm of the black hole spin play a key role in the study of the spin-mass evolution of black holes. In a viscous accretion disc whose angular momentum \mathbf{J}_{disc} is initially misaligned with the spin \mathbf{S} of the black hole, Lense-Thirring precession of the orbital plane, acting on the fluid elements, warps the disc forcing the gas close to the black hole to align (either parallel or anti-parallel) with the spin vector of the black hole. The timescale for warp propagation is very rapid and the warp extends out to rather large radii.⁶³ Following conservation of total angular momentum, the black hole responds changing its spin direction \mathbf{S} . The spin starts precessing and the system evolves into a configuration of minimum energy where \mathbf{S} and \mathbf{J}_{disc} are aligned and parallel, if $S/J_{\text{disc}} < 1$. Black hole precession and alignment occur on a timescale $\tau_{\text{align}} \propto s_{\text{spin}}^{5/7}$ shorter than the e - folding accretion time scale (typically $\tau_{\text{align}} \sim 10^{5-6}$ yr).⁶⁴ If $S/J_{\text{disc}} < 1$ accretion tends to spin the black hole up after re-orienting the black hole spin. By contrast heavier black holes for which $S/J_{\text{disc}} > 1$ oppose more inertia and the spin direction does not suffer major re-orientations.^{64,65}

Two limiting scenarios for the spin evolution have been proposed: *Coherent accretion* refers to accretion episodes from a geometrically thin disc lasting for a time τ_{episode} longer than the black hole mass growth e -folding time τ_{BH} , bringing its spin up to its limiting value $s_{\text{spin}} \sim 1$, and with \mathbf{S} parallel to \mathbf{J}_{disc} . By contrast, *chaotic accretion* refers to a succession of accretion episodes that are incoherent, i.e. randomly oriented with $\tau_{\text{episode}} < \tau_{\text{BH}}$. The black hole can then be spun-up or down, depending on the comparison between \mathbf{J}_{disc} and \mathbf{S} . If accretion proceeds via uncorrelated episodes with co-rotating and counter-rotating material equally probable, the spin direction continues to change. Counter-rotating material spins the black hole down more than co-rotating material spins it up, as the innermost stable orbit of a counter-rotating test particle is located at a larger radius ($R_{\text{isco}} = 9R_G$ for $s_{\text{spin}} = 1$) than that of a co-rotating particle ($R_{\text{isco}} = R_G$ for $s_{\text{spin}} = 1$), and accordingly carries a larger orbital angular momentum. If $\tau_{\text{episode}} < \tau_{\text{align}}$ chaotic accretion results in low spins.⁶⁶

The two scenarios of coherent and chaotic are at the extremes of a wide distribution of angular momenta for the accreting gas which is determined by the kinematic and dynamical properties of gas and stars at the galaxy's centres which change over cosmic time as galaxies are not isolated systems.

At present the spin moduli of a handful (20) of AGN, hosted in low redshift late type galaxies, has been measured through the spectra of relativistically broadened $K\alpha$ iron lines, and are reported in Figure 7. The data points are then compared with a hybrid model by⁶⁵ which follows the joint evolution of the mass M_{BH} and the spin vector \mathbf{S} by precession and accretion, of a simulated population of growing black holes in late type (spiral) galaxies.

as photons emitted with angular momentum anti-parallel to the black hole spin are preferentially captured, having a larger cross section. In a magnetised, turbulent thick disc, the spin attains an equilibrium value $s_{\text{spin}}^{\text{acc,mag}} \simeq 0.93$.⁶¹

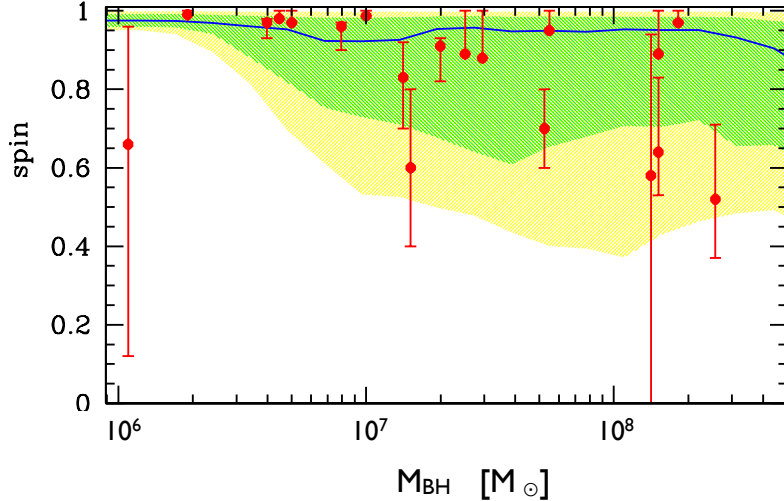


Figure 7: Comparison between measured spins from a sample of AGN (red dots) and predictions of a model by⁶⁵ from a simulated sample of accreting massive black holes (with Eddington ratio $f_E \gtrsim 0.01$) in spiral galaxies. The observational data appear to disfavour both coherent accretion along a fixed direction and chaotic (isotropic) fuelling. When the properties of the accretion flow are anchored to the kinematics of the host galaxy, a combination of coherent and incoherent accretion phases best describes the data.

Mass and spin are directly encoded in the gravitational wave signal emitted during the merger of massive black holes, and mergers are detectable with space-borne detectors out to very large cosmological distances. Therefore, measuring the masses and spins of coalescing black holes over cosmic time will offer unprecedented details on how they have been evolving via repeated episodes of accretion and mergers.

4.4 The black hole desert

There is a black hole *desert* in the mass range between $\sim 65 M_\odot$, the mass of the remnant black hole in GW150914 (the highest known as of today) and the mass of the lightest supermassive black hole known at the centre of the dwarf galaxy RGG118, of $5 \times 10^4 M_\odot$, as depicted in Figure 8. Key questions arise that the new gravitational wave astronomy can answer:

- Is the desert real, i.e. empty of middle sized black holes, or is the desert inhabited by black holes which we still do not detect?
- If inhabited, is the desert populated by transition objects, resulting from the clustering/accretion of stellar black holes viewed as single building blocks?
- Or is there a "genetic divide" between stellar origin black holes and massive black holes growing from seeds of unknown origin?
- What is the maximum mass for a stellar origin black hole^{○○}?
- Is there a gap in the mass function of stellar origin black holes induced by pair-instability supernovae?

^{○○}(Here a *maximum mass* for a stellar origin black hole $M_{\max}^{\text{BH}*}$ is intended not as fundamental mass limit (as in the case of neutron stars) but as a value related to the existence of a limit on the maximum mass M_{\max}^* of stars on the zero-age main sequence.^{67–69})

To elaborate more on the above questions we notice that there is a conceptual distinction between stellar origin black holes and supermassive black holes: the first are the relic of the very massive stars that experienced stable and long lived episodes of nuclear burning. The second are possibly the relic of rare supermassive stars that may never experienced long-lasting phases of nuclear burning and which formed in rather extreme, isolated environments. There is also a "morphological" distinction: stellar black holes (typically more than several millions per galaxy) are spread everywhere in all the galaxies of the universe, as stars are. In addition, they continue to form as stars do, in the galaxies. Instead, massive black holes (from the middleweight size to the giants) are found at the centres of galaxies (perhaps not in all), as single dark massive objects, and may have formed at early cosmic epochs or over a narrower interval of cosmic times, when the first galaxies were forming and assembling.⁷⁰ If the desert is devoid of objects, this would unambiguously indicate that the physical conditions leading to the two flavours are distinct. Locating the dividing line is not easy.

Massive stars with sub-solar metallicities and masses between $\sim 100 M_{\odot}$ and $\sim 260 M_{\odot}$ explode as pair instability supernovae.^{34,69,71} The pair instability is encountered when, late in the star's life, a large amount of radiative energy is converted into electron-positron pairs which reduce the pressure support against gravity, cause rapid contraction of the core and trigger explosive burning of the CO core, ultimately leading to the disruption of the star. Thus, if the IMF is devoid of stars with mass in excess of $\sim 260 M_{\odot}$, pair instability supernovae may actually limit the value of the maximum mass of a stellar origin black hole $M_{\max}^{\text{BH}*}$.⁶⁹ In the four panels of Figure 9, the mass of the relic black holes (red line) is plotted versus the initial mass of the progenitor star, for two selected

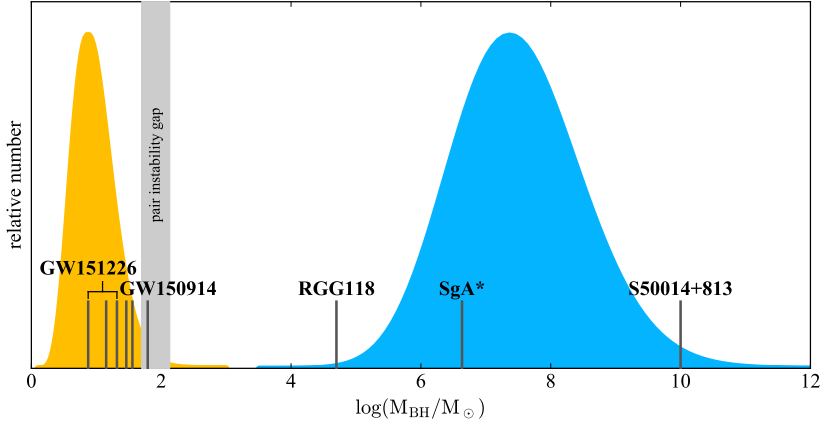


Figure 8: A pictorial representation of the black hole mass function (modelled as a log-normal distribution), encompassing the mass intervals known, from stellar origin black holes to massive and giant black holes at the centre of galaxies, to illustrate the presence of a *desert* at intermediate mass scales. Vertical lines denote the black hole masses in GW150914 and GW151226 (including the mass of the new black hole, result of the merger) and the smallest and largest mass of the two active black holes known as of today in galaxies. The grey vertical strip denotes the region of Pair instability Supernovae that leave no remnant.^{34,69} Advanced LIGO and Virgo jointly with LISA in space will shed light into the physical mechanisms that lead to the formation of heavy stellar black holes and black hole seeds covering the desert zone.

values of the metallicity, $Z = Z_{\odot}$ and $Z = 0.016Z_{\odot}$ respectively, for both non-rotating stars and rapidly rotating stars (with velocity 300 km s^{-1}). At sub-solar metallicities the maximum mass of the relic black hole coasts around values $\sim 60 M_{\odot}$ almost independently on rotation and on metallicity, provided is sub solar ($Z < 0.1 Z_{\odot}$).⁷² As shown in the bottom right panel, rapid rotation limits again $M_{\max}^{\text{BH}*} \sim 50 M_{\odot}$, and this occurs at lower progenitor masses $\sim 70 M_{\odot}$. During core He burning, rotation driven mixing causes diffusion of matter from the He convective core into the surrounding radiative zones. Such an occurrence has the consequence of increasing the CO core mass at core He depletion and therefore of reducing the limiting initial mass that enters the pair instability regime. If the IMF is top heavy and contains stars in excess of $260 M_{\odot}$, a gap between $50 M_{\odot}$ and $135 M_{\odot}$ (the He mass inside a $260 M_{\odot}$ star⁷¹) should appear in the mass function of (single) stellar origin black holes, as anticipated in.⁶⁹ Advanced LIGO and Virgo will likely help to shed light into this problem, if/when "heavy" stellar binary black hole mergers will be further discovered.

In the logic of a "genetic divide", supermassive stars likely play a key role. The formation of radiation dominated equilibrium states with masses

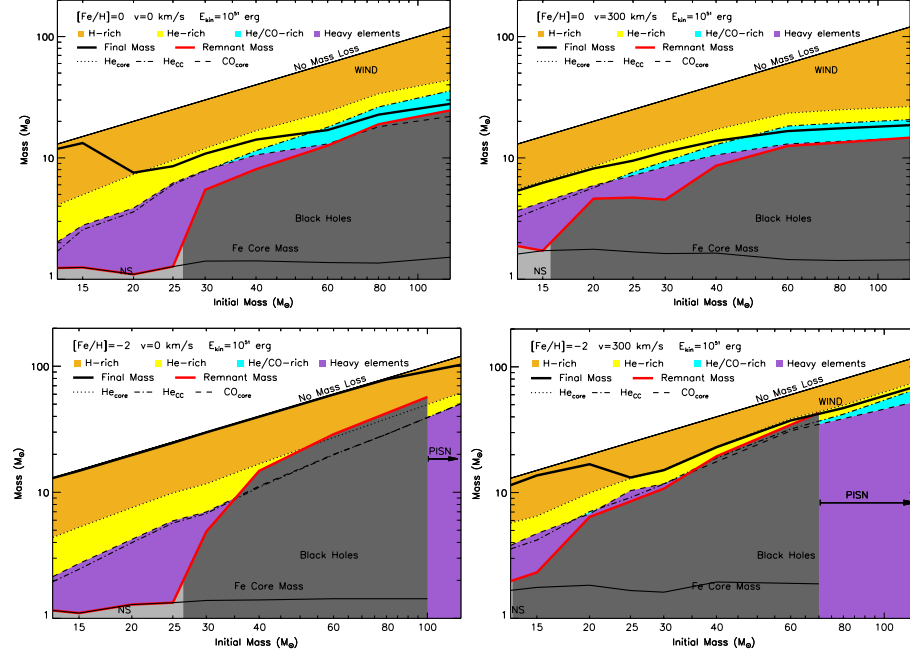


Figure 9: Global properties of a generation of massive stars as a function of the metallicity.⁷² The red line in each panel gives the mass of the remnant versus the initial mass (in M_{\odot}). In the legend symbols and colours describe the mass of different elements from hydrogen to iron inside the relic star prior to core collapse. Upper panels refer to stars of solar metallicities $Z = 0.02$ ($[Fe/H]=0$), and rotation velocities of $V = 0 \text{ km s}^{-1}$ (left), $V = 300 \text{ km s}^{-1}$ (right). At solar metallicities, mass losses by winds inhibit the growth of a massive CO core and the pair instability is never encountered. The large mass losses also limit the mass of the relic black hole to values $< 20 M_{\odot}$. Lower panels refer to stars with $Z = 3.236 \times 10^{-4}$ ($[Fe/H]=-3$) which encounter the pair instability supernova (PISN). The black hole maximum mass is close to $60 M_{\odot}$, depending weakly on rotation, and it is attained at the threshold of PISN. The figures are adapted from the chapter "Supernovae from massive stars" by M. Limongi in "Handook of Supernovae", edited by Springer. Courtesy of M. Limongi.

$\gtrsim 10^5 M_{\odot}$,²⁵ evolving into a DCBH, i.e. a configuration collapsing directly into a black hole, requires rather extreme conditions to form,⁷³ (i) namely pristine, metal free gas clouds (site of the forming supermassive star) irradiated by an intense flux of ultraviolet radiation to promote the dissociation of the main coolant, i.e. molecular hydrogen, and avoid fragmentation;^{23–25} or/and (ii) the coherent collapse of massive gas clouds in major galaxy mergers.⁷⁴ These sce-

narios would lead to a clean divide between the two black hole flavours, but Nature appears to be more complex and continuous.

There is indeed the possibility that the desert is filled of *transition* black holes.⁷⁰ Processes of aggregation might have been in action, e.g. using as *single building blocks* stellar origin black holes which merge inside nuclear star clusters.⁷⁵ Alternatively, episodes of supercritical accretion may drive stellar origin black holes to grow up to "seed" sizes of $10^3 M_\odot$ when residing in gas rich disk galaxies.⁷⁶ Photon trapping ensures that the momentum from outgoing radiation does not feed back to halt accretion which can continue until fuel exhaustion. In these cases, the desert zone would be filled by transition black holes with a broad range of masses between 100 and $1000 M_\odot$ or more.

Runaway collisions among massive stars, in young, dense nuclear star clusters at the centre of unstable proto-galactic discs^{45,77,78} may also lead to middleweight black holes. The resulting runaway super-massive star, product of the multiple merger of stars (typically of mass $\lesssim 10^3 M_\odot$) may evolve into a *quasi-star*, i.e. a black hole surrounded by a massive accretion envelope,⁷⁹ ultimately forming a black hole of intermediate mass.⁸⁰ Detecting black hole coalescences of different flavours with both Earth and space-based detectors will enable us to shed light into this complex problem.

4.5 Formation of gravitational wave sources: the cosmological perspective

In this short paragraph, we show that the existence of close pairs of massive black holes fated to coalesce is a key, unescapable prediction of the process of clustering of cosmic structures, and that the formation of close binary systems comprising stellar origin black holes and neutron stars has a natural connection with the overall star formation history in the universe. The progenitor stars of GW150914 may have formed in a binary ~ 2 Gyr after the Big Bang (at $z \sim 3$) in a metal poor environment, according to.³⁷

A plethora of observations show that today the energy content of our expanding universe is dominated by dark energy (68.3%), and by cold dark matter (CDM, 26.8%), with baryons contributing only at 4.9% level,⁸¹ and that the present spectrum of primordial density fluctuations contains more power at lower masses. At the earliest epoch, the universe was dominated by small scale density fluctuations. Regions with higher density grow in time to the point where they decouple from the Hubble flow and collapse and virialize, forming self-gravitating halos. The first dark matter halos that form grow bigger through mergers with other halos and accretion of surrounding matter along cosmic filaments. This is a bottom up process which leads to the hierarchical clustering of dark matter sub-structures and of the luminous components, the galaxies.⁷³

At present, most of the investigations of galaxies and of QSOs in the electromagnetic universe feature the occurrence of three main epochs of evolution, along cosmic history:⁸²

- The *cosmic dawn* which is the epoch extending from cosmic redshift $z \sim 15$ when the universe was only a few 100 Myr old to redshift $z \sim 6$, corresponding

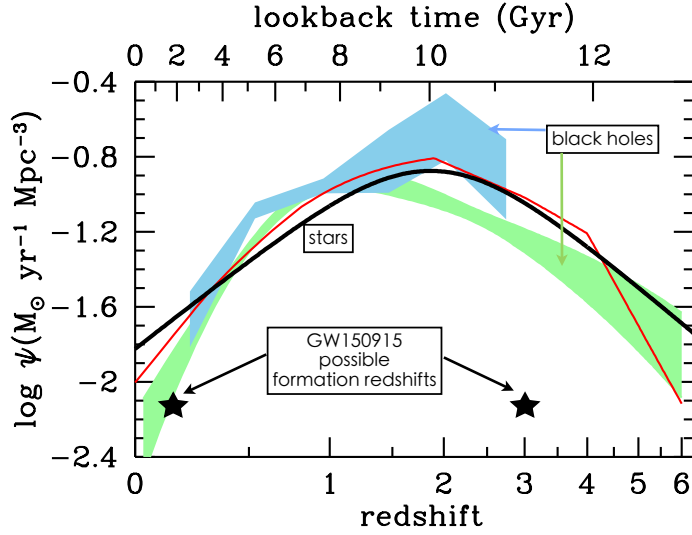


Figure 10: Comparison of the best-fit star formation history (thick black solid curve) with the massive black hole accretion history from different data (shaded green, light blu, and red line), adapted from.⁸² The shading indicates the $\pm\sigma$ uncertainty range on the total bolometric luminosity density. The comoving rates of black hole accretion have been scaled up by a factor of 3,300 to facilitate visual comparison to the star-formation history. The two black stars indicate the possible redshifts of formation of the progenitor binary to the GW150914 event, as calculated in.³⁷ Courtesy of P. Madau.

to $\lesssim 1$ Gyr. During this epoch, baryons in dark matter halos of $\gtrsim 10^6 M_\odot$ begin to collapse and the first stars form and first seed black holes. Planck data indicate that between $z = 7.8$ and 8.8 the universe completed the phase of cosmic *re-ionisation* of gas turning intergalactic neutral hydrogen into a hot tenuous plasma.⁸³ At the limits of current capabilities, GRB 090423, the farthest long GRB observed (which signals the formation of a stellar origin black hole), exploded at $z = 9.4$, when the universe was 520 Myr old, and the most distant galaxy MACS0647-JD 420 and the most distant QSO ULAS J1120+0641 are found at $z = 10.7$ and $z = 7.07$, 420 and 770 Myr after the big bang, respectively.⁹ These brightest sources are just probing the tip of an underlying distribution of fainter early objects for which little is known and which represent the building blocks of the largest structures.

- The cosmic high noon follows, which is an epoch of critical transformations

for galaxies, extending from $z \sim 6$ to 2. Around $z \sim 2$, the luminous QSOs and the cosmic-integrated star formation rate have their *peak*. This is illustrated in Figure 10 where we show the cosmic-averaged star formation rate per unit comoving volume (in units of $M_\odot \text{ yr}^{-1} \text{ Mpc}^{-3}$) and the massive black hole accretion history (in the same units but enhanced by a factor 3,300 to help the comparison) as function of lookback time and redshift. Galaxies and seed black holes are expected to grow fast in this epoch which erases information of their properties at birth. In between redshift 1 and 2, galaxies acquire about 50% of their mass, and widespread star formation can lead to the build up of populations of (NS,NS), (NS,BH*) and (BH*,BH*) fated to coalesce over cosmic time, and accessible to forthcoming and future observations.

- The last epoch of *cosmic fading* traces a phase where star formation in galaxies, and QSO's activity in galactic nuclei are both declining. It is a phase of slow evolution extending from $z \sim 1$ to the present. Observations of galaxies and AGN give a description of a quieter universe where dormant supermassive black holes lurk at the centre of bright elliptical galaxies likely formed through galaxy mergers. Less massive (dwarf) galaxies in the near universe have undergone a quieter merger and accretion history than their brighter analogues (which formed earlier). They represent the closest analogue of lower mass high redshift dark matter halos from which galaxy assembly took off during cosmic dawn. Local, dwarf galaxies are the preferred site for the search of middleweight (or intermediate) black holes of $10^{3-6} M_\odot$.⁸⁴ NGC 4359, a close-by bulgeless disk dwarf, houses in its centre a black hole of only $3.6 \times 10^5 M_\odot$. This indicates that nature provides a channel for the formation of middleweight black holes also in potential wells much shallower than that of the massive spheroids, and these galaxies are expected to host a class of gravitational waves sources, known as Extreme Mass Ratio Inspirals (EMRIs) that we will discuss ahead in this Chapter.

A number of important questions can be posed in the context of galaxy formation and evolution that the gravitational universe will try to answer:

- When did the first black hole seeds form? Did they form only during cosmic dawn, i.e. over a limited interval of cosmic time?
- How does the black hole mass and spin distribution evolve with cosmic time?
- To what extent mergers affect the cosmic evolution of massive black holes?

4.6 Massive black hole binary mergers across cosmic ages

During cosmic dawn and high noon, the bottom-up assembly of galactic halos through galaxy mergers inevitably lead to the growth of an evolving population of binary black holes in a mass range between $10^{4-7} M_\odot$. These are the target sources of the upcoming LISA-like observatory, in space. When two galaxies

with their dark matter halos merge, the time-varying gravitational field induced by the grand collision redistribute the orbital energy of stars and gas discs in such a way that a new galaxy with new morphology forms. At the same time, the black holes nested at the centres of the interacting galaxies have a long journey to travel before entering the phase of gravitational driven inspiral.⁸⁵ They experience four critical phases covering more than 10 orders of magnitude in dynamic range:

- (1) The *pairing phase*, when the black holes pair on galactic scales following the dynamics of the galaxies they inhabit until they form a Keplerian binary (on pc scales) when the stellar/gas mass enclosed in their relative orbit is comparable to the sum of the black hole masses. In this phase, the two galaxies first sink by dynamical friction against the dark matter background to form a new galaxy dragging the two black holes at the centre of the new system. Then, the black holes experience, as individual massive particles, dynamical friction against the stars/gas and continue to spiral in and sink.
- (2) *The binary or hardening phase*, when single stars scattering off the black holes extract tiny amount of their orbital energy and angular momentum. If present in large numbers, the binary continues to contract. In gas-rich galaxies, torques from a circum-binary gaseous disc surrounding the binary can also lead to hardening.
- (3) The third phase of *gravitational wave driven inspiral* starts when the black holes get so close (typically at around or below $\sim 10^{-3}$ pc) that they detach from their nearest environment, and gravitational waves dominate the loss of energy and angular momentum driving the binary to coalescence.
- (4) Finally the new black hole that formed may experience a *recoiling phase* since gravitational waves carry away linear moment. Gravitational recoil velocities are between $\sim 300 \text{ km s}^{-1}$ and $\sim 4000 \text{ km s}^{-1}$.⁸⁷ Thus the new black hole can either oscillate and sink back to the centre of the relic galaxy, or escape the galaxy. Only state-of-the-art numerical simulations can describe this long journey that begins at 10 kpc scales and ends when the two black hole coalesce, typically on scales of 10^{-6} pc. The *delay* between the galaxy merger and black hole merger varies from Myr to many Gyrs.⁸⁵ Figure 11 from⁸⁶ shows the three phases of a merger of two galaxies belonging to a group from a cosmological simulation (see the caption for details).

The merger of black holes in pristine dark matter halos is even more difficult to simulate as the dynamics is dominated by the gas and this requires use of self-consistent high resolution hydrodynamical cosmological simulations with rich input physics (chemistry network, cooling and radiative transport, turbulence and magnetic field dissipation) over a wide dynamical range. Preliminary studies indicate that the black hole dynamics is stochastic,⁸⁸ implying a rather broad range of sinking timescales.

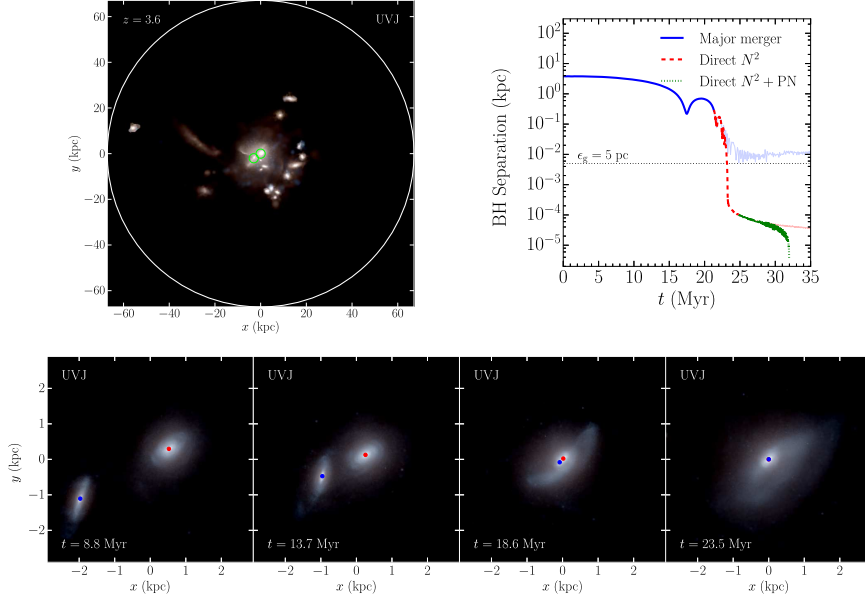


Figure 11: Group environment of a galaxy merger simulated by.⁸⁶ The left upper panel shows a mock UVJ map of the galaxy group at redshift $z = 3.6$. The white circle marks the virial radius of the group halo, while the green circles mark the galaxies in the verge of merging which host a massive black hole. The right upper panel shows the black hole separation versus time. Notice the huge dynamical range covered by this simulation, going from a few kpc down to a separation of 5 pc (horizontal dotted line - pairing phase) corresponding to the force resolution of the large scale hydrodynamical simulation. Below 5pc the continued direct N-body simulation guarantees that repeated scatterings with stars drive the binary down to 0.1 pc (red dashed line - binary/hardening phase), and that Post Newtonian corrections in the dynamics (blu dotted line - gravitational driven phase) drive the binary to coalescence within ~ 30 Myr after the formation of the oblate remnant, galaxy. The lower panel shows, from left to right, the time evolution of the galaxy merger depicted using mock UVJ photometric images of the merger, and the red and blue dots mark the position of the primary and secondary black hole, respectively. Lengths are in physical coordinates. We defer to⁸⁶ for details. Courtesy of F. Khan.

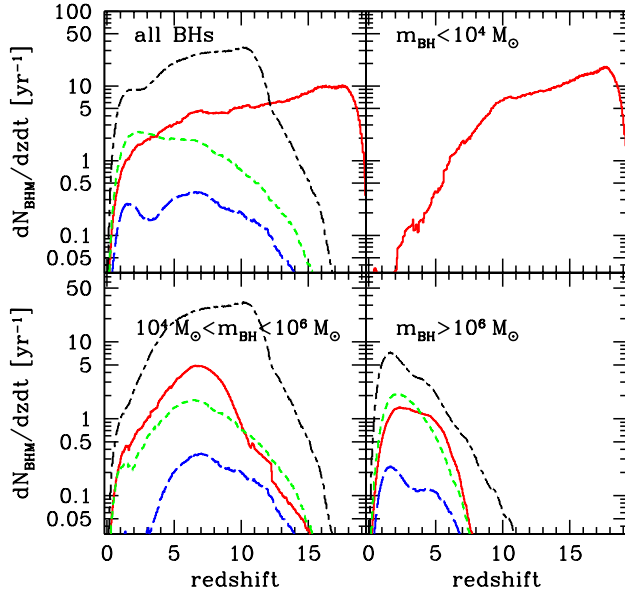


Figure 12: Differential merger rates (per unit redshift and time expressed in yr) versus redshift for different black hole seed formation scenarios, from.⁸⁹ Two main scenarios for black hole formation are considered: one where seeds are remnant of Population III stars of $\sim 100 M_{\odot}$, and one where seeds form with masses of $\sim 10^4 M_{\odot}$. The black holes then continue to evolve due to accretion: see⁸⁹ for details. Note how the lack of a physical understanding of the black hole seed formation mechanisms and their relation with the environment and cosmic epoch makes these rates highly uncertain.

4.6.1 Reconstructing the cosmic evolution of massive black hole binary coalescences across the ages

Given a mass distribution of black hole seeds, a cosmological model for the growth and assembly of dark matter halos, and an accretion recipe, one can infer the merger rates of massive black holes. In Figure 12 we show the merger rate per redshift bins of black holes as a function of z , for a variety of models of black hole seed formation, from Pop III stars to relic of supermassive stars collapsing as DCBH, computed using a Monte Carlo merger tree synthesis model within the extended Press and Schechter formalism for the assembly of galaxy halos.⁸⁹ The uncertainties are large with merger rate excursions of about two orders of magnitude, ranging from ten to several hundreds events per year. Each halo had experienced few to few hundred mergers in its past life, placing mergers

among the critical key mechanisms driving galaxy evolution.

5 The sources of the gravitational wave universe

Here we list the prospected sources of the gravitational wave universe, based on two criteria: the distinction between *high* and *low* frequency sources, and between *short duration*, *transient* and *continuous* sources. The concept of *backgrounds* is shortly introduced.

5.1 The high frequency gravitational universe

The sources of the *high frequency universe*, observed with ground-based detectors at frequencies between ~ 10 Hz and to a few 1000 Hz (~ 1 and $\sim 10^4$ Hz with the Einstein Telescope under design), can be grouped into four basic classes: compact binary coalescences, un-modelled bursts, continuous waves, and stochastic backgrounds.^{7,8,10} These groups refer to different astrophysical settings and different algorithms for their detection.

- **Compact Binary Coalescences** - CBCs refer to binaries hosting the relics of massive stars and comprise (NS,NS),(NS,BH*) and (BH*,BH*) binaries. CBCs are *transient* sources. They are detectable at the time of their coalescence, as they emit a sizeable fraction of their reduced-mass-energy, and have a modelled signal. (NS,NS) binaries are characterised by mass ratios $q \equiv m_2/m_1$ (with $m_2 < m_1$) close to ~ 1 , as observed in double neutron star binary systems, and a lower limit is $q \sim 1.4 M_\odot/M_{\max}^{\text{NS}} \sim 0.46$. The mass ratio of (NS,BH*) and (BH*,BH*) binaries is less constrained, since we do not know the maximum mass of stellar black holes nor how they pair in binaries. GW150914 and GW151226 have mass ratio ~ 0.82 and ~ 0.53 , respectively.^{2,5} GW150914 and GW151226 are expected to be the first two of a rich population of CBCs of different flavours that will be observed in the forthcoming Advanced LIGO and Virgo science runs. In §6 and §7 we describe in depth CBCs and their expected signal.

Horizon luminosity distance - A key fact that makes binaries important sources is that the amplitude of the emission is calibrated just by a combination of the two masses (to leading orders). Given this, their detectability can be expressed in terms of the horizon luminosity distance d_{horizon} for a detector, defined as the distance at which a detector measures a signal-to-noise ratio (SNR) of 8 for an optimally oriented (face-on) and optimally located binary. Figure 13 indicates this distance reach for Advanced LIGO in three of its design configurations. At present the distance reach for (NS,NS) binaries with Advanced LIGO and Virgo is ~ 90 Mpc, and ~ 400 Mpc for (BH*,BH*) binaries. At design sensitivity Advanced LIGO can detect neutron star binaries out to a distance of ~ 400 Mpc scales, and black hole binaries as GW150914 out to $\lesssim 10$ Gpc, as shown in the figure. Black holes of intermediate mass can also be detectable, if they form in binaries over this mass range. We remark that all these binaries would not be detectable otherwise (neutron star binaries are observed as pulsars only in

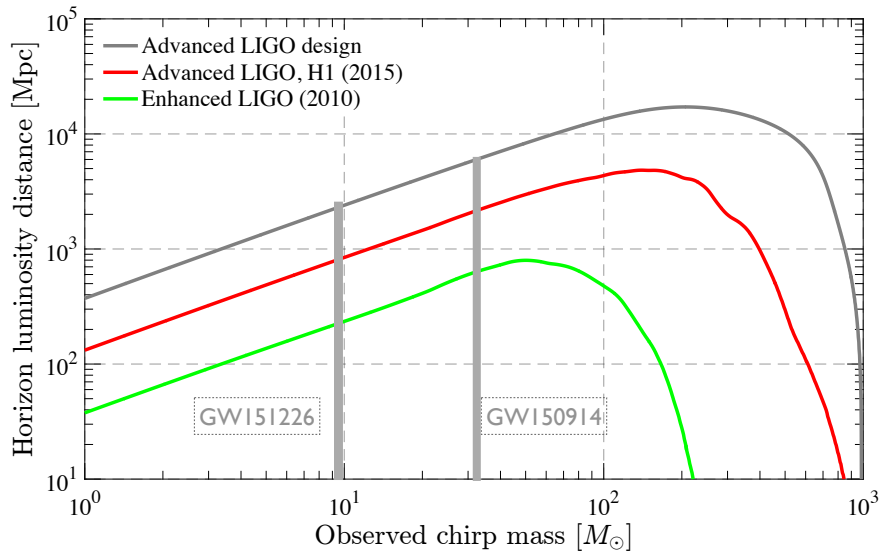


Figure 13: Horizon Luminosity distance reach of CBCs as a function of the detector-frame chirp mass (we defer to §6 of this Chapter for the definition of the chirp mass for binaries at cosmological distances). The Figure is adapted from.⁹⁰ The distance is computed for equal-mass binaries including the inspiral and merger signal. (NS,NS) binaries have observed chirp masses $\mathcal{M}_c \simeq 1$, while (BH*,BH*) binaries have \mathcal{M}_c which exceed unity. Light-grey lines refer to GW150914 and GW151226 which have detector-frame chirp masses of $\sim 30.2 M_\odot$, and $9.7 M_\odot$, respectively. The range of chirp masses includes also the possibility of detecting intermediate mass black holes in binaries, if they exist with $\mathcal{M}_c > 100$. The curves refer to three different stages of the Advanced LIGO design as indicated in the figure. A source at redshift $z = 0.01$ ($0.1, 1$) has luminosity distance of 43 Mpc (463 Mpc, 2.8 Gpc) according to the present cosmological model. Courtesy of the LIGO Scientific Collaboration.

our Milky Way). The third generation of Earth based detectors as ET will be able to detect (NS,NS) out to redshift $z \sim 2$ corresponding to a distance of 1.6 Gpc, and (BH*,BH*) as GW150914 out to a redshift $z \sim 5$ (47 Gpc) allowing ET to explore binary populations at cosmological distances, at the end of the cosmic dawn and during high noon.

Expected coalescence rates - Prior to the discovery of GW150914, the rate of CBCs relied entirely on theoretical population synthesis models and dynamical

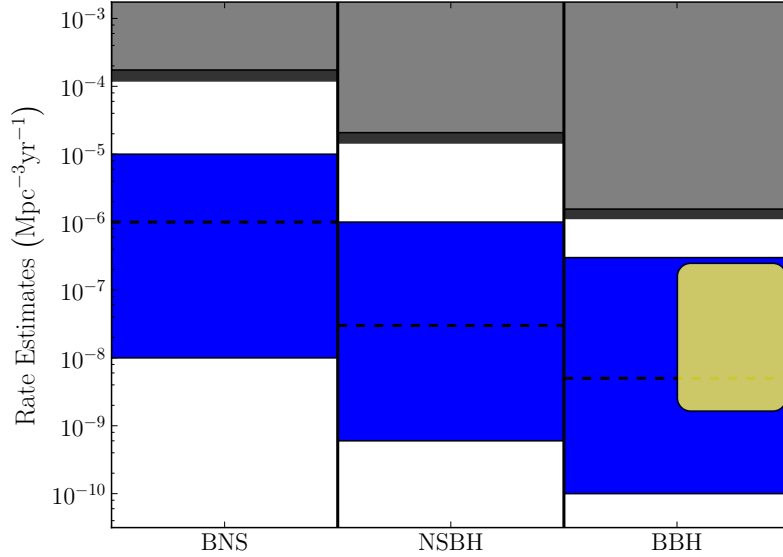


Figure 14: Comparison of merger rates of (NS,NS), (NS,BH*) and (BH*,BH*) binaries adapted from.⁹¹ The blue regions show the spread in the predicted rates with the dashed-black lines showing realistic estimates. A black hole mass of $10 M_{\odot}$ was used for estimating the rates. The grey regions display the upper limits on the rates obtained in the S5-VSR1 analysis. Following the discovery of GW150914 and GW151226, conservative estimates now fall in the dark-yellow square (see⁹² and arXiv:1606.04856v1 for further details).

models, and for (NS,NS) binaries on constraints derived from electromagnetic observations.⁹³ The rates with their large uncertainties are in Figure 14. With the discovery of GW150914, the rates for (BH*,BH*) binaries now fall in the conservative range of 9×10^{-9} and $250 \times 10^{-9} \text{ Mpc}^{-3} \text{ yr}^{-1}$ (we defer to⁹² and arXiv:1606.04856v1).

- **Unmodelled Bursts** refer to short-duration events caused by a sudden change of state in the source that do not have a near-universal waveforms. Here we outline their key features.

Core collapse supernovae (CCSNa) and *hot remnants* belong to this class.^{94,95} In CCSNa, among the most powerful explosions in the electromagnetic universe, the available energy reservoir of $3 \times 10^{53} \text{ erg}$ is set by the difference in gravitational binding energy between the pre-collapse iron core and the collapsed neutron star remnant. Much of this energy is initially stored as heat

in the proto-neutron star and most of it (99%) is released in the form of neutrinos, 1% in kinetic energy of the explosion, 0.01% is emitted in radiation across the electromagnetic spectrum, and an uncertain fraction is expected to be emitted in gravitational waves. Electromagnetic observations of CCSNae yield secondary observables, such as progenitor type and mass, explosion morphology and energy, and ejecta composition. By contrast, gravitational waves, much like neutrinos, are emitted from the innermost region (the core) of the CCSN and thus convey primary, direct live information on the dynamics of the core collapse and bounce. They potentially inform us not only on the general degree of asymmetry in the dynamics of the CCSN, but also more directly on the explosion mechanism, the structural and compositional evolution of the proto-neutron star, the rotation rate of the collapsed core, and the state of nuclear matter.

The violent dynamics in CCSNae and (possibly) in long GRBs (resulting from the collapse of rapidly rotating low-metallicity massive stars, dubbed as collapsars) is expected to give rise, if aspherical, to low amplitude bursts of gravitational waves with typical durations from milliseconds to seconds, over a wide frequency range, between 50–1000 Hz. The bursts have no universal features as gravitational wave emission is influenced by the stochastic dynamics driven by the richness in the input physics that accompany the infall of matter and its bounce. Many multi-dimensional processes may emit gravitational waves during core collapse and the subsequent post-bounce CCSN evolution. In §7 we select a few mechanisms that lead to the emission of gravitational waves, and show the shape of the signal.

The proto-neutron star that forms at the end of a CCSN is a hot and rapidly evolving object. After the first tenths of seconds of the remnants life, the lepton pressure in the interior decreases due to extensive neutrino losses, and the radius reduces to about 20–30 km. The subsequent evolution is quasi-stationary, and can be described by a sequence of equilibrium configurations. In these states the hot star can display a rich spectrum of non-radial normal modes, which can excite emission of gravitational waves in narrow intervals around the characteristic frequency of the mode, and extending over times comparable to the damping timescale of the excited oscillation mode.⁹⁶ CCSNae should be visible throughout the Milky Way with enhanced interferometric detector technology, while third generation observatories may be needed to explore events at a few Mpc, out to which the integrated CCSNae rate is $\sim 0.5\text{--}1 \text{ yr}^{-1}$. Detecting gravitational waves in coincidence with optical, X-ray, γ -ray radiation or neutrinos could give unprecedented insight into stellar collapse.

Pulsar glitches are also expected to fall in this category. Glitches are enigmatic spin-up events seen in (mainly) relatively young neutron stars like Crab and Vela. A glitch is a sudden increase (up to 1 part in 10^6) in the rotational frequency of a pulsar. Following a glitch is a period of gradual recovery to a spin close to that observed before the glitch, due to braking provided by the emission of high energy particles and electromagnetic radiation. These gradual recovery periods have been observed to last from days to years. Currently, only multiple glitches of the Crab and Vela pulsars have been observed and studied exten-

sively. The energy of these events is 10^{42} erg, i.e. of the order of $10^{-12} M_{\odot}c^2$, which set a benchmark energy level for the emission in gravitational waves by pulsars. These events are likely to be within reach of ET, but still too weak for Advanced LIGO and Virgo, and are observable only in the Galaxy.

Magnetar flares could be important sources of gravitational waves. Magnetars are associated to the high energy phenomena known as Soft Gamma Repeaters and Anomalous X-ray Pulsars. These sources host slowly spinning, isolated neutron stars endowed by ultra strong magnetic fields and whose emission is powered by the release of magnetic energy. On December 2004 a giant flare has been observed in SGR 1806-20 which released $\sim 5 \times 10^{46}$ erg in high energy radiation, implying an internal magnetic field strength of 10^{16} Gauss. To explain this powerful emission, models require a substantial deformation of the neutron star in a direction non coincident with its spin axis. The newborn fast spinning magnetar may radiate for a few weeks gravitational waves at frequencies around a kHz, and may constitute a promising new class of gravitational wave emitters, visible once per year from galaxies in the Virgo cluster, out to a distance of 16 Mpc.⁹⁷

Asteroseismology of neutron stars is (at least in principle) a promising avenue for studying neutron star interiors.^{96,98} Neutron stars have a rich oscillation spectrum associated to non-radial normal modes with frequencies in the kHz regime. They can be excited in different evolutionary phase, e.g. in rapidly and differentially rotating hot proto-neutron stars, or in old neutron stars recycled in binaries whose accreting layers are sites of repeated nuclear explosions that produce X-ray flares. In this last case, the rapid rise times of these instabilities may excite acoustic vibrations. If the rise time matches the period of a mode, than a substantial fraction of the energy released can be channeled into mechanical vibrations and a large fraction of this energy could be carried away by gravitational waves, when other mode-damping mechanisms (e.g. viscosity) are less efficient.

- **Continuous wave source** are generally persistent sources which produce signals of roughly constant amplitude and frequency, i.e. varying relatively slowly over the observation time. A number of mechanisms may cause the neutron star to emit a continuous signal. These include deformations generated either by strains in the star's crust or by intense magnetic fields, precession, and long-lived oscillation modes of the fluid interior. Target sources for this type of emission are the rotation powered neutron stars in the Milky Way.⁹⁹

More than 2000 radio pulsars have been detected for which the sky location and frequency evolution have been accurately measured. Among them, several tens have spin frequencies greater than 20 Hz so that they are in the Advanced LIGO and Virgo bandwidth reach. In the search of the gravitational wave signal, pulsars are assumed to be triaxial stars emitting gravitational waves at precisely twice their observed spin frequencies (i.e. the emission mechanism is an $l = m = 2$ quadrupole), with the wave phase-locked with the electromagnetic signal. No signal has been reported so far from targeted pulsars. This null result can therefore be interpreted as upper limit on the strength of the gravitational

wave emission, and thus as upper limit on the level of asymmetry seeded in the star's equilibrium structure. Theoretical modelling of bumpy neutron stars has mainly focused on establishing what the largest possible neutron star mountain would be.⁹⁸ Expressing this in terms of a (quadrupole) ellipticity, detailed modelling of crustal strains suggest $\epsilon_{\text{crust}} < 2 \times 10^{-5} (U_{\text{break}}/0.1)$ where U_{break} is the crustal breaking strain. State-of-the-art calculations indicate that solid phases may also be present at high densities, allowing the construction of stars with larger deformations. The magnetic field also tends to deform the star. For typical pulsar field strengths the deformation is $\epsilon_B \sim 10^{-12} (B/10^{12} \text{ G})^2$, but it can be larger by a factor $\sim 10^3$ if the core is super-conducting with critical field strength of 10^{15} G.⁹⁸

An observational milestone was reached recently, when the LIGO and Virgo data analysis from the first nine months of the S5 science run was carried on to beat the Crab pulsar spin-down limit. It was found that no more than 2% of the spin-down energy was being emitted in the gravitational wave channel. This limit already indicates that Crab is not a maximally strained quark star for which larger ellipticities are allowed.^{98–100}

- **Stochastic backgrounds** can arise from a large population of weak sources, so that there are many comparable strength signals with overlapping frequencies in each resolvable frequency bin. In the high frequency regime, the likely sources would be a population of inspiralling binaries at much greater distances than the resolvable CBCs. With the LIGO detection of GW150914 there might exist a population of "heavy" binary black holes with mass above $\sim 30 M_\odot$ contributing to the stochastic gravitational wave background at a level higher than previously expected from CBCs.¹⁰¹

A *stochastic background* can also arise from the *primordial gravitational waves* produced at the inflationary epoch. The standard cosmological model places this background at even lower levels than the expected foreground from unresolved binaries, but alternative models can produce strong cosmological backgrounds in different frequency bands. Consequently, non-detections can place meaningful constraints on alternative cosmological models.

5.2 The low frequency gravitational universe

The milli-Hz frequency range (between 0.1 mHz and 0.1Hz) will be probed by space based interferometers such as eLISA^{9,102^h}

^heLISA or 'evolving' LISA is, at the time of writing, a descoped version of the original LISA mission, to be flown by ESA in the early 2030s. For the purpose of our general discussion, there is no need to differentiate between the details of the two concepts. Detailed eLISA designs under consideration can be found in.¹⁷⁵

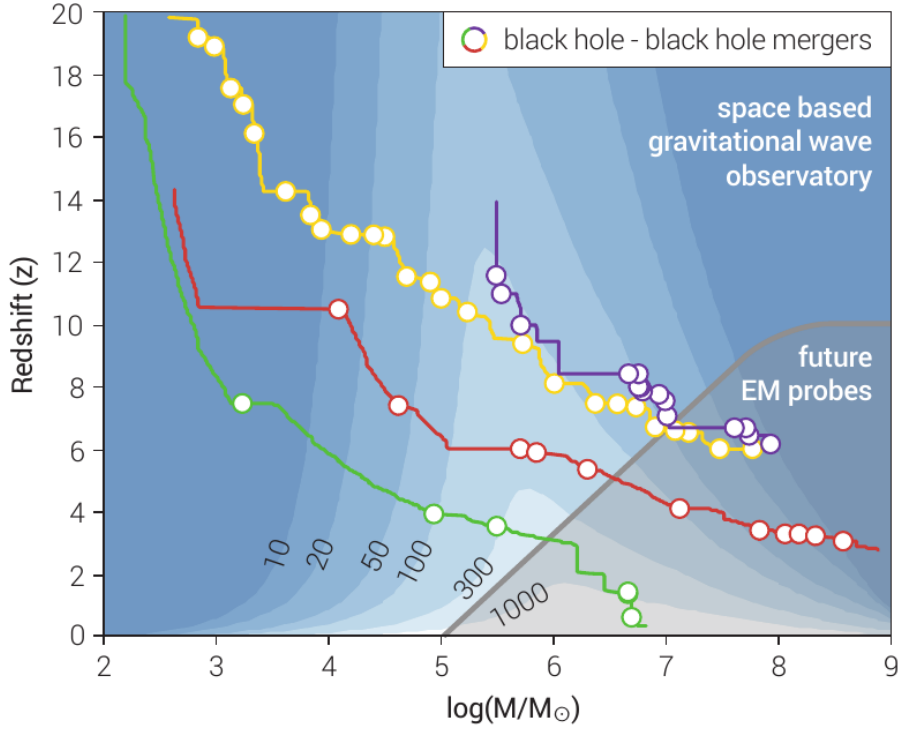


Figure 15: Contour plot of constant sky-polarization averaged signal-to-noise ratio (SNR) of equal mass, non spinning massive black hole binary coalescences in the elISA detector, plotted in the total rest-frame mass (x -axis) and redshift (y -axis) plane, from.¹⁰² Tracks represent selected evolutionary path of different MBHCs, obtained using semi-analytical population synthesis models. Circles mark MBHCs occurring along the way, whereas the bottom-right grey area identifies the portion of parameter space accessible to future electromagnetic observations of active supermassive black holes. The figure shows how complementary is the parameter space explored by eLISA. In the overlap region there might also be the possibility of detecting precursors and or electromagnetic counterparts of MBHCs.

- **Massive black hole coalescences** (MBHCs) are binaries resulting from the collision and merger of galaxies, and are detected at the time of their coalescence. Figure 15 shows that eLISA will observe signals coming from MBHCs in the mass range between $10^4 M_\odot$ and $10^7 M_\odot$, with typical binary mass ratios $0.1 < q < 1$, out to redshift $z \sim 20$ (if they already exist) corresponding to a luminosity distance of ~ 230 Gpc and an age of the universe of 180 Myr. Overlaid to constant signal-to-noise ratio contours are mass-redshift evolutionary pathways ending with the formation of a supermassive black hole representing (i) an

analogue of SgrA* (the black hole at our Galactic centre); (ii) a typical quasar at $z \approx 2$; and (iii) two distant quasars at $z \approx 6$. White dots mark merger events and highlight the fact that any massive black hole we observe in bright galaxies today has grown cutting through the eLISA sensitivity band. The forthcoming LISA-like observatory will therefore provide an highly complete census of MBHCs throughout the universe.

Expected rates - The expected rate of MBHCs is weakly constrained as it depends on the occupation fraction of (seed) black holes in haloes as a function of redshift, on their mass distribution (as depicted in Figure 12), on their accretion history, and on the pairing and hardening efficiency inside the new galaxy that has formed.^{85,89,103} Cosmological simulations of the galaxy assembly anchored to estimates of the local galaxy-merger-rate predict a few to few-hundred coalescences per year.⁹ Mergers are inevitable in a hierarchical universe, and whatever is the route to the massive black hole build-up, eLISA will provide a unique window to test MBHCs. MBHCs pinpoint places where galaxy mergers occur and in the eLISA band-width they inform us on the evolution of massive black holes in the low mass end of their distribution extending down to the desert zone.

Physics and astrophysics with precision gravitational wave measurements - In virtue of the extremely high signal-to-noise ratio of most of the events, MBHC parameters will be extracted with exquisite precision.⁹ Individual redshifted masses can be measured with an error of 0.1% – 1%, on both components. Even more interestingly, the spins of two massive black holes can be determined to an absolute uncertainty down to 0.01 in the best cases. This is a critical measurement, because the efficiency of accretion and mass growth of MBHs strongly depends on their spins which are currently difficult to determine through electromagnetic observations¹⁰⁴ (see §4.3).

The distinctive high signal-to-noise ratio of MBHCs will allow black hole "spectroscopy" i.e., the direct measure of several frequencies and damping times associated to the quasi-normal modes present in the ringdown signal of the newborn massive black hole.^{105,106} This will make it possible to carry on direct precision tests of the no-hair theorem. Violations of general relativity predictions may indicate new physics or the presence of exotic dark objects such as, e.g. boson stars that carry a surface.¹⁰⁷ The comparison between spectroscopy measurements from the LIGO-Virgo data on (BH*,BH*) coalescences and those from LISA¹⁰⁶ on MBHCs mapping the heaviest holes will be of enormous value: the proof of the universality of black holes over a mass range of more than six orders of magnitude.

Constraining the massive black hole cosmic history - While individual MBHC measurements will allow exquisite tests of general relativity and will probe several distinctive feature of massive black hole physics, information on the astrophysical evolution is encoded in the statistical properties of the observed population. As first illustrated in,¹⁰³ observations of multiple MBHCs can be combined together to learn about their formation and cosmic evolution. In particular the mass distribution of the ensemble of observed events encodes precious

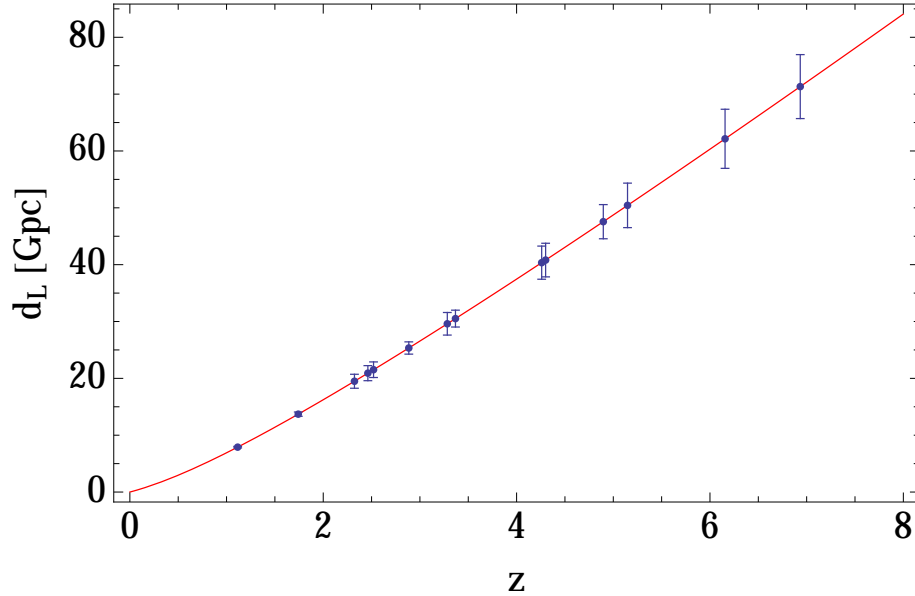


Figure 16: Simulated data points of "standard sirens" MBHCs in the luminosity distance versus redshift diagram.¹⁰⁸ Simultaneous electromagnetic counterparts to the MBHCs are assumed, which provide an independent measure of the redshift of the source. The data are from a simulated catalog of MBHCs extracted from a model of heavy seeds, and for a selected configuration of a LISA-like observatory. Note that a LISA-like mission will be able to map the expansion of the universe out to $z > 2$, which cannot be tested by Supernovae Type Ia or other current probes. Few standard sirens will be available at lower redshift, as MBHCs are rare events. See for details.¹⁰⁸ Courtesy of N. Tamanini.

information about the nature of the first seeds, whereas the spin distribution will constrain the primary mode of accretion that grows them to become supermassive.¹⁰⁴

Cosmography - Another peculiar property of MBHCs is that their luminosity distance can be directly measured as it is encoded in the gravitational wave signal, and its estimate does not involve cross-calibrations of successive distance indicators at different scales (as the distance ladder in the electromagnetic universe) since the gravitational wave luminosity of MBHCs is determined by gravitational physics, only. Thus MBHCs are standard sirens (we defer to §6.1 for an exact definition). A LISA like interferometer can provide the distance to the source to a stunning few percent accuracy. If an electromagnetic counterpart to the MBHC event can be observed,^{109,110} it will make it possible to reconstruct the luminosity distance versus redshift relation, as shown in Figure 16 offering the possibility of measuring the Hubble parameter at the level of 1 – 2%, and of

inferring bounds on the dark matter and dark energy content of the universe.¹⁰⁸

- **Extreme mass ratio inspirals** (EMRIs) describe the inspiral and possibly the plunge of stellar mass compact objects into a massive black hole at the centre of a galaxy.^{9,111} EMRIs still fall in the class of "binaries" despite their small mass ratio $q \ll 10^{-3}$.

EMRI flavours and expected rate - Massive black holes in galactic nuclei are surrounded by a swarm of stars and compact objects. The densities can be as high as 10^8 stars pc⁻³. In such extreme environments, stars are easily deflected on very low angular momentum orbits, owing to repeated, distant stellar encounters and thus can enter the massive black hole sphere of influence. The fate of main sequence stars on such "plunging" orbits is to be tidally disrupted.¹¹² But, compact objects such as neutron stars, stellar black holes and white dwarfs (for central black holes of $M_{\text{BH}} < 10^5 M_{\odot}$) can be captured in extremely eccentric orbits, with periastron of $\approx 10R_G$, avoiding disruption. Their orbit will then slowly circularise because of gravitational wave emission and the slow inspiral can in principle lead to observable EMRI signals. In general, stellar black holes are expected to dominate the observed rate for a LISA-like detector. This is because dynamical mass segregation tends to concentrate the heavier compact stars nearer the massive black hole,^{113–115} and because black hole EMRIs have higher signal-to-noise ratio, and so can be seen out to a much larger distance, typically of few Gpc ($z \simeq 1$). Their expected rate is uncertain due to the currently poor knowledge on the low mass end of the massive black hole mass function in galaxies (at $M_{\text{BH}} < 10^6 M_{\odot}$) and to the large uncertainties on the properties of typical compact object distributions in galactic nuclei. In general, a Milky Way type massive black hole is expected to form an EMRI every 10 Myr, implying a detection rate for a LISA-like mission in the figure of hundreds per year.^{9,116,117} There is, however, at least a factor of 100 uncertainty on this number.

Astrophysics and fundamental physics with EMRIs - High rates imply large astrophysical payouts following detection. The number and mass distribution of EMRIs will inform us about the unconstrained low end of the mass function of massive black holes and on the dynamics of compact objects in the dense environment of galactic nuclei on scales that are impossible to probe otherwise. The requirement of matching hundreds of thousands of cycles to dig out the signal from the data stream, implies that detections will automatically come with exquisite parameter estimation.⁹ Figure 17 shows that the mass of the two black holes and the spin of the massive black hole can be determined generally to better than a part in ten thousand, a precision that is unprecedented in astronomical measurements. This will make it possible to perform massive black hole population studies on a sample of relatively low redshift, quiescent black holes, complementary to the higher redshift, merging systems seen as MBHCs. EMRIs ensure that the inspiralling object essentially acts as a test particle in the background space-time of the central massive black hole. As such, the hundreds of thousands of wave cycles collected at the detector encode a very precise mapping of the stationary spacetime metric of the central massive

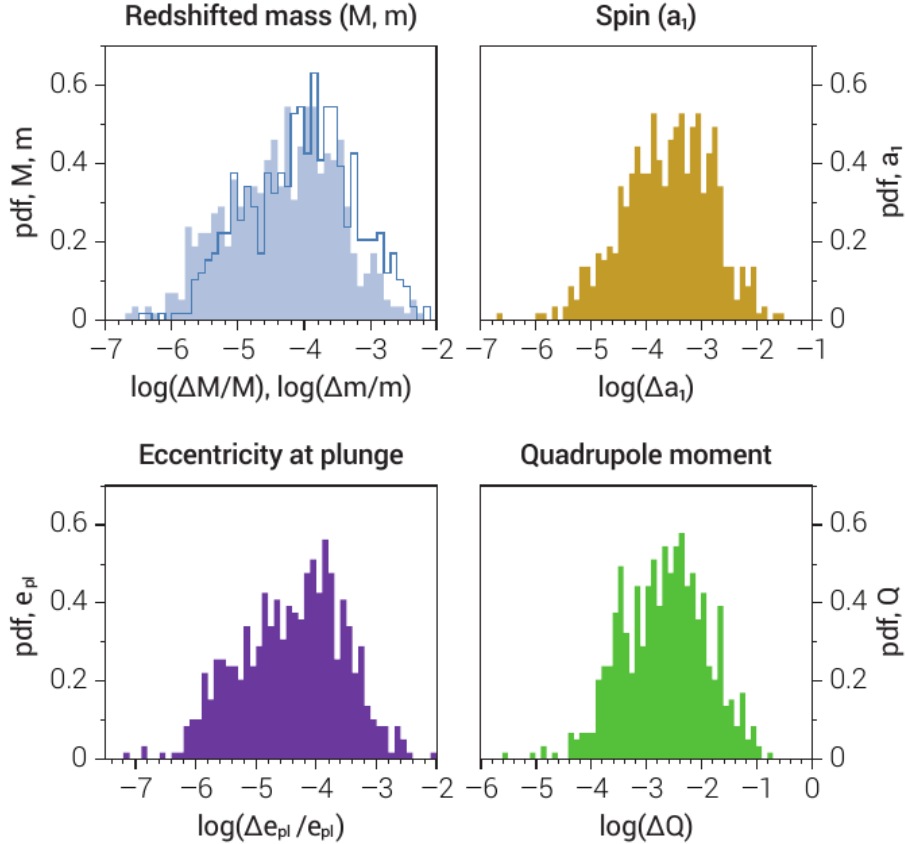


Figure 17: Parameter estimation accuracy on a sample of EMRIs from eLISA.¹⁰² In the top left panel the filled (empty) histograms are the distribution of mass determination precision for the central primary black hole (inspiralling compact object); the top right panel represents the distribution in the error determination of the spin magnitude of the central massive hole; the lower left panel represents the eccentricity error of the compact orbit at plunge; the lower right panel is the fractional precision at which the quadrupole moment of the primary black hole can be measured.

black hole, providing the ultimate test of its Kerr nature, complementary to the ringdown one possible with MBHCs.¹⁰⁵ As shown in Figure 17 deviations as small as 0.1% from the Kerr mass-quadrupole moment will be detectable for typical EMRIs, pushing testing of spacetime metric to a whole new level.

- **Continuous sources** comprise double white dwarfs in binaries (WD,WD), and possibly (NS,NS) and (BH*,BH*), in the Milky Way emitting a nearly monochromatic signal, preferentially located at the low frequency end of the

eLISA sensitivity interval.⁹ A number of (WD,WD) binaries are already known to emit a nearly monochromatic signal in the eLISA band since they have been discovered in the electromagnetic window, and are known as *verification binaries*. The discovery of new (up to a few thousand for a two-year mission) ultra-compact binaries with orbital periods below one hour and typically 5 to 10 minutes, determined from the periodicity of the gravitational wave, is one of the main objectives of a LISA-like mission. For a number of systems it is possible to measure the first time derivative of the frequency, and thus determine a combination of the masses of the two component stars that can be used to distinguish white dwarf, neutron star and black hole binaries. This will give precious insight on the distribution of the binaries in their different arrangements and flavours, present in the thin and thick discs of our Galaxy as well as in the halo and inside globular clusters. The highest signal-to-noise-ratio systems will allow us to study the complex physics of white dwarf interactions in binaries and to establish how systems survive as interacting binaries. We recall that (WD,WD) binaries are considered to be potential progenitors of Type Ia supernovae.^{9,118}

- **Galactic foreground** describes the signal coming from an unresolved population of million compact binaries emitting each a nearly monochromatic gravitational wave, which are confined in the thick disc of the Milky Way, preferentially (WD,WD) binaries which create a confusion-limited noise at frequencies below a few mHz, as illustrated in Figure 18. Its average level is comparable to the instrument noise, but due to its strong modulation during the year (by more than a factor of two) it can be detected. The overall strength can be used to learn about the distribution of the sources in the Milky Way.

- **Cosmological background** refers to the signal(s) coming from the primordial universe. The frequency band of a LISA-like detector corresponds to 0.1 to 100 TeV energy scales in the early universe, at which new physics is expected to become visible. We defer to¹¹⁹ for a authoritative description of the potential sources of the primordial universe.

5.3 The very low frequency gravitational universe

Moving further down in frequency, we enter the *very low frequency universe* probed by Pulsar Timing Array experiments EPTA,¹²⁰ PPTA,¹²¹ NANOGrav¹²² and the International PTA (IPTA),¹²³ which are especially sensitive in a window extending from 10^{-9} Hz to 10^{-7} Hz. Arrays of millisecond pulsars can be used to detect correlated signals such caused by passing gravitational waves. The dominant contribution at these frequencies is expected to come from supermassive black hole binaries (SMBHBs) in their slow inspiral phase, month or years prior to merging.¹²⁴

- **Background from supermassive black hole binaries** refers to the incoherent superposition of signals coming from a large number of SMBHBs of $10^8 - 10^{10} M_\odot$ forming in massive galaxy mergers out to redshift $z \lesssim 1$ which gives rise to a confusion-limited foreground, and on top of which particularly

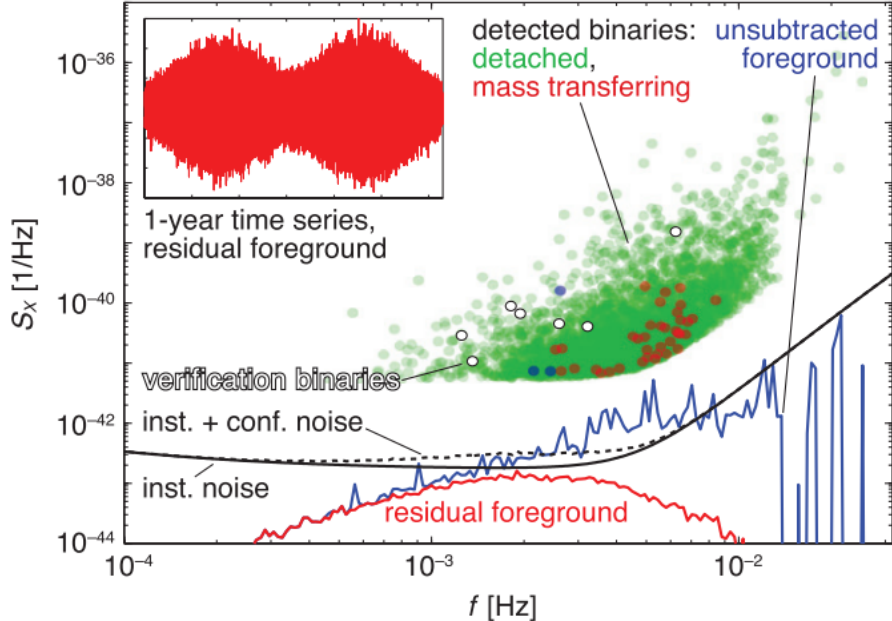


Figure 18: Power spectral density in units of strain Hz^{-1} of the gravitational wave foreground from galactic binaries, before (blue) and after (red) subtraction of resolvable systems, adapted from.¹¹⁸ Binaries are subtracted if they have a signal-to-noise ratio $\text{SNR} > 7$ over two years of observations, and are plotted as green (detached binaries) and red/blue (mass-transferring binaries) dots. White dots identify few known verification binaries. The solid (dashed) black curves represent instrument noise without (with) the residual foreground confusion noise included. The small inset to the top left represents a time series realisation of the residual foreground, showing the typical annual modulation due to the detector’s orbit around the Sun. Courtesy of M. Vallisneri.

bright or nearby sources might be individually resolved. The main traits of the background are described at the end of this Chapter, but we can anticipate the obvious payout of a PTA detection.

The background from SMBHBs informs us of the existence of a vast population of sub-pc (to be precise, sub-0.01pc) SMBHBs expected to rise according to the current cosmological model of galaxy assembly, and for which we have only indirect evidence.¹²⁵ Recently, a number of galaxies in the verge of merging has been discovered in large surveys, each galaxy harbouring an active supermassive black hole.¹²⁶ But, these mergers are in their early stage of pairing, as galaxies are observed interacting on scales of several kpc. The detection of this foreground can provide a measure of the efficiency of the pairing and hardening of these SMBHBs on pc and sub-pc scales. This will enable us to distinguish the

role of stellar and/or gas dynamics in removing energy and angular momentum from the binary (overcoming the last parsec problem, i.e. the possible stalling of the binary due its weak coupling with the environment.⁸⁵ In particular, from the shape and amplitude of the signal we will learn whether binaries are eccentric or circular in their approach to coalescence, possibly constraining the efficiency of the mutual coupling with stars or/and gas. Identification and sky localisation of individual sources, will also open the possibility of identifying their electromagnetic counterpart, making multi-messenger studies of SMBHBs possible. In §7.5 we describe in more detail the background detectable by PTA.

- **The unknown** is a universe hosting totally unexpected sources over the whole multi-frequency gravitational wave sky. History shows that every time a new window became accessible to electromagnetic observations we discovered sources that were never anticipated.

6 Binaries as key sources of the gravitational universe

In this section, we introduce shortly key concepts required to identify the main traits of binaries as astrophysical sources of gravitational waves, and defer to the book by M. Maggiore, *Gravitational Waves*, and Poisson and Will, *Gravity*,¹²⁷ for a comprehensive overview.

In Newtonian gravity, two point masses in a binary move on circular or elliptical orbits around the common centre of mass. The motion is periodic with constant Keplerian frequency $f_K = (GM/a^3)^{1/2}/(2\pi)$, where a is the semi-major axis of the relative orbit and $M = m_1 + m_2$ the total mass of the binary of components m_1 and m_2 , respectively. In general relativity, binary systems emit gravitational waves which radiate away orbital energy and angular momentum. In the case of circular binaries the gravitational wave, which tracks the large scale motion, is monochromatic with frequency f equal to $f = 2f_K$. To compensate the radiative energy losses, binaries back-react gradually hardening, i.e. decreasing their semi-major axis a and increasing the orbital frequency f_K . The emission is weak initially and a phase of nearly *adiabatic contraction*, lasting hundred to thousand million years, anticipates the phase of *inspiral, merger and ringdown*, which produce a detectable signal.

The *inspiral* refers to the phase when the two binary components can still be considered as structureless and their dynamics (both conservative and dissipative) can be described by Post Newtonian (PN) theory. In this phase, which is the longer lasting, the signal, called *chirp*, has a characteristic shape, with both the amplitude and frequency of the wave slowly sweeping to higher values. This phase is crucial in obtaining first estimates of the binary system's parameters most of which can be extracted by matching the observed signal on general relativity predictions. When the binary companions are spinning, the signal is modulated by spin-orbit and spin-spin couplings, and this modulation encodes in addition to the masses, orbit inclination, distance and sky location, also the

spins of the two interacting bodies.

The *merger* refers to the phase of "very late inspiral" and coalescence (no longer described within the PN formalism). Moving at around one third of the speed of light, the two bodies experience extreme gravitational fields so that their dynamics and signal can be described only in the realm of Numerical Relativity (NR). The merger signal lasts for a shorter time (milliseconds for stellar origin black holes, minutes for massive black holes) compared to the inspiral, and in this phase finite-size effects become important for neutron star mergers, as the stars carry a surface. NR simulations which account for the full non-linear structure of the Einstein's equation are highly successful in tracing the dynamics and the gravitational wave radiation.

The *ringdown* refers to the phase when the coalescence end-product relaxes to a new stationary equilibrium solution of the Einstein field equations: a new black hole for (BH*,BH*) and (NS,BH*) mergers or a hot hyper-massive or supra-massive neutron star or a black hole for the case of (NS,NS) mergers. Likewise MBHCs and EMRIs end with the formation of a new black hole. The emitted radiation can be computed using Perturbation Theory and it consists of a superposition of quasi-normal modes of the compact object that forms. These modes carry a unique signature that depend only on the mass and spin in the case of black holes.^{105,106}

The merger and ringdown parts of the signal last for a short duration, yet they carry tremendous luminosity. Their inclusion in a matched filter search for binary systems dramatically increases the distance reach and the accuracy at which the masses and spins can be measured. The access to the latest stages gives precious insight into the structure of neutron stars and the EoS at supra-nuclear densities; and in the case of black holes the possibility of testing gravity in the genuinely strong-field dynamical sector, and possibly prove the "no-hair" conjecture.^{105,128} The emission of gravitational waves from a binary is a continuous process and phenomenological models for the merger dynamics have been developed, the most remarkable among the various approaches being the Effective One Body (EOB) theory and the Phenom models which permits a continuous description of the three phases, as predicted by general relativity,^{129–132} including also tidal effects in the case of (NS,NS) coalescences.¹³³

6.1 Description of the inspiral

Binaries are irreversibly driven to coalescence, and the reference frequency of the gravitational wave at the time of coalescence is

$$f_{\text{coal}} = \frac{1}{(\pi 6^{3/2})} \frac{c^3}{GM} \quad (8)$$

representing twice the Keplerian frequency of a test mass orbiting around a non-spinning binary black hole of mass M (seen as single unit) at the innermost stable circular orbit R_{isco} . Neutron stars are so compact that their equilibrium radii are smaller than R_{isco} for many EoSs and typical masses,¹⁹ so that f_{coal} represents a reference frequency for coalescing compact objects in general.

- Radiated energy and angular momentum - back reaction

In the inspiral phase and to leading order, the power radiated by a *circular binary* (averaged over a orbital period) is

$$\dot{E}_{\text{gw}}^{\text{circ}} = \frac{32}{5} \frac{c^5}{G} \left(\frac{GM_c}{c^3} \pi f \right)^{10/3} = \frac{32}{5 \cdot 6^5} \frac{c^5}{G} \nu^2 \tilde{f}^{10/3} \quad (9)$$

where $f = 2f_K$ is the frequency of the gravitational wave emitted, $\tilde{f} = f/f_{\text{coal}}$ the unitless frequency, and

$$M_c \equiv \frac{(m_1 m_2)^{3/5}}{(m_1 + m_2)^{1/5}} = \nu^{3/5} M = \mu^{3/5} M^{2/5} \quad (10)$$

is the so called *chirp mass* expressed either in terms of the *symmetric mass ratio*, $\nu = m_1 m_2 / M^2$ (equal to 1/4 for an equal mass binary), or of the reduced mass $\mu = m_1 m_2 / M = \nu M$. The luminosity $\dot{E}_{\text{gw}}^{\text{circ}}$ near coalescence ($\tilde{f} \sim 1$) does not depend upon the mass M of the coalescing objects, but on the symmetric mass ratio ν only, approaching the value $\nu^2 (c^5/G) \sim \nu^2 (3.6 \times 10^{59}) \text{ erg s}^{-1}$. The independence on M is just a consequence of the fact that [energy/time] is equivalent to [mass/time], and time is equivalent to mass in $G = c = 1$ units. For a short time lapse, this huge gravitational wave luminosity is far in excess of the electromagnetic luminosity of the entire universe (when $\nu > 0.01$).

We then remark that merging black holes of stellar origin of $10 M_\odot - 30 M_\odot$ emit the same luminosity as merging black holes of $10^6 M_\odot$ or $10^9 M_\odot$, for a given ν , as the two fundamental constants c and G fix the scale uniquely.

The orbital angular momentum \mathbf{L} from a binary is radiated away at a orbit-averaged rate

$$\dot{L}_{\text{gw}}^{\text{circ,orb}} = \frac{32}{5} M_c c^2 \left(\frac{GM_c}{c^3} \pi f \right)^{7/3} = \frac{32}{5\sqrt{6^7}} \nu^2 M c^2 \tilde{f}^{7/3}, \quad (11)$$

in the direction of \mathbf{L} . When the binary nears coalescence, $\dot{L}_{\text{gw}}^{\text{circ,orb}} \rightarrow [32/5\sqrt{6^7}] \nu^2 M c^2$ whose value depends on M and ν .

Binaries with non zero eccentricity e and equal semi-major axis a , lose energy and angular momentum at a higher rate, as during closest approach when the mutual interaction is strongest, radiation is emitted more effectively. The two rates are enhanced by a factor $\mathcal{E}(e) = (1 + 73e^2/24 + 37e^4/96)/(1 - e^2)^{7/2}$ in (9), and $\mathcal{L}(e) = (1 + 7e^2/8)/(1 - e^2)^2$ in (11), with respect to a circular binary. In the case of eccentric binaries, the signal carries a dependence on the eccentricity e , and the emission spectrum is far richer than for a circular binary as more harmonics nf of the fundamental frequency $f = 2f_K$ enter the expression, with $n > 1$.

The emission of gravitational waves costs energy, and the source of radiation is the orbital energy of the binary, given by $E_{\text{bin}} = -(1/2)G\nu M^2/a = -(1/2)\nu M^2(GM)^{1/3}(\pi f)^{2/3}$ according to the virial theorem (computed to lowest order assuming Newtonian dynamics). Likewise, angular momentum is radiated away at the expense of the orbital angular momentum $\mathbf{L} = \nu M[GMa(1 - e^2)]^{1/2} \hat{\mathbf{L}}$, where $\hat{\mathbf{L}}$ denotes its direction.

The inspiral can be represented as a sequence of quasi-closed orbits where both the semi-major axis a and eccentricity e vary with time. During adiabatic contraction, and according to (9) and (11), one can prove that energy is extracted more rapidly than angular momentum, and binaries become more and more circular so that only little or null eccentricity is left at the time of coalescence. (Notice however that this is not necessarily true for EMRIs as in their inspiral they can retain significant eccentricity up to the innermost circular orbit.)

The total energy of the binary decreases adiabatically at a rate equal to $\dot{E}_{\text{bin}} = -\dot{E}_{\text{gw}}$. The binary hardens, the semi-major axis decreases, and the gravitational wave frequency increases at a rate

$$\dot{f} = \frac{96}{5} \pi^{8/3} \left(\frac{GM_c}{c^3} \right)^{5/3} f^{11/3}. \quad (12)$$

Equation (12) is derived setting $\dot{E}_{\text{bin}} = (dE_{\text{bin}}/df)(df/dt)$ with dE_{bin}/df inferred using the expression of the binary's Newtonian energy E_{bin} given few lines above. Equation (12) shows that to leading order the frequency evolution of the gravitational wave emitted by a circular binary is determined uniquely by the chirp mass M_c . The evolution of f is slow initially and it progresses faster and faster with time, given the rapid dependence of \dot{f} on the frequency itself. The solution to (12)

$$f(t) = \frac{5^{3/8}}{(256)^{3/8} \pi} \left(\frac{GM_c}{c^3} \right)^{-5/8} (t_{\text{coal}} - t)^{-3/8} \quad (13)$$

describes the rise in the frequency f of the gravitational wave emitted by the binary when chirping, where t_{coal} gives the epoch of merger. At t_{coal} , the frequency of the wave formally diverges, but a non diverging cut-off frequency is found when the system evolves into the relativistic state and the two masses merge.

Figure 1 of §2 shows (bottom row) the spectacular *chirp* observed in GW150914,² i.e. the increase in frequency during binary inspiral, and the convergence of a finite value at merger as a new black hole has formed.

According to (13), a binary observed at a frequency f takes a time to coalesce equal to

$$\tau_{\text{coal}}^{\text{circ}}(f) = \frac{5}{256\pi^{8/3}} \frac{1}{\nu} \left(\frac{c^3}{GM} \right)^{5/3} \frac{1}{f^{8/3}} \simeq \frac{7.4}{\nu} \left(\frac{M_\odot}{M} \right)^{5/3} \left(\frac{1 \text{ Hz}}{f} \right)^{8/3} \text{ days}, \quad (14)$$

which is a steep function of the frequency f .

The late inspiral, merger and ringdown phases have a very short duration. In terms of the dimensionless frequency $\tilde{f} \sim 1$ this time is

$$\tau_{\text{coal}}^{\text{circ}}(\tilde{f}) = \frac{6480}{256} \frac{1}{\nu} \frac{GM}{c^3} \frac{1}{\tilde{f}^{8/3}} \simeq 1.25 \times 10^{-4} \frac{1}{\nu} \frac{M}{M_\odot} \frac{1}{\tilde{f}^{8/3}} \text{ sec.} \quad (15)$$

Equation (15) shows that inspiraling massive binaries weighing more than $10^6 M_\odot$ are characterised by a longer duration signal than stellar origin binaries and that unequal mass binaries with same M take much longer to coalesce as $\tau_{\text{coal}}^{\text{circ}} \propto \nu^{-1}$.

To become observable sources of gravitational waves, binaries need to contract and merge on a timescale less than the Hubble time of 13.6 Gyr. Since one can relate f to the Keplerian period, equation (14) gives the characteristic time to coalescence of a generic binary as a function of the binary separation. Thus, the typical semi-major axis that a binary should have in order to coalesce within \sim Gyr is

$$a_{\text{gw}} \simeq 2 \times 10^{11} \left(\frac{1}{\nu} \right)^{1/4} \left(\frac{M}{M_\odot} \right)^{3/4} \left(\frac{\tau_{\text{coal}}^{\text{circ}}}{\text{Gyr}} \right)^{1/4} \text{cm}, \quad (16)$$

corresponding to a few R_\odot for stellar origin binaries, and to a 10^{-3} pc for black hole binaries of $10^6 M_\odot$. These are remarkably small distances, so that torques and dissipation processes of different origin need to be at work to "deposit" a binary in the domain of gravitational wave emission.

Two further important quantities which describe circular binaries in their spiral-in phase are the energy spectrum dE_{gw}/df and the total energy radiated in gravitational waves E_{gw} . In the quadrupole approximation,

$$\frac{dE_{\text{gw}}}{df} = \frac{\pi^{2/3}}{3G} (GM_c)^{5/3} f^{-1/3} \quad (17)$$

and

$$E_{\text{gw}} \sim \frac{\pi^{2/3}}{2G} (GM_c)^{5/3} f_{\text{max}}^{2/3} \quad (18)$$

where f_{max} is the maximum frequency at which the inspiral is observed. If we extrapolate crudely (18) up to f_{coal} , the radiated energy $E_{\text{gw}} \sim 0.08 \nu M c^2$ depends on the reduced mass of the binary (a more accurate estimate of E_{gw} is given ahead in this Chapter).

• Waveforms

Interferometers detect not the energy carried by the wave but the perturbation of spacetime itself, $h_{\mu\nu}$. Chapter 1 provided the formalism to compute, to leading order, the two independent (traceless) polarisation states h_+ and h_\times of a gravitational wave. For a circular binary at distance r the two states read

$$h_+(t) = \frac{4}{r} \left(\frac{GM_c}{c^2} \right)^{5/3} \left(\frac{\pi f(t_{\text{ret}})}{c} \right)^{2/3} \frac{1 + \cos^2(\iota)}{2} \cos[\Phi_N(t_{\text{ret}})] \quad (19)$$

$$h_\times(t) = \frac{4}{r} \left(\frac{GM_c}{c^2} \right)^{5/3} \left(\frac{\pi f(t_{\text{ret}})}{c} \right)^{2/3} \cos(\iota) \sin[\Phi_N(t_{\text{ret}})] \quad (20)$$

where $\iota = \hat{\mathbf{n}} \cdot \hat{\mathbf{L}}$ is the inclination angle between the line of sight $\hat{\mathbf{n}}$ and the unit vector parallel to the orbital angular momentum \mathbf{L} of the binary. $f(t_{\text{ret}})$ is the instantaneous frequency given by (13) (evaluated at the retarded time

$t_{\text{ret}} = t - r/c$) and $\Phi_N \equiv 2\pi \int f(t')dt'$ is the lowest order contribution to the orbital phase evolving according to

$$\Phi_N(t) = \Phi_0 - 2 \left(\frac{5GM_c}{c^3} \right)^{-5/8} (t_{\text{coal}} - t)^{5/8}, \quad (21)$$

where Φ_0 is a constant giving the orbital phase at the epoch of merger, when f diverges nominally (finite size effect will impact on the waveform before this divergence is reached). It is worth noting that, at any given frequency, both h_+ and h_\times scale as $\nu M^{5/3}$, i.e. faster than linear with respect to the total mass M and linear in ν , so that unequal mass binaries of total mass M have weaker emission.

Note further that the ratio of the two polarisation amplitudes h_+/h_\times depends on the inclination angle ι . When the binary is seen edge-on, i.e. $\iota = \pi/2$, $h_\times = 0$ and radiation has pure + polarisation as, from the observer's view, the motion of the binary stars projected on the sky is purely linear. When $\iota = 0$, so that the binary is seen face-on, the stars execute a circular motion in the sky, and both polarisation components have equal amplitude and are out of phase by $\pi/2$, emitting a circularly polarised wave. Thus, to leading order, the polarisation has a direct relationship to the motions of the point masses projected on the observers sky plane.

A single detector can only measure a linear combination of the polarisations, called *strain amplitude*,

$$h(t) = F_+(\alpha, \delta, \psi)h_+ + F_\times(\alpha, \delta, \psi)h_\times \quad (22)$$

where F_+ and F_\times are the antenna patterns for a particular detector.⁷ The angles α and δ describe the binary's position on the sky, and ψ the component of $\hat{\mathbf{L}}$ orthogonal to $\hat{\mathbf{n}}$. The angles ι and ψ fully specify the orientation of the binary's angular momentum $\hat{\mathbf{L}}$. They are constants for transient sources, but they must be considered time-dependent for long lasting sources, when Doppler modulation of the signal due to the relative motion of the source and detector can not be neglected.

It is expedient to write the response $h(t) = F(t)(\cos \xi h_+ + \sin \xi h_\times)$ with $F = (F_+^2 + F_\times^2)^{1/2}$ and $\tan \xi = F_\times/F_+$. In this way $F(t)$ is independent of the polarisation angle and provides a measure of the sensitivity of the detector to different locations in the sky.

If the signal is extracted using *match filtering techniques*, what is measured is the effective strain amplitude defined as

$$h_{\text{eff}} = \mathcal{N}_{\text{cycles}}^{1/2} h, \quad (23)$$

where $\mathcal{N}_{\text{cycles}} = fT$ represents the number of cycles the chirping binary covers over the observing (or emitting) time T . The number of cycles spent by the source in the detector bandwidth Δ between $[f_{\min}, f_{\max}]$ is equal to $\mathcal{N}_{\text{cycles}} = \int_{f_{\min}}^{f_{\max}} df(f/\dot{f})$. From (12) we infer

$$\mathcal{N}_{\text{cycles}} = \frac{1}{32\pi^{8/3}} \left(\frac{GM_c}{c^3} \right)^{-5/3} (f_{\min}^{-5/3} - f_{\max}^{-5/3}). \quad (24)$$

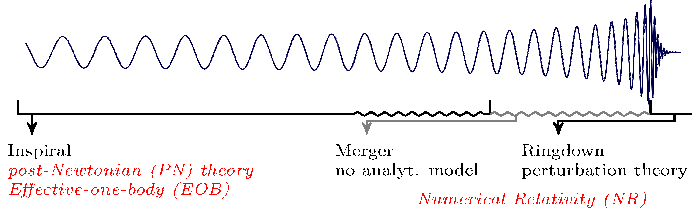


Figure 19: Characteristic waveform $h(t)$ from coalescing non spinning equal mass black holes, depicting the inspiral, merger and ringdown phases, from¹³⁴. Wavy lines illustrate the regime close to merger where analytical methods have to be bridged by NR. The different approximation schemes and their range of validity are indicated. Courtesy of F. Ohme.

Note that $\mathcal{N}_{\text{cycles}}$ can be written in a compact form in terms of the dimensionless frequency \tilde{f} and the in-band cycles can be estimated in terms of the minimum frequency of the detector sensitivity f_{\min} (since $f_{\min} \ll f_{\max}$)

$$\mathcal{N}_{\text{cycles}}(\tilde{f}_{\min}) = \frac{6^{5/2}}{32\pi} \frac{1}{\nu} \tilde{f}_{\min}^{-5/3}. \quad (25)$$

Note further that $\mathcal{N}_{\text{cycles}}$ is proportional to ν^{-1} so that unequal mass binaries and in particular EMRIs remain in band for a longer time covering many more cycles before plunging, which enhances the strength of their signal. Typically, merging binaries are tracked for $\mathcal{N}_{\text{cycles}} \sim O(10) - O(100)$, while EMRIs for $O(10^{4-5})$.

Match filtering techniques, can be very effective in extracting the signal from the noise, even when the typical amplitude is a factor $\mathcal{N}_{\text{cycles}}^{1/2}$ below the noise floor. Since the number of cycles spent in the interferometer bandwidth $\mathcal{N}_{\text{cycles}} \propto f^{-5/3}$ decreases with increasing frequency more rapidly than the rise of h with f , the effective strain amplitude $h_{\text{eff}} = \mathcal{N}_{\text{cycles}}^{1/2} h \propto f^{-1/6}$ decreases with f , even if the nominal instantaneous amplitude increases ($h \propto f^{2/3}$). Effective strain amplitudes from interesting astrophysical sources within reach have $h_{\text{eff}} \approx 10^{-18} - 10^{-22}$.

To have a description of the *late inspiral* linearised theory is insufficient. As the two masses come closer, the relative orbital speed (v_{orb}/c) increases, and one should compute the orbit dynamics, amplitude and phase of the gravitational waves in the so called PN formalism,^{127,135} which consists in an expansion in terms of (v_{orb}/c) , accurate down to relative binary separations of the order of $a_{\text{NR}} \sim 10GM/c^2$. Below a_{NR} instead, Numerical Relativity (NR) gives the full and final description of the gravito-dynamics of the binary, from the late inspiral, final plunge and merger. The Effective One Body^{129,134,136} method and the Phenom models^{131,132} prove to be very effective in providing waveforms consistent with NR, across the three phases. This allows to create template repositories that are used to model the observed signal, and extract the pa-

parameters at the source. Figure 19 illustrates in a rather simple way, the main features of the waveform from a non spinning, equal mass black hole binary. The key feature of black hole coalescence is that after merger the amplitude decays almost suddenly indicating the formation of a new event horizon.

- Binaries at cosmological distances in the PN frame work

Coalescing binaries can be seen out to cosmological distances, and in this case the expansion of the universe during the propagation of the wave from the source to the detector can not be neglected. This requires a re-exam of (19) and (20). It is easy to show that the frequency, mass and distance are affected by the underlying expansion of the universe in a rather simple way. If z is the cosmological redshift of the source of gravitational waves, the frequency, mass and distance acquire the following corrections:

- the observed frequency f_{obs} is redshifted with respect to the frequency as measured in the source frame, $f_{\text{obs}} = f/(1+z)$;
- the chirp mass in the source frame M_c is replaced by the redshifted chirp mass $\mathcal{M}_c = (1+z)M_c$, i.e. the chirp mass in the observer-frame;
- the source distance r is replaced by the luminosity distance $d_L(z) = (1+z)a(t_0)r$, where $a(t_0)$ is the scale factor today.

According to the above scalings, the evolution of the waveform of a generic binary is invariant under the change of $M_c \rightarrow (1+z)M_c$ and $f \rightarrow f/(1+z)$, so that the wave does not encode any information on the cosmological redshift of the source, and the two polarisation amplitudes are given by

$$h_+(\tau^{\text{obs}}) = \frac{4}{d_L(z)} \left(\frac{G\mathcal{M}_c(z)}{c^2} \right)^{5/3} \left(\frac{\pi f_{\text{obs}}(\tau^{\text{obs}})}{c} \right)^{2/3} \frac{1 + \cos^2(\iota)}{2} \cos[\Phi(\tau^{\text{obs}})] \quad (26)$$

$$h_\times(\tau^{\text{obs}}) = \frac{4}{d_L(z)} \left(\frac{G\mathcal{M}_c(z)}{c^2} \right)^{5/3} \left(\frac{\pi f_{\text{obs}}(\tau^{\text{obs}})}{c} \right)^{2/3} \cos(\iota) \cos[\Phi(\tau^{\text{obs}})] \quad (27)$$

where $\tau^{\text{obs}} = (1+z)(t_{\text{coal}} - t)$ is the time to coalescence measured by the observer's clock (note that $\tau_{\text{ret}}^{\text{obs}} = \tau^{\text{obs}}$), and where the frequency and orbital phase $\Phi = \pi \int f_{\text{obs}}(t') dt'$ are computed solving for the equation

$$\dot{f}_{\text{obs}} = \frac{96}{5} \pi^{3/8} \mathcal{M}_c^{5/3}(z) f_{\text{obs}}^{11/3} [1 + \mathcal{D}^{\text{PN}}] \quad (28)$$

where \mathcal{D}^{PN} is the PN correction to the phase, up to the desired order. \mathcal{D}^{PN} depends on t_{coal} and Φ_0 , and can be expanded analytically in powers of the symmetric mass ratio ν and of $\mathcal{M}_c(z)f_{\text{obs}}$, both independent of redshift z (we defer to¹³⁵ for the full analytical expression of \mathcal{D}^{PN} up to 3.5 PN order). Again \dot{f}_{obs} is dominantly determined by the chirp mass, but PN corrections \mathcal{D}^{PN} depend on the symmetric mass ratio and on the two black hole spins (if different than zero). Therefore, these corrections help in breaking degeneracies in the

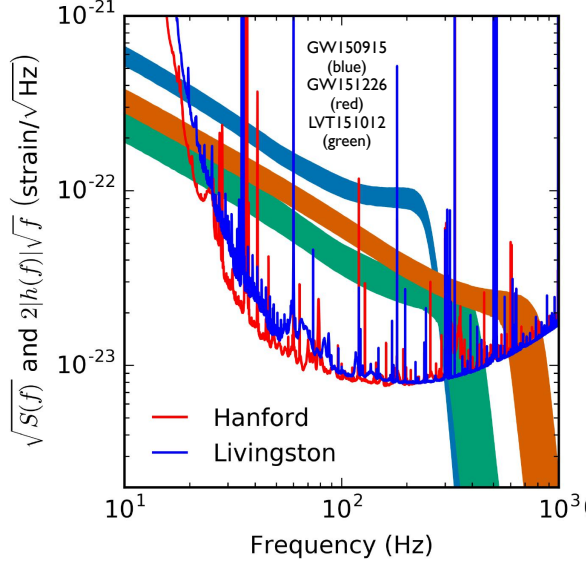


Figure 20: The figure shows the spectral strain sensitivity of the total noise $\sqrt{S_{\text{noise}}}$ of the Hanford and Livingston detectors and the signals of GW150914, GW151226 and of the trigger event LVT151012 (which has a 87% probability of hosting a third coalescing black hole binary) plotted as a function of frequency (in Hz). The figure is adapted from.³⁸ Courtesy of the LIGO Scientific Collaboration and Virgo Collaboration.

waveforms and allow to measure individual black hole (redshifted) masses and spins.

- Fourier domain

In order to compare theoretical waveforms with experimental sensitivities, and to compute the signal-to-noise ratio it is necessary to describe the signal in the frequency domain. The Fourier transform of the two polarisation states of the wave are given by:

$$\tilde{h}_+(f) = A \frac{c}{d_L} \left(\frac{G \mathcal{M}_c}{c^3} \right)^{5/6} e^{i\Phi_+^{\text{PN}}(f)} \frac{1}{f^{7/6}} \left(\frac{1 + \cos^2 \iota}{2} \right) \quad (29)$$

$$\tilde{h}_\times(f) = A \frac{c}{d_L} \left(\frac{G \mathcal{M}_c}{c^3} \right)^{5/6} e^{i\Phi_\times^{\text{PN}}(f)} \frac{1}{f^{7/6}} \cos \iota \quad (30)$$

with $A = \pi^{-2/3} (5/12)^{1/2}$. The phases $\Phi_+^{\text{PN}}(f) = \Phi_\times^{\text{PN}}(f) - \pi/2$ are as of today

computed up to the 4th PN order, and can be expressed again in terms of ν and of $\mathcal{M}_c(z)f$. One can then compute the Fourier transform of the strain amplitude $h(t)$ (eq. 22), denoted as $\tilde{h}(f)$ (in units of Hz^{-1}) which includes the antenna pattern response of the detector, and calculate the square of the signal-to-noise ratio S/N (or SNR) of a source as

$$\left(\frac{S}{N}\right)^2 = \int_0^\infty d\ln f \frac{|2\tilde{h}(f)\sqrt{f}|^2}{S_{\text{noise}}} \quad (31)$$

where $\sqrt{S_{\text{noise}}}$ is the *spectral strain sensitivity* or *spectral amplitude* with dimension $\text{Hz}^{-1/2}$, and describes the noise in the detector. Customarily, $\sqrt{S_{\text{noise}}}$ and $2\tilde{h}(f)\sqrt{f}$ are plotted in the same diagram as function of frequency f , to describe the sensitivity window of an interferometric experiment jointly with the strength of the source signal. The signal from a coalescing binary sweeps through the frequency domain as illustrated in Figure 20, where for the first time we can plot the signals from the three "real" sources (GW150914 and GW151226 mentioned above, plus a third candidate signal LVT151012) detected in the Hanford and Livingston interferometers above the sensitivity curves.

- Chirping binaries as standard sirens

Chirping binaries are *standard sirens*, in that the measurement of their gravitational wave signal can determine the source absolute luminosity distance. This is the analogue of the *standard candles* of the electromagnetic universe, but differently from electromagnetic observations, where one has to resort to cross-calibration of multiple distance indicators, for the gravitational wave sources the only calibration is the assumption that general relativity describes the binary waveform. We notice that the luminosity distance is a direct observable, if one can measure *both* polarisations h_+ and h_\times separately as well as \dot{f}_{obs} directly from the observations. On one side the ratio of the two polarisations h_+/h_\times gives the inclination angle ι as both carry the same dependence on the chirp mass, and by measuring the frequency derivative \dot{f}_{obs} imprinted in the phase of the chirping signal one can infer the chirp mass (and at higher PN orders the individual masses). Then, all parameters in the expressions of h_+ and h_\times are fixed except $d_L(z)$ which can be measured directly. This defines a standard siren. Once d_L is determined, one can then infer the redshift of the source, given a cosmological model. But the measure of d_L is slightly more complex.

A single detector can not measure h_+ and h_\times independently, as it measures a linear combination of the two polarisation states as indicated in (22). Measuring the amplitude of the wave gives a combination of the angles $(\alpha, \delta, \psi, \iota)$ and d_L , even when the redshifted chirp mass is known with sufficient precision. Although \mathcal{M}_c decouples from the amplitude, the luminosity distance, position, and orientation angles remain highly coupled and can be determined with overall fractional accuracy of 1/signal-to-noise. One measures an effective luminosity distance $d_{L,\text{eff}} = d_L/\mathcal{F}$ where $\mathcal{F} \equiv (F_+^2(1+\cos^2\iota)^2 + F_\times^2 \cos^2\iota)^{1/2}$. For non spinning binaries the signal is characterised by nine parameters: $M, \nu, t_{\text{coal}}, \Phi_0, \alpha, \delta, \psi, \iota, d_L$. When the phase is known to a high order PN, the masses M and ν , and the

constant Φ_0, t_{coal} can be determined. A network of three non-colocated interferometers can then measure three independent combinations of the polarisations and two time delays, and hence d_L . In absence of non colocated multiple detectors one can exploit the rotation of the interferometer around the Sun, as this is the case for a space born interferometer with the minimal number of links. With this procedure, the source position can be inferred to within a few/several square degrees in the best cases, giving information about the source's distance and inclination.¹³⁷ A way to reduce these degeneracies is to measure the event electromagnetically. An electromagnetic signature, should it exist, can pin point the event's position far more accurately than gravitational waves alone. In this circumstance, the position angles decouple and multiple detectors allow for a precise determination of the source distance.¹³⁷ The remarkable fact is that when used in concomitance with an independent measurement of the redshift of the source, standard siren observations provide information on the luminosity distance - redshift relationship, hence an independent test of the current cosmological paradigm.¹³⁸ This is shown in Figure 16 for the case of MBHCs.

6.2 Spin effects in black hole binary inspirals

The formalism and the results described so far considered inspiralling point particles characterised by their masses m_1 and m_2 , only. But astrophysical objects are endowed by rotation, and it is necessary to evaluate the role of their spins \mathbf{S}_1 and \mathbf{S}_2 in their dynamics.¹³⁵ Spins introduce spin-orbit and spin-spin couplings (i.e., the “dragging of inertial frames” by the bodies’ spins) affecting the binary dynamics, and consequently the phase and amplitude evolution of the gravitational signal during the inspiral, merger and ringdown. In general, misaligned spins cause the orbital angular momentum to precess, modulating the emitted gravitational wave. Spin misalignment increases the parameter space of templates needed to detect gravitational waves via matched filtering but also breaks degeneracies between estimated parameters in detected events.

Spin induced effects are important when the dimensionless spin parameter $s_{\text{spin}} \equiv c|\mathbf{S}|/Gm^2$ of one or of the two binary components is fairly large. This is the case for black holes which can be maximally spinning. (We recall that massive black holes in galaxies can attain high values of their spin due to accretion.) Neutron stars are unlikely to spin fast enough to drive interesting effects when they are in the detector band during the inspiral phase. To show this, consider the moment of inertia of a neutron star $I_{\text{NS}} = (2/5)k_I M_{\text{NS}} R_{\text{NS}}^2$, where $k_I \sim 0.7 - 1$ measures the extent to which the mass distribution inside the neutron star is centrally condensed compared to a uniform sphere. For a neutron star with $M_{\text{NS}} = 1.4 M_{\odot}$, radius $R_{\text{NS}} = 12$ km, and spin period P_{NS} of 10 ms, as observed in double neutron star binaries, the Kerr parameter

$$s_{\text{spin}}^{\text{NS}} = \frac{c}{G} \frac{I_{\text{NS}}}{M_{\text{NS}}^2} \frac{2\pi}{P_{\text{NS}}} \quad (32)$$

is only $\sim 0.06 k_I$.

We focus here on spinning black holes only, and on precession effects on the binary orbital angular momentum and spins. There are astrophysical mechanisms^{63,64} that tend to align the black hole spins with the orbital angular momentum during the early phases of binary evolution in gaseous circum-binary discs,^{139–141} but the alignment may be partial or may depend on the environment, so that spin-induced precession effects are astrophysically important during the inspiral and merger of the two black holes.^{142–144}

If gravitational wave losses can be neglected, the total angular momentum \mathbf{J} of the binary, defined as $\mathbf{J} = \mathbf{S}_1 + \mathbf{S}_2 + \mathbf{L}$, is conserved together with the modulus of \mathbf{L} and the moduli of the two spins $s_{\text{spin},1}$ and $s_{\text{spin},2}$. Under these conditions the PN equations are invariant under a re-scaling of the total mass M , leaving as free parameter only the symmetric mass ratio ν , or equivalently $q = m_2/m_1 < 1$.

For a circular binary, to 2PN order in the spins, the evolution equations read^{142,143}

$$\dot{\mathbf{S}}_1 = \boldsymbol{\Omega}_1 \times \mathbf{S}_1, \quad \dot{\mathbf{S}}_2 = \boldsymbol{\Omega}_2 \times \mathbf{S}_2, \quad (33)$$

where

$$\boldsymbol{\Omega}_1 = \frac{G}{c^2 a^3} \left(2 + \frac{3}{2} q - \frac{3(\mathbf{S}_2 + q\mathbf{S}_1) \cdot \mathbf{L}}{2L^2} \right) \mathbf{L} + \mathbf{S}_2 \quad (34)$$

$$\boldsymbol{\Omega}_2 = \frac{G}{c^2 a^3} \left(2 + \frac{3}{2} q - \frac{3(\mathbf{S}_1 + q^{-1}\mathbf{S}_2) \cdot \mathbf{L}}{2L^2} \right) \mathbf{L} + \mathbf{S}_1 \quad (35)$$

are the spin precession frequencies averaged over the orbital period, and $\mathbf{L} = \nu M(GMa)^{1/2} \hat{\mathbf{L}}$ the Newtonian angular momentum vector (with $\hat{\mathbf{L}}$ the unit vector indicating the direction). Equations (33,34,35) imply that the direction of $\hat{\mathbf{L}}$ precesses according to

$$\dot{\hat{\mathbf{L}}} = - \left(\nu M(GM)^{2/3}/(\pi f)^{1/3} \right)^{-1} (\dot{\mathbf{S}}_1 + \dot{\mathbf{S}}_2). \quad (36)$$

Equation (36) neglects the loss of orbital angular momentum by gravitational radiation and this is correct as long as the precession timescale

$$\tau_{\text{prec}} \equiv 2\pi\Omega^{-1} \approx \frac{2\pi c^2 a^{5/2}}{G^{3/2} \nu M^{3/2}} \quad (37)$$

is shorter than the timescale for gravitational wave emission $\tau_{\text{coal}}^{\text{circ}}$, that can be written in terms of the binary separation a as

$$\tau_{\text{coal}}^{\text{circ}} = \frac{5}{256} \frac{c^5}{G^3} \frac{a^4}{\nu M^3}. \quad (38)$$

Equations (33,34,35) and (36) imply that highly spinning black holes can change their spin orientation prior to merging. (Interestingly, it has been shown that the spin of a black hole may totally flip direction along the orbital angular momentum during the latest inspiral phase.¹⁴⁵)

A close inspection of the above equations^{142,143,146} reveals the existence of subset configurations where all the three vectors are locked in a plane as they

jointly precess around \mathbf{J} at the same rate. These configurations are often referred to as "spin-orbit resonances" and are a consequence of the hierarchy in the three timescales, the orbital time $\tau_{\text{orb}} = 2\pi f_K^{-1} \ll \tau_{\text{prec}} \ll \tau_{\text{coal}}^{\text{circ}}$. When the loss of energy and orbital angular momentum through radiation reaction are included, systems can eventually be captured into these resonance orientations,¹⁴² thus reducing the range of precession frequencies.

Studies by¹⁴³ further indicate that spin distributions that are initially partially aligned with the orbital angular momentum can be distorted during the PN inspiral. Spin precession tends to align (antialign) the binary black hole spins with each other if the spin of the more massive black hole is initially partially aligned (antialigned) with the orbital angular momentum, thus increasing (decreasing) the average final spin. Spin precession is stronger for comparable-mass binaries and could produce significant spin alignment before merger for both supermassive and stellar origin black hole binaries.¹⁴³ But in the case of quasi-circular binaries there are solutions which are unstable to large misalignments when the spin of the higher-mass black hole is aligned with the orbital angular momentum and the spin of the lower-mass black hole is antialigned. This can occur in the strong field regime, near the merger.¹⁴⁴ It is therefore clear that the re-orientation of spins during the end of the inspiral and merger has important implication, and it affects the final spin of the new black hole and the extent of the gravitational recoil described in the next paragraph.

6.3 Gravitational recoil

Merging black hole binaries radiate net linear momentum and the newly formed black hole receives a *gravitational recoil*, acquired near the time of formation of the common horizon of the merging black holes. In the framework of NR, it is now possible to obtain precise estimates of $\mathbf{v}_{\text{recoil}}$ as a function of the black hole parameters.

Gravitational recoil emerges when the two black holes are not symmetric. The asymmetry can be due to unequal masses, unequal spins, or a combination of the two. A non spinning black hole binary radiates net linear momentum if the component masses are not equal, and the maximum recoil is of $\sim 175 \text{ km s}^{-1}$ when the mass ratio is $q \sim 0.195$.¹⁴⁷ The complementary case, when the black holes have equal masses but unequal spins, first reported in,¹⁴⁷ leads to a maximum possible in-plane recoil velocity of $\sim 460 \text{ km s}^{-1}$. This occurs when the spins have equal-amplitude, and are anti-parallel with respect to the orbital angular momentum direction. But generic binaries with in-plane spin components may lead to much higher recoil velocities. Numerical relativity experiments find that the recoil normal to the orbital plane (due to spin components lying in the orbital plane) can be larger than the in-plane recoil originating from either the unequal-masses or the spin components normal to the orbital plane. Recoil velocities of nearly 4000 km s^{-1} (known as super-kicks) arise when equal-mass maximally spinning black holes merge with spins in the orbital plane equal in magnitude and opposite in direction. But even larger recoil velocities, of up to $\sim 5000 \text{ km s}^{-1}$, emerge in "hang-up" binaries with equal-mass, equal-spin mag-

nitudes having both spins forming an angle of $\sim 50^\circ$ with the orbital angular momentum and in-plane components anti-aligned (see Fig. 1¹⁴⁸).

Independent recoil velocity calculations have confirmed these behaviours, and empirical formulae have been derived to match the numerical results. To illustrate the dependence of $\mathbf{v}_{\text{recoil}}$ on the spins and mass ratio we report a handy formula for the recoil, referring to¹⁴⁷ for details:

$$\mathbf{v}_{\text{recoil}}(\nu, \mathbf{S}_1, \mathbf{S}_2) = v_m \mathbf{e}_1 + v_{\perp} (\cos \xi \mathbf{e}_1 + \sin \xi \mathbf{e}_2) + v_{\parallel} \hat{\mathbf{L}} \quad (39)$$

where \perp and \parallel refer to components perpendicular and parallel to the orbital angular momentum unit vector $\hat{\mathbf{L}}$, ξ measures the angle between the unequal mass and spin contribution to the recoil velocity in the orbital plane,

$$v_m = A\nu^2 \frac{(1-q)}{(1+q)} [1 + B\nu] \quad (40)$$

is the in-plane component of the recoil velocity due to the asymmetry induced by the different masses carried by the black holes,

$$v_{\perp} = H \frac{\nu^2}{(1+q)} [(1+B_H\nu)(\mathbf{S}_2^{\parallel} - q\mathbf{S}_1^{\parallel}) + H_s \frac{(1-q)}{(1_q)^2} (\mathbf{S}_2^{\parallel} + q^2\mathbf{S}_1^{\parallel})] \quad (41)$$

the additional in-plane component of the recoil related to both asymmetries in the spin and mass, and finally

$$v_{\parallel} = K \frac{\nu^2}{(1+q)} [(1+B_K\nu)|\mathbf{S}_2^{\perp} - q\mathbf{S}_1^{\perp}| \cos \Theta_1 + K_s \frac{(1-q)}{(1_q)^2} |\mathbf{S}_2^{\parallel} + q^2\mathbf{S}_1^{\parallel}| \cos \Theta_2] \quad (42)$$

the recoil velocity parallel to $\hat{\mathbf{L}}$. It is useful to notice how the perpendicular (parallel) components of the recoil couple with the parallel (perpendicular) components of the spin vectors. In the above equations, B, B_H, B_K, H_s, K_s are dimensionless constants (see¹⁴⁷) derived from numerical relativity simulations, Θ_1 and Θ_2 are angles between the in-plane component of the total spin vector of the two black holes and the infall direction at merger, and \mathbf{e}_1 and \mathbf{e}_2 are unit vectors in the orbital plane and mutually orthogonal. The current best estimates for the dimensional constants are : $A = 1.2 \times 10^4 \text{ km s}^{-1}$, $H = (6.9 \pm 0.5) \times 10^3 \text{ km s}^{-1}$ and $K = (6.0 \pm 0.1) \times 10^4 \text{ km s}^{-1}$ and $\xi = 145^\circ$.

Recoil velocities have important implications in astrophysics, as the merger remnants may leave permanently or temporarily the sites inhabited by their progenitor binaries. For stellar origin coalescences, this occurs when v_{recoil} exceeds the escape speed from the parent star cluster, typically $\approx 50 \text{ km s}^{-1}$. For massive black holes in merging galaxies, the newly formed black hole leaves the galaxy if its recoil velocity exceeds $\approx 800 \text{ km s}^{-1}$. For lower velocities, the kicked massive black hole can return and sink back at the centre of the host, preserving a level of Brownian motion after having dissipated its kinetic energy via dynamical friction against stars or/and gas.¹⁴⁹ Off-set black holes can be seen in an active phase since they may drag gas with them which can be accreted. Off-set

AGN clearly pinpoint, albeit indirectly, places where a merger has occurred, and a number of candidates have been observed, in large AGN surveys.¹⁵⁰ Super-kicks naturally prompt the question of why supermassive black holes are often seen at the centres of their host galaxies. There are indications that super-kick configurations may not be the favourite arrangements as accretion torques tend to align the spins to the orbital angular momentum suppressing the in-plane components of the spins and reducing the extent of the recoil.^{139,140} But, hang-up configurations may lead to non-negligible probabilities of recoils of several 1000 km s^{-1} in real astrophysical sources. In general, spin-orbit resonances are likely to populate specific portions of the parameter space, and depending on which of the two black holes has more aligned spin with \mathbf{L} , kicks are either suppressed or enhanced. At present which of these scenarios is more common is observationally undetermined.

6.4 Modelling the final spin and mass of coalescing black holes

A black hole binary coalescence is an "elementary" process that takes as input two black holes of initial mass m_1 and m_2 and spin vectors \mathbf{S}_1 and \mathbf{S}_2 (with $\mathbf{S}_i = s_i G m_i^2 \hat{\mathbf{s}}_i / c$, and $i = 1, 2$), Newtonian energy E_{bin} and angular momentum L (the choice of $\hat{\mathbf{L}}$ is arbitrary and defines the z -axis) defined at a far-out initial separation a_{in} and produces a new black hole of mass M_{fin} , spin $\mathbf{S}_{\text{fin}} = s_{\text{fin}} G M_{\text{fin}}^2 \hat{\mathbf{s}}_{\text{fin}} / c$ and recoil speed $\mathbf{v}_{\text{recoil}}$. The full mapping between the initial and final states can be obtained by solving exactly the Einstein's field equations which incorporate the law of energy-momentum conservation. It is important to notice that a final state can correspond to different initial states, given that the ten initial internal degrees of freedom are mapped into the seven of the new black hole that forms.

Astrophysical black holes in binaries are expected to span a wide parameter space, too vast to be explored entirely. At a lower level one can construct a mapping between a minimal set of initial conditions involving the mass ratio ν and spin vectors \mathbf{S}_1 , \mathbf{S}_2 , and \mathbf{S}_{fin} . In this way one can capture some important properties of the end-states, once the directions of the spins relative to the orbital angular momentum at a "sufficiently" far-out distance are specified. This mapping is degenerate as different initial states can lead to the same final state, also in this lowered parameter space.^{146,151,152} The binary's unit vector $\hat{\mathbf{L}}$ fixes a direction in space and key angles are $\cos \theta_1 = \hat{\mathbf{s}}_1 \cdot \hat{\mathbf{L}}$, $\cos \theta_2 = \hat{\mathbf{s}}_2 \cdot \hat{\mathbf{L}}$, and $\cos \gamma \equiv \hat{\mathbf{s}}_1 \cdot \hat{\mathbf{s}}_2$.

For generic binaries, it is possible to derive analytical fitting formulae, if one assumes to a first approximation that: (i) the mass-energy radiated in gravitational waves is negligible (i.e., $M_{\text{fin}} = M$); (ii) the norm of the two spin vectors and of the vector $\mathbf{l} \equiv \mathbf{S}_{\text{fin}} - (\mathbf{S}_1 + \mathbf{S}_2) = \mathbf{L} - \mathbf{J}_{\text{rad}}$ (interpreted as being the residual orbital angular momentum contributing to \mathbf{S}_{fin}) do not depend on the binary separation; (iii) the final spin is parallel to the total angular momentum \mathbf{J} defined at far distances (this amounts to assuming that, according to PN theory,

the radiated angular momentum $\mathbf{J}_{\text{rad}} \parallel \mathbf{J}$, and this is motivated by the fact that precession of \mathbf{L} around \mathbf{J} averages the gravitational wave emission orthogonal to \mathbf{J});(iv) the angles γ , θ_1 and θ_2 are locked in space; (v) when the initial spins are equal and opposite ($\cos \gamma = -1$), and the masses are equal, the final black hole has spin equal to that of a non spinning binary. With these ansatz, a number of predictions can be made that are in close agreement with numerical simulations. The first is that for equal mass binaries, aligned ($s_{\text{spin}} > 0$) or anti-aligned ($s_{\text{spin}} < 0$) unequal spins,¹⁵² the final spin can be expressed as

$$s_{\text{spin}} = p_0 + p_1(s_{\text{spin},1} + s_{\text{spin},2}) + p_2(s_{\text{spin},1} + s_{\text{spin},2})^2 \quad (43)$$

where the coefficients $p_0 \simeq 0.6869$, $p_1 \simeq 0.1522$ and $p_2 \simeq -0.0081$ are obtained from independent fits to distinct data sets, and where s_{spin} takes a negative value when antialigned with respect to $\hat{\mathbf{L}}$. Equation (43) can be interpreted as power series of the initial spins and indicates that its zeroth-order term p_0 can be associated with the dimensionless orbital angular momentum not radiated in gravitational waves by a non spinning binary. This value is close to the most accurate measurement of the final spin of two non spinning black holes $s_{\text{fin}} = 0.68646 \pm 0.00004$. The first order term p_1 can be seen as the contribution to the final spin from the spins of the two black holes and their spin-orbit coupling. The last, second order term p_2 accounts for the contribution of the spin-spin couplings. Interestingly $s_{\text{spin}} = p_0$ is the final spin also for equal-mass binaries with $\mathbf{S}_1 = -\mathbf{S}_2$.

Recently, by combining information from the test-particle limit, perturbative/self-force calculations, the PN dynamics, and an extensive set of NR simulations collected from the literature, Hofmann et al.¹⁵³ have constructed a novel formula for the final spin from the merger of quasi-circular black hole binaries with arbitrary mass ratios and spins, and we defer the reader to¹⁵³ for further details.

The above equations give a prescription to calculate the final spin of the new black hole. But how can the information on the spin be extracted from the signal? The measurements of the black hole individual spins from the signal is hampered by partial degeneracies in the phase evolution which is a function of the black hole masses and the individual spin vectors. During the inspiral, for a binary with spins aligned with \mathbf{L} , the spin influence on the evolution of the phase arises in a weighted combinations of the spins projected on $\hat{\mathbf{L}}$

$$\chi_{\text{eff}} = \frac{c}{G} \left(\frac{\mathbf{S}_1}{m_1} + \frac{\mathbf{S}_2}{m_2} \right) \cdot \frac{\hat{\mathbf{L}}}{M} \quad (44)$$

which takes values between -1 (for maximally rotating black holes when both have spins antialigned with the respect to the orbital angular momentum) and +1 (aligned spins). Equation (44) implies degeneracy in the estimate of the individual spins, in particular for equal mass binaries.

When the spins have also components lying in the orbital plane, their in-plane projections rotate within the orbital plane at different velocities and the signal acquires further structure. In this case the mean influence of the four

in-plane spin components on the phasing can be combined into a single effective precession spin parameter

$$\chi_p = \frac{c}{(2+3q/2)Gm_1^2} \max[(2+3q/2)S_{1\perp}, (2+3/2q)S_{2\perp}] \quad (45)$$

where $\chi_p = 1$ (0) corresponds to a binary with maximum (null) level of precession.

For GW150914, it has been possible to measure the spin of the new black hole $s_{\text{fin}} = 0.67^{+0.05}_{-0.07}$ and $\chi_{\text{eff}} = -0.06^{+0.17}_{-0.18}$, and pose a limit on $\chi_p < 0.81$ (at 90% probability level).^{2,154} The spins of the black holes prior to coalescence have been constrained to value $s_{\text{spin},1} = 0.31^{+0.51}_{-0.27}$ and $s_{\text{spin},2} = 0.39^{+0.50}_{-0.34}$.¹⁵⁴ For GW151226, the weaker signal does not allow an estimate of s_{fin} , but from the longer-duration inspiral seen in GW151226 it has been possible to pose a lower limit on $s_{\text{spin},1} > 0.2$ at the 99% credible level. Only weak constraints have been placed on χ_p suggesting that the data are no informative on the level of precession in the binary prior to coalescence.⁵

As far as the radiated energy $E_{\text{gw}}^{\text{rad}}$ and final mass M_{fin} are concerned, the combined approach that uses fitting formulae from the PN expansion calculation calibrated with NR experiments has led to predictions on the final mass.¹⁵² Two regimes are described here as they guide intuition: (i) the test particle limit (in which $m_2 \rightarrow 0$), and (ii) the case of equal-mass binaries with spins aligned or anti-aligned with respect to the orbital angular momentum \mathbf{L} .

In the *test particle* limit, the energy radiated by m_2 during the inspiral onto the central black hole of mass m_1 (with $m_1 \gg m_2$), from large distances down to R_{isco} is

$$E_{\text{gw}}^{\text{rad}} = [1 - \tilde{E}_{\text{isco}}(s_{\text{spin}})]\nu Mc^2 + O(\nu) \quad (46)$$

where $\tilde{E}_{\text{isco}}(s_{\text{spin}})$ the binding energy per unit mass at the innermost stable circular orbit

$$\tilde{E}_{\text{isco}}(s_{\text{spin}}) = \left[1 - 2/(3R_{\text{isco},\pm}^{\text{spin}})\right]^{1/2} \quad (47)$$

where $R_{\text{isco},\pm}^{\text{spin}}$ is the coordinate radius of the innermost stable circular orbit in the Kerr metric, equal to $6GM/c^2$ for a non-spinning black hole, and GM/c^2 ($9GM/c^2$) for a maximally rotating black hole and a test particle on a co-rotating (counter-rotating) orbit. For $s_{\text{spin}} = 0$, $\tilde{E}_{\text{isco}} = \sqrt{8/9}$ while for $s_{\text{spin}} = 1$, $\tilde{E}_{\text{isco}} = \sqrt{1/3}$ ($\sqrt{25/27}$) for prograde (retrograde) orbits. The maximum radiated energy is equal to $E_{\text{gw}}^{\text{rad}} = 0.423\nu Mc^2$, for a co-rotating orbit around a maximally rotating Kerr black hole, neglecting the plunge phase and high order corrections.

The case of equal-mass binaries and both spins aligned or anti-aligned with respect to the orbital angular momentum, has been explored numerically.^{146,156} The energy emitted by these binaries during the inspiral (from infinite separation), merger and ringdown (computed by combining PN calculation to numerical relativity results) can be described by a polynomial fit¹⁵²

$$E_{\text{gw}}^{\text{rad}} = [w_{\text{ns}} + w_{\text{so}}(s_{\text{spin},1} + s_{\text{spin},2}) + w_{\text{ss}}(s_{\text{spin},1} + s_{\text{spin},2})^2]Mc^2 \quad (48)$$

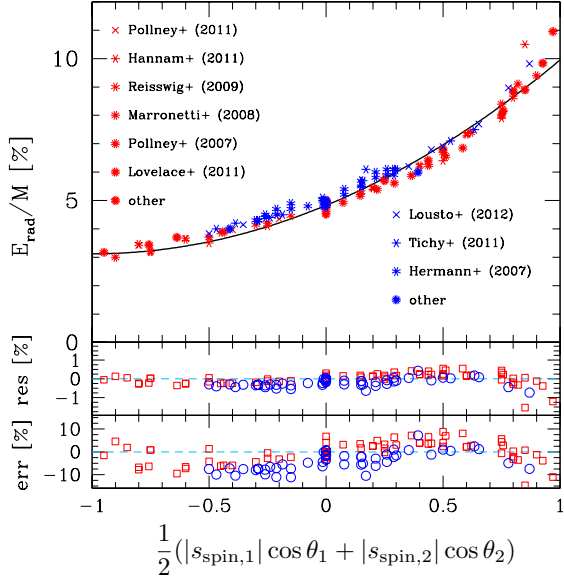


Figure 21: Radiated energy, $E_{\text{gw}}^{\text{rad}}$ per unit mass as a function of the total spin of the system projected along the orbital angular momentum, for different sets of published NR simulations of equal mass binaries, both with aligned/antialigned spins (in red) and for misaligned spins (in blue). The black solid line is the fit whose analytical expression can be found in.¹⁵⁵ Bottom panels give the residuals of the NR data from the fitting expression and the corresponding error relative to $E_{\text{gw}}^{\text{rad}}$. Courtesy by E. Barausse.

where again s_{spin} takes negative values when the spin is anti-aligned with respect to $\hat{\mathbf{L}}$. The fitting coefficients $w_{\text{ns}} = 0.04827 \pm 0.00039$, $w_{\text{so}} = 0.01707 \pm 0.00032$, and $w_{\text{ss}} = w_{\text{so}}/4$, can be interpreted as the non-spinning contribution to the radiated energy (which is the largest one and which accounts for $\sim 50\%$ of the largest possible mass loss occurring when $s_{\text{spin},1} = s_{\text{spin},2} = +1$), the spin-orbit contribution (which is $\lesssim 30\%$ of the largest possible loss) and spin-spin contribution (which is $\lesssim 20\%$ of the largest possible loss), respectively. Equation (48) reproduces the data available to within $\sim 0.005Mc^2$ except for almost extremal spins where higher order terms may be needed. This result teaches us that spin effects can either amplify or reduce the amount of energy radiated away so that binaries with given M and ν do not radiate away the same $E_{\text{gw}}^{\text{rad}}$.

In Figure 21 we show the results of NR simulations for equal mass binaries.¹⁵⁵ As illustrated in Figure 21, equal-mass, maximally spinning black holes with

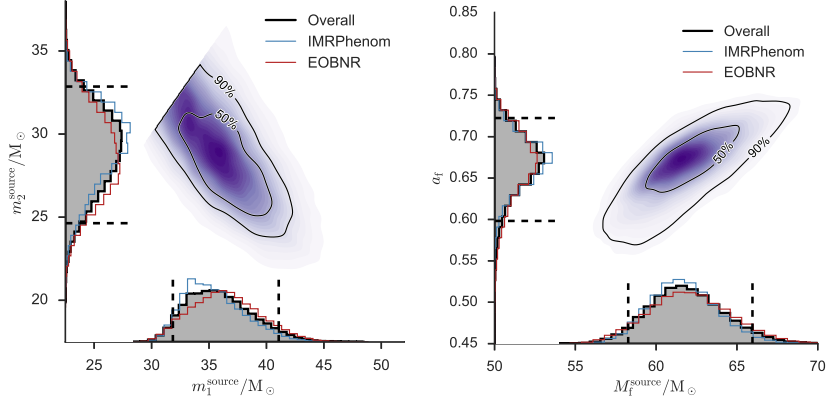


Figure 22: Probability Distribution Functions (PDFs) for the source-frame component masses m_1 and m_2 (left), and for the mass M_{fin} and spin s_{fin} (right) of the remnant black hole in GW150914.^{2,154} In the 1-dimensional marginalised distributions, the figure shows the overall (solid black), IMRPhenom (blue) and EOBNR (red) PDFs, where the acronym IMRPhenom and EOBNR refer to the two model waveforms for spinning (non-precessing) binaries used to analyse the signal. Figure adapted from Abbott et al. arXiv:1602.03840v1. For detail we defer to.¹⁵⁴ The dashed vertical lines mark the 90% credible interval for the overall PDF. The 2-dimensional plot shows the contours of the 50% and 90% credible regions plotted over a colour-coded posterior density function. Courtesy of the LIGO Scientific Collaboration and Virgo Collaboration.

spins aligned with the orbital angular momentum are the most efficient emitters of gravitational waves, with $E_{\text{gw}}^{\text{rad}} = 0.0995Mc^2$. Also equal-mass non spinning binaries lose a considerable fraction of their mass via radiation having $E_{\text{gw}}^{\text{rad}} \sim 0.048Mc^2$, while maximally spinning binaries with spins parallel but anti-aligned with the orbital angular momentum have $E_{\text{gw}}^{\text{rad}} \sim 0.037Mc^2$.¹⁵⁶ More complex fitting formulae have been derived¹⁴⁶ for generic binaries.

Figure 22 shows the Probability Distribution Functions (PDFs) for the source-frame masses of the two black holes in GW150914, and for the mass and spin of the remnant black hole.^{2,154} From these values one can infer a radiated energy of $3.0^{+0.5}_{-0.5} M_\odot c^2$, the majority of which emitted at frequencies in the LIGO sensitive band. For the second source, GW151226 we defer to.⁵

7 Waveforms and the Laws of Nature

In this section we give a brief overview on the properties of the gravitational wave signals, which inform us on the nature of the sources and on their physical properties.

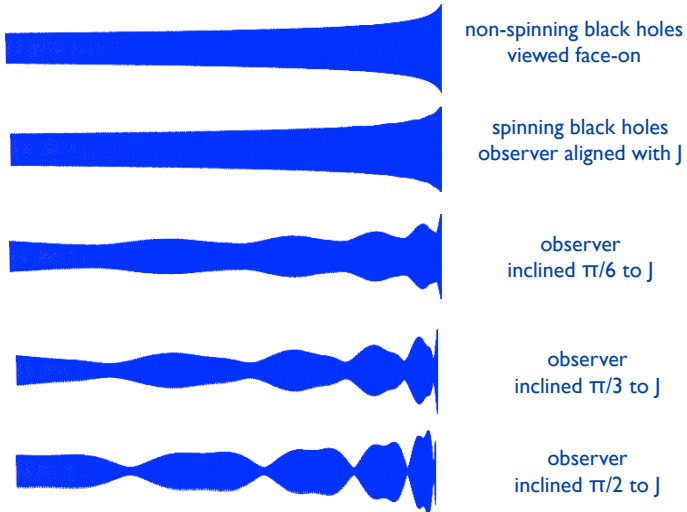


Figure 23: Waveforms from a black hole binary with mass ratio $q = 1/3$. The upper panel refers to a non-spinning binary viewed face-on, i.e. with optimal orientation corresponding to the highest signal. The remaining panels refer to a spinning binary with in-plane spin $s_{\text{spin},1} = 0.75$, and $s_{\text{spin},2} = 0$, viewed at different angles with respect to the total angular momentum \mathbf{J} . The morphology changes with the viewing angle, and the modulation by precession is absent when the binary is seen along \mathbf{J} . Adapted from M. Hannam talk, Hannover 24 May 2016 : <https://gw150914.aei.mpg.de/program/mark-hannams-talk>

7.1 Black hole binary coalescences

Black hole binaries (BH*,BH*) of stellar origin, or massive (MBH,MBH) have universal signals as black holes are geometrical objects, according to general relativity. Spin-precession colours the waveform in various ways, changing the morphology. This is illustrated in Figure 23 where we show the spin-induced modulation on the gravitational wave amplitude, during the inspiral phase, as view from different orientations with respect to the observer's viewing angle.

For an accurate measure of the physical parameters and in order to break degeneracies, one needs to know the full waveform and detect a source with a high signal-to-noise ratio.

The whole waveform (including the ringdown) contains precious information on the mass and spin of the new black hole. We recall that if the object is truly a black hole as predicated by general relativity, then the mass and spin obtained from the different oscillation modes present in the ringdown signal should all be consistent within the measurement errors.^{105,128} Inconsistencies

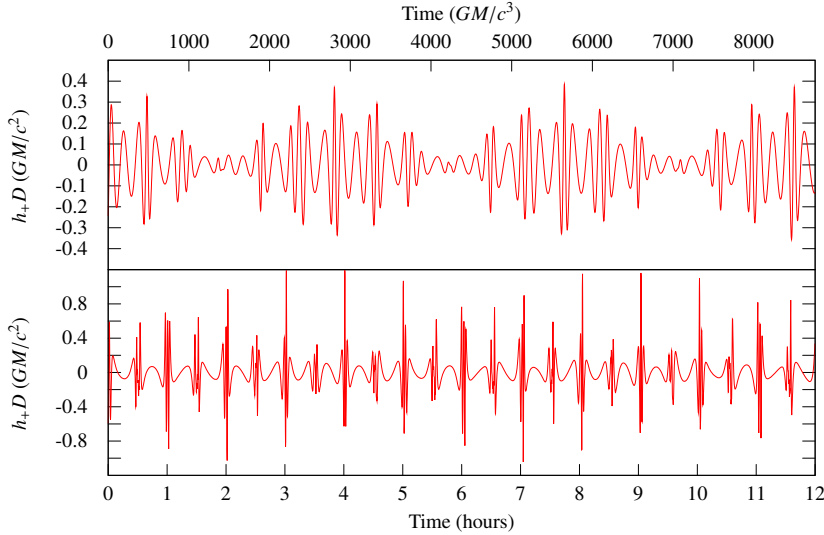


Figure 24: Segments of generic EMRI waveforms.⁹ These are the plus-polarised waves produced by a test mass orbiting a $10^6 M_\odot$ spinning black hole with $s_{\text{spin},1} = 0.9$, at distance D from the observer. Top panel: Slightly eccentric and inclined retrograde orbit modestly far from the horizon. Bottom panel: Highly eccentric and inclined prograde orbit much closer to the horizon. The amplitude modulation visible in the top panel is mostly due to Lense-Thirring precession of the orbital plane. The more eccentric orbit in the bottom panel produces sharp spikes at each pericentre passage.

in the values of the mass and spin inferred in this way would be an indication of the failure of general relativity or that the radiation was emitted from an object that is not a black hole. Test of consistency with the early inspiral and merging phase will also be critical, providing extremely valuable information, both on the nature of the interacting bodies and on the properties of gravity, as fundamental interaction.

7.2 Extreme Mass Ratio Inspirals

EMRI are expected to be very clean astrophysical systems, except perhaps in the few percent of galaxies containing accreting massive black holes, where interactions with the accretion disc could possibly affect the EMRI dynamics and waveform. EMRIs trace geodesics in the spacetime of the massive black

hole. Over a typical eLISA observation time (months to years), EMRI orbits are highly relativistic (radii smaller than $10 R_S$) and display extreme forms of periastron and orbital plane precession due to the dragging of inertial frames by the massive black holes spin, as illustrated in Figure 24.

Given the large amount of gravitational wave cycles collected in a typical EMRI observation ($\mathcal{N}_{\text{cycle}} \sim 10^5$), a fit of the observed gravitational waves to theoretically calculated templates will be very sensitive to small changes in the physical parameters of the system. eLISA should be able to determine the mass of the massive black hole to fractional accuracy of about $10^{-3} - 10^{-4}$ for gravitational wave signals with an SNR of 20 and the spin with 10^{-3} in its absolute value.

This level of precision suggests that we can use EMRIs for highly precise observational tests of the *Kerr-ness* of the central massive object.^{105,128,157} That is, if we do not assume that the larger object is a black hole, we can use gravitational waves from an EMRI to map the spacetime of that object. The spacetime outside a stationary axisymmetric object is fully determined by its mass moments M_l and current multipole moments S_l . Since these moments fully characterise the spacetime, the orbits of the smaller object and the gravitational waves it emits are determined by the multipolar structure of the spacetime. Extracting the moments from the EMRI waves is analogous to geodesy. Black hole geodesy, also known as holiodesy, is very powerful because Kerr black holes have a very special multipolar structure. In units with $G = c = 1$, a Kerr black hole has multipole moments given by

$$M_l + iS_l = (is_{\text{spin}})^l M_{\text{BH}}^{l+1}, \quad (49)$$

where M_{BH} is the mass of the large black hole. Thus, $M_0 = M_{\text{BH}}$, $S_1 = s_{\text{spin}} M_{\text{BH}}^2$, and $M_2 = -s_{\text{spin}}^2 M_{\text{BH}}^3$, and similarly for all other multipole moments; they are all completely determined by the first two moments, the black hole mass and spin. This is equivalent of stating the black hole 'no-hair' theorem: the properties of a black hole are entirely determined by its mass and spin. The mass moment M_2 will be measured with extreme accuracy by eLISA, for a signal-to-noise-ratio larger than 30.

Any inconsistency with the Kerr multipole structure could signal a failure of general relativity, the discovery of a new type of compact object, or a surprisingly strong perturbation from some other material or object. EMRI signals can be used to distinguish definitively between a central massive black hole and a boson star.¹⁰⁷ In the black hole case the gravitational wave signal "shuts off" shortly after the inspiraling body reaches the last stable orbit (and then plunges through the event horizon), while for a massive boson star, the signal does not fade, and its frequency derivative changes sign, as the body enters the boson star and spirals toward its centre.^{105,157}

7.3 Neutron star binary coalescences

Neutron stars have a surface and are deformable bodies. In the latest moments of the inspiral of a (NS,BH*) or (NS,NS) binary, the tidal interaction becomes

important. The neutron star acquires a tidal deformation, and this affects the external gravitational field and the relative orbital motion. Thus the deformability of each star leaves a subtle signature in the amplitude and phasing of the gravitational wave.

The effect of the tidal interaction on the orbital motion and gravitational wave signal is measured by a quantity known as *tidal Love number*, defined for each body in the binary. To guide intuition, let us treat the first body (either one of the two NS or BH*) as a point mass sourcing the external monopole potential U_{ext} , and focus on the tidal deformation on the second body excited by U_{ext} . The deformed mass distribution can be described in terms of a quadrupolar deformation Q_{ab} which turns out to be proportional to the external tidal field, $T_{ab} = -\partial_a \partial_b U_{\text{ext}}$. Dimensional analysis requires $Q_{ab} = -2/(3G)\kappa R^5 T_{ab}$, where κ is the tidal Love number for the quadrupolar deformation, and R the stellar radius. The resulting external gravitational potential, relative to the centre of mass of the deformed body, is

$$U = \frac{Gm_2}{r} - \frac{1}{2} \left[1 + 2\kappa \left(\frac{R}{r} \right)^5 \right] T_{ab} x^a x^b, \quad (50)$$

the first term representing the monopole contribution, the second the gravitational potential by the point mass sourcing the tide, and the third the correction to the gravity's field induced by the distorted mass distribution.

The formalism has been extended within the framework of general relativity^{133,159,160} and the quadrupolar Love number κ has been computed for neutron stars with different EoS: $\kappa = 0.11$ for the lowest $\mathcal{C} = 0.139$, and $\kappa = 0.0647$ for the highest $\mathcal{C} = 0.1924$. Interestingly enough, non-spinning black holes have zero Love numbers. Both the compactness \mathcal{C} and Love number κ enter the evolution of the orbital phase, and with Advanced LIGO and Virgo it will be possible to measure the degree of tidal polarisability, defined as $2/(3G)\kappa R^5$, for neutron stars when the signal-to-noise ratio is sufficiently high (~ 16), opening the prospects of extracting information on the nuclear EoS from a coherent analysis of an ensemble of gravitational wave observations of separate binary merger events.^{133,160}

After being tidally deformed and shock heated at impact, the two neutron stars merge, and depending on the total mass of the binary, they may form a black hole or a hyper-massive neutron star which may later collapse into a black hole. The merger and ringdown phases can only be followed numerically, and Figure 25 shows the coalescence of two equal-mass (non magnetised) neutron stars forming a hyper-massive neutron star.¹⁵⁸ During the late inspiral, the two stars develop strong deformations due to the tides that they mutually exert, and after merging the highly non-symmetric hyper-massive star is surrounded by tidal debris.

Binary neutron star mergers have been simulated, within the context of NR, in order to explore a variety of EoS²¹ and to extract and study the morphology of the gravitational wave signal, and in particular its evolution in the frequency domain, in search of characteristic frequencies that may inform us about the

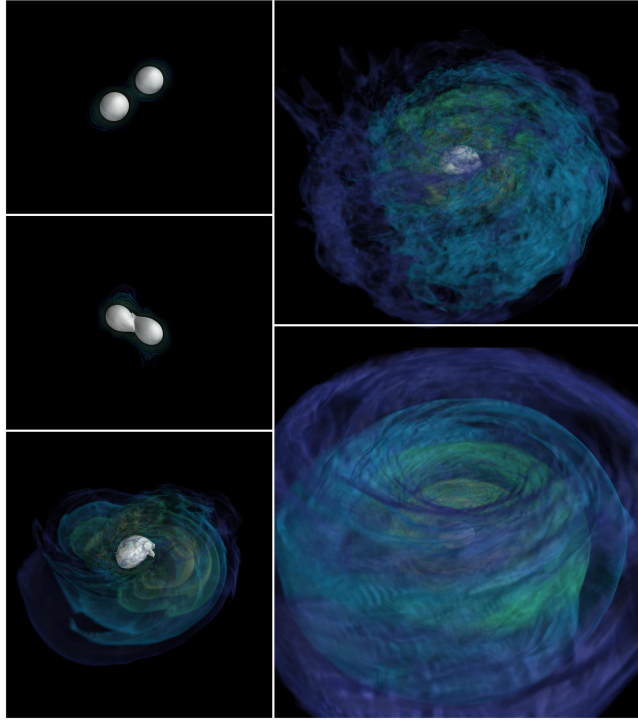


Figure 25: The figure depicts a merger of an equal-mass (NS,NS) binary.¹⁵⁸ The two neutron stars (drawn in white) spiral-in (top left panel), touch (middle left), and merge into a hyper-massive neutron star while ejecting debris (bottom left). Most of the ejecta form a torus orbiting around the remnant (right panels), while the rest escapes. Courtesy of B. Giacomazzo.

degree of compactness of the two merging neutron stars.^{133,162}

Figure 26 collects an inventory of gravitational wave signals from equal-mass binaries simulated with different EoS, shown in different colours. Each column refers to a given initial gravitational mass and we defer to^{21,161} for details. Figure 26 shows that the gravitational wave signal from (NS,NS) mergers does not show a rapid decay (as in the case of a (BH*,BH*) coalescence) as the hyper-massive neutron star that forms undergoes violent oscillation modes prior to collapse into a black hole.

In the Fourier domain, each signal carries precious information on the compactness \mathcal{C} of the neutron stars. This is illustrated in Figure 27 where the spectral density $2\tilde{h}(f)\sqrt{f}$ is plotted against the frequency f of the wave, for two selected models.¹⁶¹ The low frequency dotted line corresponds to the inspiral phase which is then followed by a sequence of three prominent peaks with different amplitudes. Those are related to the oscillations of the hyper-massive neu-

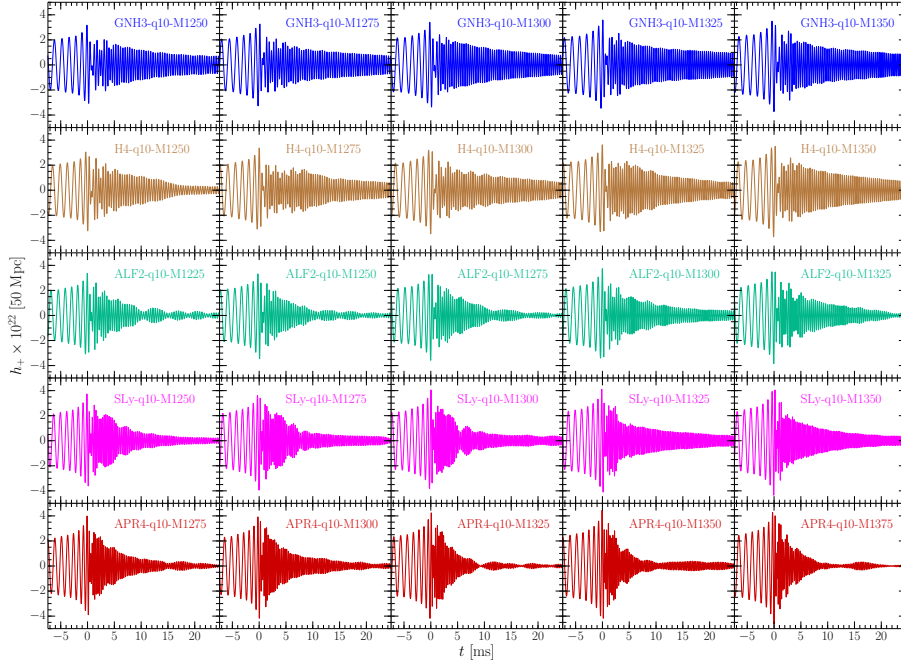


Figure 26: Gravitational wave signals $h_+(t) \times 10^{22}$ for sources at 50 Mpc, from a large suite of equal-mass (NS,NS) coalescences and for a variety of nucleonic EoS, from.^{21,161} Courtesy of L. Rezzolla.

tron star, and would be absent or much smaller if a black hole forms promptly. In this latter case, the gravitational-wave signal would terminate abruptly with a cut-off corresponding to the fundamental quasi-normal-mode frequency of the black hole. The behaviour summarised in Figure 27 has been investigated by a number of authors over the last decade. As of today, there is a widespread consensus that: (i) the post-merger gravitational wave signal possesses spectral features that are robust and that emerge irrespective of the EoS or the mass ratio; (ii) the frequencies of the peaks, referred to as "contact frequencies" in the post-merger signal can be used to obtain important information on the stellar properties (i.e. mass and radius) and hence represent a very good proxy to deduce the EoS.

7.4 Electromagnetic counterparts of CBCs

Very recent magneto-hydrodynamical simulations in general relativity of (NS,NS) mergers with an initially high, but dynamically weak magnetic field, have proven that at the end of the merger an incipient jet forms around the remnant.¹⁶⁴ This occurs following the delayed collapse of a hyper-massive neutron star into a black

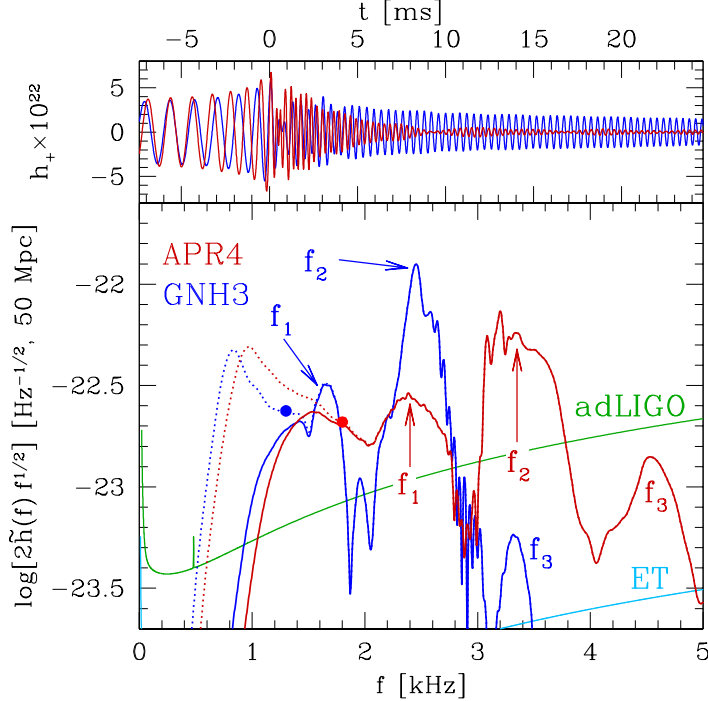


Figure 27: This figure from¹⁶¹ shows in the top panel the evolution of h_+ from the coalescence of equal-mass (NS,NS) binaries at a distance of 50 Mpc (the two curves refer to two selected EoS (APR4 dark-red and GNH3 EoSs blue lines). The bottom panel shows the wave spectral density $2\tilde{h}(f)\sqrt{f}$ versus frequency f windowed after the merger, for the two EoSs. The sensitivity curves of Advanced LIGO (green line) and ET (light-blue line) are also plotted. The dotted lines show the spectral density in the inspiral, while the circles mark the contact frequency $f_{\text{cont}} = \mathcal{C}^{3/2}/(2\pi\bar{M})$, where $\mathcal{C} = \bar{M}/\bar{R}$ is the average compactness, with \bar{M} the initial gravitational mass of the two stars, $\bar{R} = (R_1 + R_2)/2$, and $R_{1,2}$ are the radii of the non-rotating stars associated with each binary. The frequency f_1 appears to correlate closely with the compactness \mathcal{C} of the stars. See¹⁶¹ for details. Courtesy of L. Rezzolla.

hole, 60 ms after the merger. The region above the black hole poles becomes strongly magnetised, and a collimated, mildly relativistic outflow is launched. Figure 28 gives a glimpse into the merger of a (BH*,NS) binary with mass ratio 3:1. In this simulation,¹⁶³ the mass ratio is not extreme and the neutron star is tidally disrupted as a whole, so that the black hole ends being enshrouded by a torus of debris representing the leftover of the star that is torn apart by the intense tidal field of the black hole. A weak magnetic dipole field was seeded in

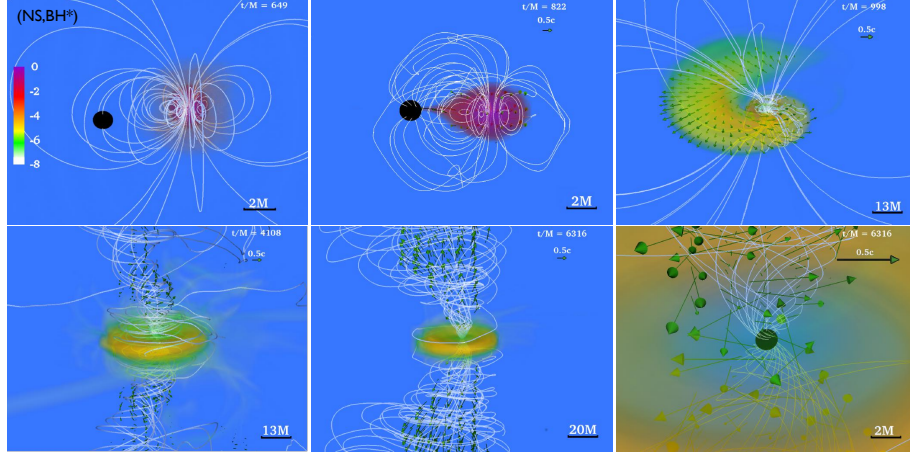


Figure 28: Magnetohydrodynamical simulation in general relativity of the merger of a (BH*,NS) binary with 3 to 1 ratio. Figure adapted from.¹⁶³ The black hole is rotating with spin $s_{\text{spin}} = 0.75$ aligned with the orbital angular momentum. About two orbits prior to merger, a dynamically weak interior dipole magnetic field is seeded into the neutron star. The figure shows snapshots of the rest-mass density in log-scale, in units of $8.92 \times 10^{14} (1.4 M_{\odot}/M_{\text{NS}})^2 \text{ gr cm}^{-3}$, at different times t/M . Here, time is in units of $2.5 \times 10^{-3} (M_{\text{NS}}/1.4 M_{\odot}) \text{ ms} = 7.58 (M_{\text{NS}}/1.4 M_{\odot}) \text{ km}$. Arrows indicate plasma velocities and white lines show the magnetic field lines. Bottom panels highlight the system after an incipient jet is launched. The scale-size in each panel is indicated on the right bottom corner in units of M . Courtesy of S. Shapiro.

the neutron star extending to the exterior, which is responsible for the launch of an incipient jet which could account for the energetics of a short GRB.

One of the current challenges of Advanced LIGO and Virgo is to detect the electromagnetic counterparts of (NS,NS) and/or (NS,BH*) merger events related to outflows produced during the merger and post-merger phases, as illustrated in Figure 29. This would have a tremendous impact as it will prove the origin of short GRBs as coalescing binaries,¹⁶⁵ and will open the possibility of identifying the host galaxy and thus the redshift of the source opening the possibility of using (NS,NS) and (NS,BH*) mergers as standard sirens.¹³⁸

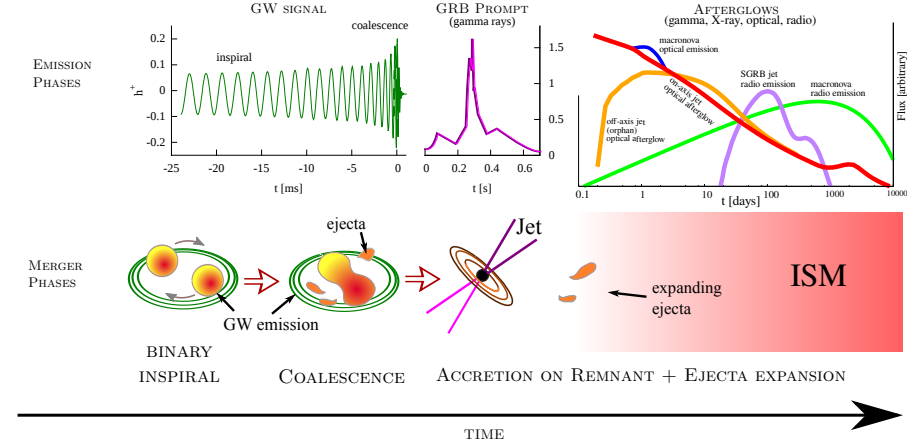


Figure 29: Electromagnetic follow up of a (NS,NS) merger event. See text for the description of the figure.

In more detail, the tidal interaction between the two neutron stars during the merger phase very likely leads to nearly isotropic ejection of neutron rich material. Due to the subsequent expansion, such material undergoes rapid r -process nucleosynthesis, followed by radioactive decay of unstable isotopes, thus producing a short-lived optical/near-IR transient, known as *macronova* (blue solid line in Figure 29) lasting hours to days after the merger.¹⁶⁶ The same ejecta may also produce a long-lived radio transient (green solid line), lasting months to years, due to the interaction with the surrounding interstellar medium.¹⁶⁷ In the post-merger phase, rapid accretion of a centrifugally supported disc on the compact remnant powers a collimated relativistic jet of semi-aperture θ_{jet} , which produces a short GRB.¹⁶⁵ Prompt collimated emission at gamma-ray energies (violet solid line in the top-middle plot) is followed by extended, lower energy emission (afterglow), due to the interaction of ejecta with the interstellar medium. Owing to relativistic beaming, the gamma-ray emission is visible to observers with viewing angle within the narrow cone of the jetted emission. Optical afterglow emission (red and orange solid lines) is detectable by observers at angles $\lesssim 2\theta_{\text{jet}}$. Radio afterglow emission (purple solid line) is observable from all viewing angles once the jet decelerates to mildly relativistic velocities on a

timescale of weeks to months (up to years, depending on the inter-stellar medium density and jet energy).

7.5 Core-collapse supernovae

Electromagnetic observations suggest that many, if not most, core collapse supernova explosions exhibit asymmetric features, and this is also suggested by results of multidimensional simulations. Thus, core collapse supernovae (CCSNe) are likely to be accompanied by emission of gravitational waves, associated to the quadrupole mass-energy dynamics.⁹⁴ Spherical symmetry could be broken by stellar rotation, convection in the proto-neutron star and in the region behind the shock, and by the standing accretion shock instability. State-of-the-art models predict strains $h \sim 10^{-23} - 10^{-20}$ for core collapse events at 10 kpc with frequencies of ~ 1 to 1000 Hz, and total emitted energies in gravitational waves of $10^{42} - 10^{47}$ erg, corresponding to $10^{-12} - 10^{-7} M_\odot c^2$.

There is a garden-variety of signals expected from CCSNe and in Figure 30 we show, as an illustration, the waveform expected from four representative models.¹⁶⁸ In the left panel, the strain from a neutrino (upper left) and rotation (lower left) driven CCSN are seen by an equatorial observer at 10 kpc. The wave from the neutrino-driven deformation carries two polarisation states, and is characterised by a long-lived signal with complex time-domain structure. The rotation-driven instability leads to oblateness and to an $l = 2, m = 0$ quadrupole deformation of the inner quasi-homologously collapsing core. The extreme accelerations experienced by the inner core at bounce lead to a large spike in the gravitational wave signal, followed by ring-down of the proto-neutron star as it settles to its new equilibrium state. In contrast, the right panels of Figure 30 show the signal from a differentially rapidly rotating proto-neutron star unstable to a bar-mode instability $m = 2$ (upper right panel), modelled in the quadrupole approximation as a sine-Gaussian morphology.¹⁶⁸ If the CCSN mechanism fails to re-energize the stalled shock, the proto-neutron star will collapse to a black hole, due to fall-back on a timescale set by accretion. Provided matter has sufficient angular momentum, a massive self-gravitating accretion disc/torus may form around the nascent stellar mass black hole. The inner regions of the disc are geometrically thin due to efficient neutrino cooling, but outer regions are thick and may be gravitationally unstable to fragmentation at large radii. The predicted signal shown in the lower right panel comes instead from orbiting fragments around the newly formed black hole.

7.6 Signal from a cosmological background of supermassive black holes

We are now in the position to characterise, after §5, the cosmological background of gravitational waves resulting from the incoherent superposition of SMBHBs still away from coalescence, and to possibly identify individual sources.

Following,¹⁶⁹ the characteristic amplitude of this cosmic background can be

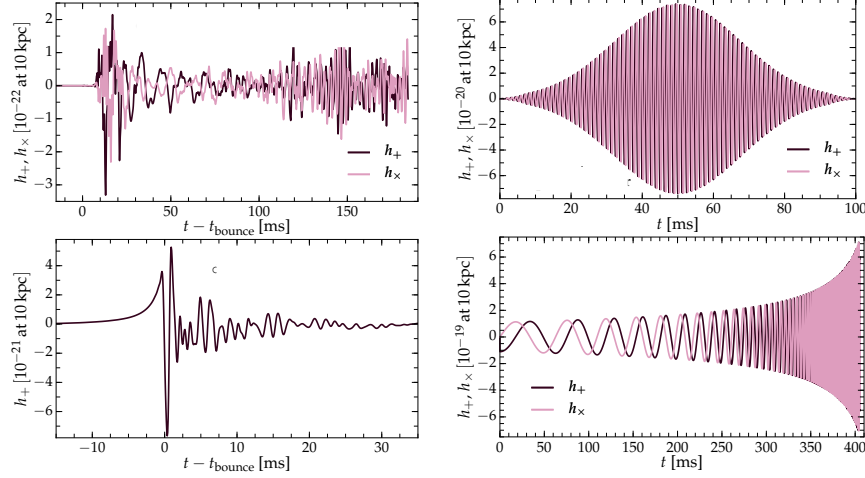


Figure 30: Inventory of waveforms from CCNSe, adapted from.¹⁶⁸ Left panels show the strain for a neutrino (top) and rotation (bottom) driven core collapse as seen from an equatorial observer at a distance of 10 kpc. Right panels show the strain from a bar-mode (top) and disc fragmentation instability (bottom), as seen by a polar observer at 10 kpc, calculated to leading (quadrupole) order from simple analytical models of the instabilities. Courtesy of S.E. Gossan.

written as

$$h_c^2(f) = \int_0^\infty dz \int_0^\infty dM_c \frac{d^3 N}{dz dM_c d\ln f_r} h^2(f_r), \quad (51)$$

where $f_r = (1+z)f$, $d^3 N/dz dM_c d\ln f_r$ is the comoving number of binaries with chirp mass and redshift in the range $[M_c, M_c + dM_c]$ and $[z, z + dz]$, emitting in a given logarithmic frequency interval f_r . In the approximation of quasi circular binaries, $h(f_r)$ is the inclination–polarisation averaged strain given by

$$h(f_r) = \left(\frac{8\pi^{2/3}}{10^{1/2}} \right) \frac{1}{d_L} \left(\frac{GM_c}{c^2} \right)^{5/3} \left(\frac{\pi f_r}{c} \right)^{2/3}, \quad (52)$$

where d_L its luminosity distance to the source.¹⁶⁹ It is straightforward to show that for SMBHBs driven by gravitational wave emission, equation (51) results in a spectrum of the form $h_c = A(f/f_0)^{-2/3}$. The normalisation A encodes information about the cosmic population of SMBHBs and directly depends on

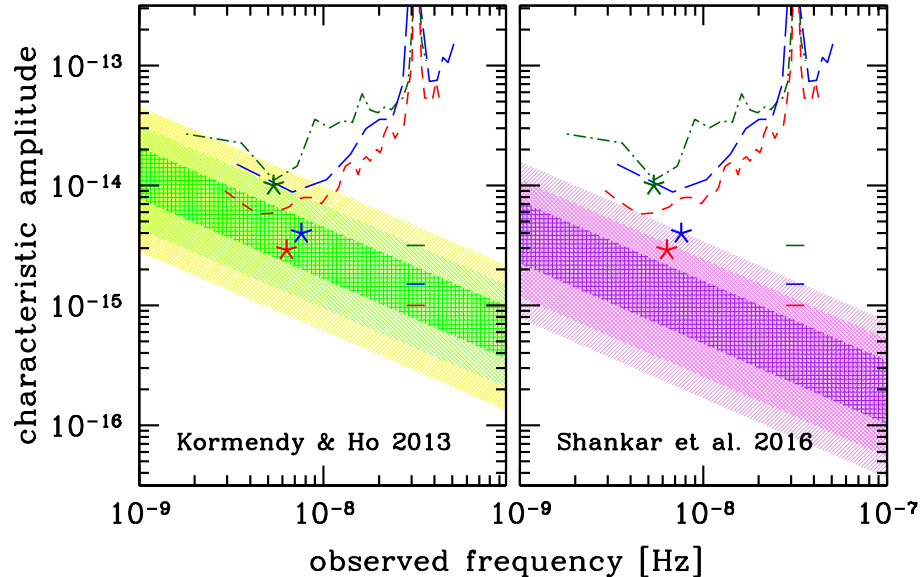


Figure 31: Characteristic amplitude of the gravitational wave background assuming specific M_{BH} -galaxy correlations as indicated in.¹²⁴ In each panel, shaded areas define the 68%, 95% and 99.7% confidence intervals of the signal amplitude. Jagged curves represent current PTA sensitivities: EPTA (dot-dashed green), NANOGrav (long-dashed blue), and PPTA (short-dashed red). Stars represent the integrated upper limits to an $f^{-2/3}$ background coming from each sensitivity curve, and the horizontal ticks are their extrapolation at $f = 1\text{yr}^{-1}$.

the rate of massive galaxy mergers, on the intrinsic relations between the properties of the galaxies and the mass of the SMBHs they host, and on the pairing efficiency of SMBHs following galaxy mergers. Figure 31 shows examples of the uncertainty in the expected signal level, assuming two specific M_{BH} -galaxy correlations from the literature. The figure also shows up-to-date sensitivities from the three major PTAs, which started to pierce into the range predicted by SMBHB population models. A detection of the signal is expected within the next decade, also aided by the advent of new observational facilities such as MeerKAT, FAST and SKA.¹⁷⁰

If A encodes information about the abundance and mass distribution of SMBHBs in the universe, the shape of the spectrum critically depends on the dynamical properties of SMBHBs on their path to final coalescence.¹²⁴ The $f^{-2/3}$ spectrum is in fact valid only in the circular gravitational wave driven approximation; coupling to the stellar and gaseous environment, necessary to shrink the binaries at sub-pc scales, as well as significant eccentricities will modify the shape of the spectrum at the low end, possibly causing a turnover.

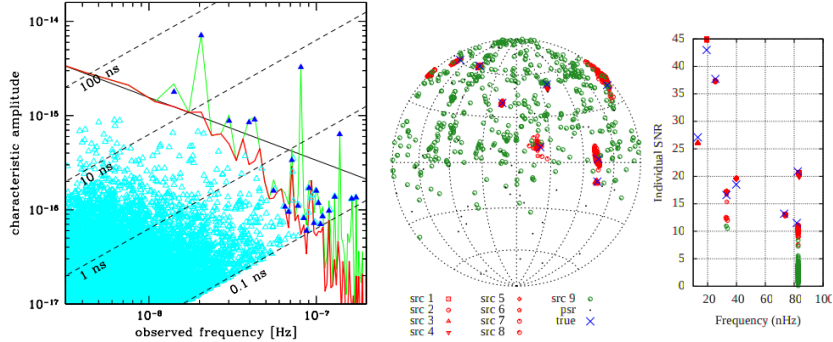


Figure 32: The left panel shows characteristic amplitude versus frequency of a Monte Carlo realisation of the gravitational wave signal from SMBHBs. Each cyan point represents the emission of an individual binary and blue triangles are individually resolvable sources. The green (red) line is the collective signal including (subtracting) resolvable sources. The black solid line is the expected analytical $f^{-2/3}$ power law, and the black dashed lines represent different timing residual levels. Adapted from.¹²⁴ The right panel, adapted from¹⁷¹ represents an exercise of individual SMBHB recovery in simulated PTA data. The blue crosses represent injected sources, whereas the clusters of red points are the signal recovered by a Multi-Modal genetic algorithm running on the synthetic dataset. This shows PTA potential of correctly identifying multiple SMBHBs.

Observation and characterisation of the background shape will therefore provide unique insights on the population and dynamics of sub-parsec SMBHBs.¹²²

As far as resolvable SMBHBs are concerned, the $f^{-2/3}$ power-law shown in Figure 31 is an approximation to a much more complex reality. Especially at $f > 10\text{nHz}$, the signal enters in a low-number statistic regime, and is typically dominated by few sources. This is elucidated in the left panel of Figure 32, in which the blue triangles highlight SMBHBs that rise above the confusion noise generated by the overall population, and therefore can potentially be detected individually. These are, however, very low frequency signals involving SMBHBs far from coalescence. As such, they are essentially monochromatic and only few cycles can be observed, making a reliable estimate of basic parameters such as the source chirp mass extremely difficult. However PTAs can reconstruct the source localisation in the sky within tens of deg² thanks to triangulation. This will make it possible to follow-up the interesting regions in the sky in search for electromagnetic periodic signals, likely associated to the presence of a circumbinary massive disc which envelopes the SMBHB. This possibility will open new avenues in multi-messenger astronomy as shown in the right panel of Figure 32. A counterpart identification would, for example, enable the measurement of the redshift (and thus distance, assuming a cosmological model) to the source, thus allowing a precise measurement of the SMBHB chirp mass. Although

the first PTA detection is expected to involve the unresolved gravitational wave background, several SMBHBs will eventually be individually resolved, providing another formidable tool to study the astrophysics of supermassive black holes.

8 Conclusion

This Chapter is a first attempt to describe the *multi-band gravitational wave universe* in a unified way. *Binaries* of all flavours have been our main actors, and in Figure 33 we show their signals sweeping across the different frequency intervals. We have demonstrated that the information gathered in the gravitational waves emitted by these sources is immense as will make it possible to answer to the deep and urgent questions posed in the beginning of this Chapter: on the Laws of Nature, on the intimate link between stellar and galaxy formation and evolution processes, and on the geometry of the universe itself.ⁱ

A new, golden era of exploration of the universe has started. Detecting the vibrations of spacetime will let us explore the cosmos from a new perspective. This is thanks to the major advances we witnessed in experimental physics: laser interferometry proves to be successful and powerful in detecting the minuscule perturbations of spacetime produced by cosmic sources. The discovery of GW150914 and GW151226 represents the culmination of an experimental research able to achieve strain noise sensitivities at the level of $10^{-23} \text{ Hz}^{-1/2}$ around 200 Hz.^{2,172}

On the 8th of June 2016, ESA announced to the public the first results of the LISA Pathfinder in-flight experiment at the Sun-Earth Lagrangian point, designed to measure the level of residual acceleration noise on two test masses free-falling with respect to a local inertial frame. The results¹⁷³ beautifully demonstrate that the two masses can be put and remain in "free fall" with a relative acceleration noise characterised by a power spectral density of $5.2 \pm 0.1 \text{ fm s}^{-2} \text{ Hz}^{-1/2}$ corresponding to $0.56 \pm 0.01 \times 10^{-15} g \text{ Hz}^{-1/2}$ with g the standard acceleration gravity on Earth.¹⁷³ The result of the LISA Pathfinder experiment shows that the technology on board meets the requirement for a space based gravitational wave observatory with a sensitivity close to what was originally foreseen for LISA. With an expected launch of a LISA-like Observatory by 2030, the gravitational wave universe will be scrutinised across all accessible frequency bands from nano-Hz, to mHz and kHz.

The high, low and very low frequency gravitational universes which encompass the multi-band universe should not be perceived as disconnected. They are instead inter-winded, and Figure 34 shows beautifully how profound is the level of reciprocity. The detection of GW150914 has and will have profound implications for the science in the mHz regime. It has in fact became clear that, besides the vast population of galactic compact binaries, the future LISA-like interferometer in space might detect up to $O(10^3)$ "heavy" GW150914 like (BH*,BH*) binaries out to $z \approx 0.5$.¹⁷⁴ GW150914 itself, five years prior to

ⁱWe regret for not having described the cosmic background(s) from the very early universe, for length limitations. We defer to¹¹⁹ for a review.

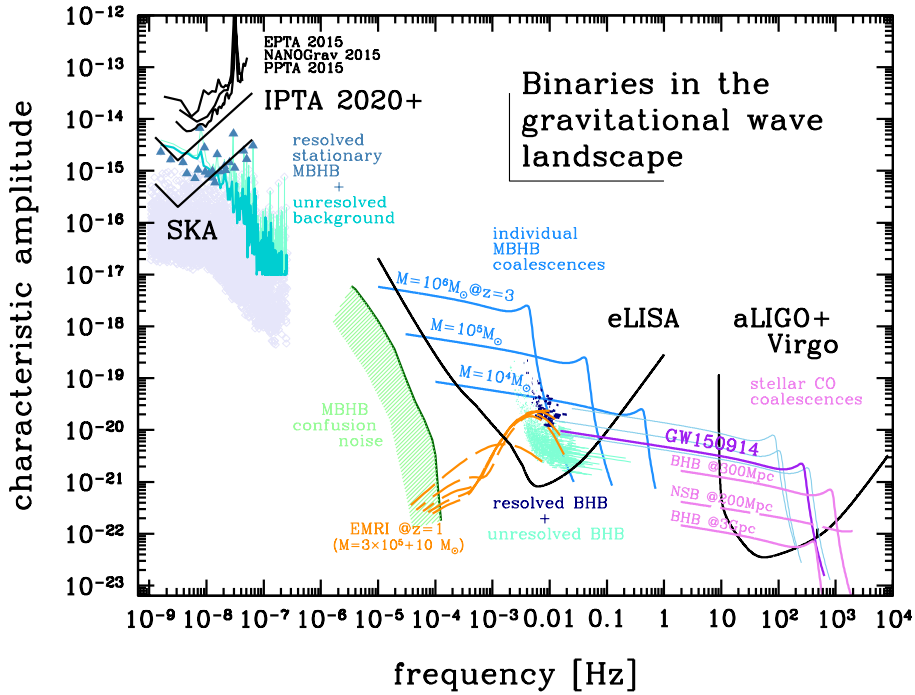


Figure 33: Binaries in the gravitational wave universe. The Figure shows the dimensionless characteristic strain amplitude in Fourier space versus frequency, from black hole binaries of all flavours, and of neutron star binaries, as described in this Chapter. Plotted are also the sensitivity curves of PTA, eLISA, and Advanced LIGO and Virgo. In eLISA and LIGO-Virgo, merging binaries above the sensitivity curve can be detected with a signal-to-noise ratio that can be computed from (31), and sweep across the sensitivity band increasing their frequency up to coalescence. At the lowest frequencies $\sim 10^{-8}$ Hz of PTA, inspiralling supermassive black hole binaries of $10^9\text{--}10^{10} M_\odot$ give rise to a stochastic background contaminated by individual, loud sources. Around \sim mHz frequencies of eLISA coalescing binary black holes weighing $10^{4\text{--}7} M_\odot$ are the main sources. They sweep across the band months before merging. Together with EMRIs, they stand out from an hypothetical background of binaries like GW150914 and of Galactic WD-WD binaries (signal not shown to keep the figure readable). At the highest frequencies accessible with Advanced LIGO-Virgo, coalescing stellar origin black holes and neutron stars are the main sources and sweep across the band in minutes to a fraction of a second. GW150914 sweeps first in the eLISA band and emerges again in the LIGO and Virgo sensitivity range at the time of coalescence (see Figure 34).

coalescence, was emitting gravitational waves at about 15 mHz, accumulating a

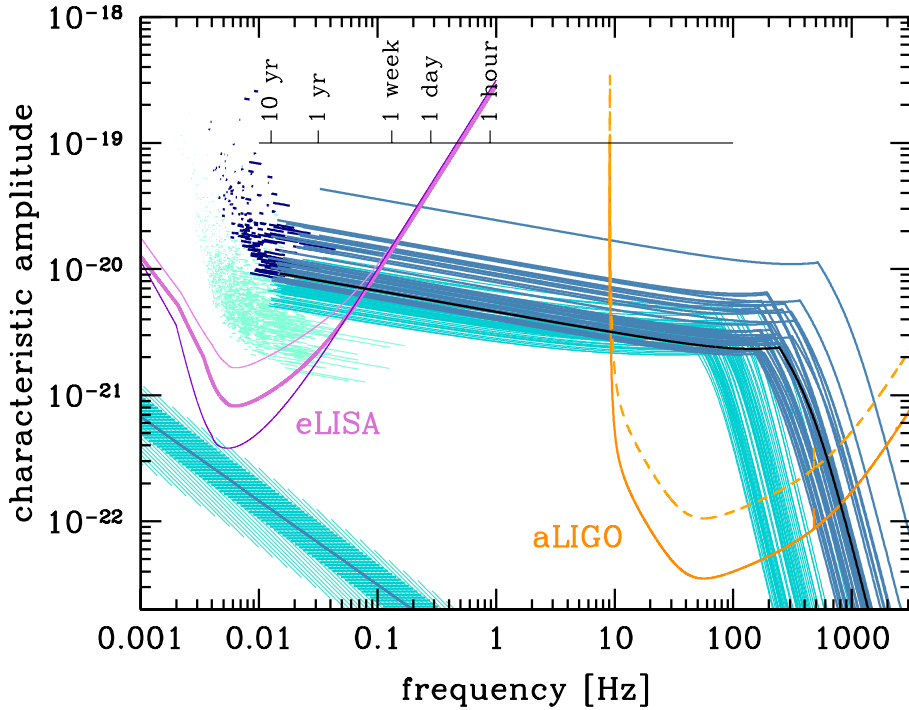


Figure 34: Multi-band gravitational wave astronomy of $(\text{BH}^*, \text{BH}^*)$ binaries, adapted from.¹⁷⁴ Plotted is the dimensionless characteristic amplitude versus frequency as in Figure 33. The violet lines are the sensitivity curves of three eLISA configurations; from top to bottom N2A1, N2A2, N2A5.¹⁷⁵ The orange lines are the current (dashed) and design (solid) Advanced LIGO sensitivity curves.¹⁷² Blue lines represent tracks of a sample of $(\text{BH}^*, \text{BH}^*)$ binaries. The light turquoise lines are systems with signal-to-noise ratio (SNR) between 1 and 5 in the eLISA band. The light and dark blue curves crossing the Advanced LIGO band are sources with $\text{SNR} > 5$ and $\text{SNR} > 8$ respectively in eLISA; the dark blue ticks are binaries with $\text{SNR} > 8$ in eLISA not crossing the Advanced LIGO band within five years. The characteristic amplitude track completed by GW150914 is shown as a black solid line, with the top label indicating its frequency progression in the last 10 years before coalescence.

signal-to-noise ratio of ≈ 10 , sweeping across the eLISA window as shown in Figure 34. Although rates are still uncertain and will be constrained by Advanced LIGO and Virgo in their forthcoming runs, the detection of several such "heavy" $(\text{BH}^*, \text{BH}^*)$ binaries in both mHz and kHz bands will open the era of *multi-band "correlated" gravitational wave astronomy*, with profound implications for tests of general relativity and multi-messenger astronomy.

References

1. B. P. Abbott, R. Abbott, T. D. Abbott, M. R. Abernathy, F. Acernese, K. Ackley, C. Adams, T. Adams, P. Addesso, R. X. Adhikari, and et al., Prospects for Observing and Localizing Gravitational-Wave Transients with Advanced LIGO and Advanced Virgo, *Living Reviews in Relativity*. **19** (Feb., 2016). doi: 10.1007/lrr-2016-1.
2. B. P. Abbott, R. Abbott, T. D. Abbott, M. R. Abernathy, F. Acernese, K. Ackley, C. Adams, T. Adams, P. Addesso, R. X. Adhikari, and et al., Observation of Gravitational Waves from a Binary Black Hole Merger, *Physical Review Letters*. 116(6):061102 (Feb., 2016). doi: 10.1103/PhysRevLett.116.061102.
3. V. Cardoso, E. Franzin, and P. Pani, Is the Gravitational-Wave Ringdown a Probe of the Event Horizon?, *Physical Review Letters*. 116(17):171101 (Apr., 2016). doi: 10.1103/PhysRevLett.116.171101.
4. V. Cardoso and L. Gualtieri, Testing the black hole 'no-hair' hypothesis, *Classical and Quantum Gravity*. 33(17):174001 (Sept., 2016). doi: 10.1088/0264-9381/33/17/174001.
5. B. P. e. a. Abbott, Gw151226: Observation of gravitational waves from a 22-solar-mass binary black hole coalescence, *Phys. Rev. Lett.* **116**, 241103 (Jun, 2016). doi: 10.1103/PhysRevLett.116.241103. URL <http://link.aps.org/doi/10.1103/PhysRevLett.116.241103>.
6. F. Özel, D. Psaltis, R. Narayan, and J. E. McClintock, The Black Hole Mass Distribution in the Galaxy, *Astrophysical Journal*. **725**, 1918–1927 (Dec., 2010). doi: 10.1088/0004-637X/725/2/1918.
7. B. S. Sathyaprakash and B. F. Schutz, Physics, Astrophysics and Cosmology with Gravitational Waves, *Living Reviews in Relativity*. **12** (Mar., 2009). doi: 10.12942/lrr-2009-2.
8. N. Andersson and et al., The transient gravitational-wave sky, *Classical and Quantum Gravity*. 30(19):193002 (Oct., 2013). doi: 10.1088/0264-9381/30/19/193002.
9. P. Amaro-Seoane, S. Aoudia, S. Babak, P. Binétruy, E. Berti, A. Bohé, C. Caprini, M. Colpi, N. J. Cornish, K. Danzmann, J.-F. Dufaux, J. Gair, I. Hinder, O. Jennrich, P. Jetzer, A. Klein, R. N. Lang, A. Lobo, T.ittenberg, S. T. McWilliams, G. Nelemans, A. Petiteau, E. K. Porter, B. F. Schutz, A. Sesana, R. Stebbins, T. Sumner, M. Vallisneri, S. Vitale, M. Volonteri, H. Ward, and B. Wardell, eLISA: Astrophysics and cosmology in the millihertz regime, *GW Notes, Vol. 6, p. 4-110*. **6**, 4–110 (May, 2013).

10. B. Sathyaprakash, M. Abernathy, F. Acernese, P. Ajith, B. Allen, P. Amaro-Seoane, N. Andersson, S. Aoudia, K. Arun, P. Astone, and et al., Scientific objectives of Einstein Telescope, *Classical and Quantum Gravity*. **29**(12):124013 (June, 2012). doi: 10.1088/0264-9381/29/12/124013.
11. C. W. Misner, K. S. Thorne, and J. A. Wheeler, *Gravitation* (1973).
12. R. P. Kerr, Gravitational Field of a Spinning Mass as an Example of Algebraically Special Metrics, *Physical Review Letters*. **11**, 237–238 (Sept., 1963). doi: 10.1103/PhysRevLett.11.237.
13. B. Carter, Global Structure of the Kerr Family of Gravitational Fields, *Physical Review*. **174**, 1559–1571 (Oct., 1968). doi: 10.1103/PhysRev.174.1559.
14. S. W. Hawking, Black holes in general relativity, *Communications in Mathematical Physics*. **25**, 152–166 (June, 1972). doi: 10.1007/BF01877517.
15. D. C. Robinson, Uniqueness of the Kerr black hole, *Physical Review Letters*. **34**, 905 (Apr., 1975). doi: 10.1103/PhysRevLett.34.905.
16. S. W. Hawking, Black hole explosions?, *Nature*. **248**, 30–31 (Mar., 1974). doi: 10.1038/248030a0.
17. S. L. Shapiro and S. A. Teukolsky, *Black Holes, White Dwarfs and Neutron Stars: The Physics of Compact Objects* (June, 1986).
18. J. M. Lattimer and M. Prakash, The equation of state of hot, dense matter and neutron stars, *Phys Rep.* **621**, 127–164 (Mar., 2016). doi: 10.1016/j.physrep.2015.12.005.
19. G. B. Cook, S. L. Shapiro, and S. A. Teukolsky, Rapidly rotating neutron stars in general relativity: Realistic equations of state, *Astrophysical Journal*. **424**, 823–845 (Apr., 1994). doi: 10.1086/173934.
20. T. W. Baumgarte, S. L. Shapiro, and M. Shibata, On the Maximum Mass of Differentially Rotating Neutron Stars, *Astrophysical Journal, Letters*. **528**, L29–L32 (Jan., 2000). doi: 10.1086/312425.
21. L. Baiotti and L. Rezzolla, Binary neutron-star mergers: a review of Einstein’s richest laboratory, *ArXiv e-prints* (July, 2016).
22. P. B. Demorest, T. Pennucci, S. M. Ransom, M. S. E. Roberts, and J. W. T. Hessels, A two-solar-mass neutron star measured using Shapiro delay, *Nature*. **467**, 1081–1083 (Oct., 2010). doi: 10.1038/nature09466.
23. T. Hosokawa, H. W. Yorke, K. Inayoshi, K. Omukai, and N. Yoshida, Formation of Primordial Supermassive Stars by Rapid Mass Accretion, *Astrophysical Journal*. **778**:178 (Dec., 2013). doi: 10.1088/0004-637X/778/2/178.

24. M. A. Latif and A. Ferrara, Formation of supermassive black hole seeds, *ArXiv e-prints* (May, 2016).
25. H. Ueda, T. Hosokawa, K. Omukai, and N. Yoshida, The Final Fates of Accreting Supermassive Stars, *ArXiv e-prints* (Sept., 2016).
26. A. Burrows, Colloquium: Perspectives on core-collapse supernova theory, *Reviews of Modern Physics*. **85**, 245–261 (Jan., 2013). doi: 10.1103/RevModPhys.85.245.
27. J. Antoniadis, T. M. Tauris, F. Ozel, E. Barr, D. J. Champion, and P. C. C. Freire, The millisecond pulsar mass distribution: Evidence for bimodality and constraints on the maximum neutron star mass, *ArXiv e-prints* (May, 2016).
28. F. Özel, D. Psaltis, R. Narayan, and A. Santos Villarreal, On the Mass Distribution and Birth Masses of Neutron Stars, *Astrophysical Journal*. 757:55 (Sept., 2012). doi: 10.1088/0004-637X/757/1/55.
29. B. P. Abbott, R. Abbott, T. D. Abbott, M. R. Abernathy, F. Acernese, K. Ackley, C. Adams, T. Adams, P. Addesso, R. X. Adhikari, and et al., Astrophysical Implications of the Binary Black-hole Merger GW150914, *Astrophysical Journal, Letters*. 818:L22 (Feb., 2016). doi: 10.3847/2041-8205/818/2/L22.
30. K. Belczynski, M. Dominik, T. Bulik, R. O’Shaughnessy, C. Fryer, and D. E. Holz, The Effect of Metallicity on the Detection Prospects for Gravitational Waves, *Astrophysical Journal, Letters*. **715**, L138–L141 (June, 2010). doi: 10.1088/2041-8205/715/2/L138.
31. M. Dominik, K. Belczynski, C. Fryer, D. E. Holz, E. Berti, T. Bulik, I. Mandel, and R. O’Shaughnessy, Double Compact Objects. I. The Significance of the Common Envelope on Merger Rates, *Astrophysical Journal*. 759:52 (Nov., 2012). doi: 10.1088/0004-637X/759/1/52.
32. M. Mapelli, M. Colpi, and L. Zampieri, Low metallicity and ultra-luminous X-ray sources in the Cartwheel galaxy, *Mon. Not. Roy. Astr. Soc.* **395**, L71–L75 (May, 2009). doi: 10.1111/j.1745-3933.2009.00645.x.
33. M. Spera, M. Mapelli, and A. Bressan, The mass spectrum of compact remnants from the PARSEC stellar evolution tracks, *Mon. Not. Roy. Astr. Soc.* **451**, 4086–4103 (Aug., 2015). doi: 10.1093/mnras/stv1161.
34. A. Heger and S. E. Woosley, The Nucleosynthetic Signature of Population III, *Astrophysical Journal*. **567**, 532–543 (Mar., 2002). doi: 10.1086/338487.
35. A. Heger, C. L. Fryer, S. E. Woosley, N. Langer, and D. H. Hartmann, How Massive Single Stars End Their Life, *Astrophysical Journal*. **591**, 288–300 (July, 2003). doi: 10.1086/375341.

36. W. Zhang, S. E. Woosley, and A. Heger, Fallback and Black Hole Production in Massive Stars, *Astrophysical Journal*. **679**:639–654 (May, 2008). doi: 10.1086/526404.
37. K. Belczynski, D. E. Holz, T. Bulik, and R. O’Shaughnessy, The first gravitational-wave source from the isolated evolution of two stars in the 40-100 solar mass range, *Nature*. **534**, 512–515 (June, 2016). doi: 10.1038/nature18322.
38. The LIGO Scientific Collaboration, the Virgo Collaboration, B. P. Abbott, R. Abbott, T. D. Abbott, M. R. Abernathy, F. Acernese, K. Ackley, C. Adams, T. Adams, and et al., Binary Black Hole Mergers in the first Advanced LIGO Observing Run, *ArXiv e-prints* (June, 2016).
39. A. V. Tutukov and L. R. Yungelson, The merger rate of neutron star and black hole binaries, *Mon. Not. Roy. Astr. Soc.*. **260**, 675–678 (Feb., 1993). doi: 10.1093/mnras/260.3.675.
40. J. A. Faber and F. A. Rasio, Binary Neutron Star Mergers, *Living Reviews in Relativity*. **15** (July, 2012). doi: 10.12942/lrr-2012-8.
41. R. A. Hulse and J. H. Taylor, Discovery of a pulsar in a binary system, *Astrophysical Journal, Letters*. **195**, L51–L53 (Jan., 1975). doi: 10.1086/181708.
42. J. H. Taylor and J. M. Weisberg, A new test of general relativity - Gravitational radiation and the binary pulsar PSR 1913+16, *Astrophysical Journal*. **253**, 908–920 (Feb., 1982). doi: 10.1086/159690.
43. D. Bhattacharya and E. P. J. van den Heuvel, Formation and evolution of binary and millisecond radio pulsars, *Phys Rep.* **203**, 1–124 (1991). doi: 10.1016/0370-1573(91)90064-S.
44. I. Mandel and S. E. de Mink, Merging binary black holes formed through chemically homogeneous evolution in short-period stellar binaries, *Mon. Not. Roy. Astr. Soc.*. **458**, 2634–2647 (May, 2016). doi: 10.1093/mnras/stw379.
45. M. Mapelli, Massive black hole binaries from runaway collisions: the impact of metallicity, *Mon. Not. Roy. Astr. Soc.*. **459**, 3432–3446 (July, 2016). doi: 10.1093/mnras/stw869.
46. C. L. Rodriguez, C.-J. Haster, S. Chatterjee, V. Kalogera, and F. A. Rasio, Dynamical Formation of the GW150914 Binary Black Hole, *ArXiv e-prints* (Apr., 2016).
47. M. J. Benacquista and J. M. B. Downing, Relativistic Binaries in Globular Clusters, *Living Reviews in Relativity*. **16** (Mar., 2013). doi: 10.12942/lrr-2013-4.

48. S. F. Portegies Zwart and S. L. W. McMillan, Black Hole Mergers in the Universe, *Astrophysical Journal, Letters.* **528**, L17–L20 (Jan., 2000). doi: 10.1086/312422.
49. N. C. Stone, B. D. Metzger, and Z. Haiman, Assisted Inspirals of Stellar Mass Black Holes Embedded in AGN Disks, *ArXiv e-prints* (Feb., 2016).
50. P. Marchant, N. Langer, P. Podsiadlowski, T. M. Tauris, and T. J. Moriya, A new route towards merging massive black holes, *Astronomy & Astrophysics.* 588:A50 (Apr., 2016). doi: 10.1051/0004-6361/201628133.
51. G. Hobbs, D. R. Lorimer, A. G. Lyne, and M. Kramer, A statistical study of 233 pulsar proper motions, *Mon. Not. Roy. Astr. Soc..* **360**, 974–992 (July, 2005). doi: 10.1111/j.1365-2966.2005.09087.x.
52. S. Repetto, M. B. Davies, and S. Sigurdsson, Investigating stellar-mass black hole kicks, *Mon. Not. Roy. Astr. Soc..* **425**, 2799–2809 (Oct., 2012). doi: 10.1111/j.1365-2966.2012.21549.x.
53. S. E. de Mink and I. Mandel, The chemically homogeneous evolutionary channel for binary black hole mergers: rates and properties of gravitational-wave events detectable by advanced LIGO, *Mon. Not. Roy. Astr. Soc..* **460**, 3545–3553 (Aug., 2016). doi: 10.1093/mnras/stw1219.
54. B. M. Ziosi, M. Mapelli, M. Branchesi, and G. Tormen, Dynamics of stellar black holes in young star clusters with different metallicities - II. Black hole-black hole binaries, *Mon. Not. Roy. Astr. Soc..* **441**, 3703–3717 (July, 2014). doi: 10.1093/mnras/stu824.
55. A. Merloni. Observing Supermassive Black Holes Across Cosmic Time: From Phenomenology to Physics. In eds. F. Haardt, V. Gorini, U. Moschella, A. Treves, and M. Colpi, *Lecture Notes in Physics, Berlin Springer Verlag*, vol. 905, *Lecture Notes in Physics, Berlin Springer Verlag*, p. 101 (2016). doi: 10.1007/978-3-319-19416-5__4.
56. J. Kormendy and L. C. Ho, Coevolution (Or Not) of Supermassive Black Holes and Host Galaxies, *ARA&A.* **51**, 511–653 (Aug., 2013). doi: 10.1146/annurev-astro-082708-101811.
57. R. Genzel, F. Eisenhauer, and S. Gillessen, The Galactic Center massive black hole and nuclear star cluster, *Reviews of Modern Physics.* **82**, 3121–3195 (Oct., 2010). doi: 10.1103/RevModPhys.82.3121.
58. A. E. Reines and M. Volonteri, Relations between Central Black Hole Mass and Total Galaxy Stellar Mass in the Local Universe, *Astrophysical Journal.* 813:82 (Nov., 2015). doi: 10.1088/0004-637X/813/2/82.
59. T. Sbarrato, G. Ghisellini, G. Tagliaferri, M. Perri, G. M. Madejski, D. Stern, S. E. Boggs, F. E. Christensen, W. W. Craig, C. J. Hailey, F. A. Harrison, and W. W. Zhang, Extremes of the jet-accretion power

- relation of blazars, as explored by NuSTAR, *Mon. Not. Roy. Astr. Soc.*. **462**, 1542–1550 (Oct., 2016). doi: 10.1093/mnras/stw1730.
- 60. K. S. Thorne, Disk-Accretion onto a Black Hole. II. Evolution of the Hole, *Astrophysical Journal*. **191**, 507–520 (July, 1974). doi: 10.1086/152991.
 - 61. C. F. Gammie, S. L. Shapiro, and J. C. McKinney, Black Hole Spin Evolution, *Astrophysical Journal*. **602**, 312–319 (Feb., 2004). doi: 10.1086/380996.
 - 62. J. M. Bardeen, Kerr Metric Black Holes, *Nature*. **226**, 64–65 (Apr., 1970). doi: 10.1038/226064a0.
 - 63. J. M. Bardeen and J. A. Petterson, The Lense-Thirring Effect and Accretion Disks around Kerr Black Holes, *Astrophysical Journal, Letters*. **195**, L65 (Jan., 1975). doi: 10.1086/181711.
 - 64. A. Perego, M. Dotti, M. Colpi, and M. Volonteri, Mass and spin co-evolution during the alignment of a black hole in a warped accretion disc, *Mon. Not. Roy. Astr. Soc.*. **399**, 2249–2263 (Nov., 2009). doi: 10.1111/j.1365-2966.2009.15427.x.
 - 65. A. Sesana, E. Barausse, M. Dotti, and E. M. Rossi, Linking the Spin Evolution of Massive Black Holes to Galaxy Kinematics, *Astrophysical Journal*. **794**:104 (Oct., 2014). doi: 10.1088/0004-637X/794/2/104.
 - 66. A. R. King, S. H. Lubow, G. I. Ogilvie, and J. E. Pringle, Aligning spinning black holes and accretion discs, *Mon. Not. Roy. Astr. Soc.*. **363**, 49–56 (Oct., 2005). doi: 10.1111/j.1365-2966.2005.09378.x.
 - 67. M. R. Krumholz, Notes on Star Formation, *ArXiv e-prints* (Nov., 2015).
 - 68. K. Belczynski, T. Bulik, C. L. Fryer, A. Ruiter, F. Valsecchi, J. S. Vink, and J. R. Hurley, On the Maximum Mass of Stellar Black Holes, *Astrophysical Journal*. **714**, 1217–1226 (May, 2010). doi: 10.1088/0004-637X/714/2/1217.
 - 69. K. Belczynski, A. Heger, W. Gladysz, A. J. Ruiter, S. Woosley, G. Wiktorowicz, H.-Y. Chen, T. Bulik, R. O’Shaughnessy, D. E. Holz, C. L. Fryer, and E. Berti, The Effect of Pair-Instability Mass Loss on Black Hole Mergers, *ArXiv e-prints* (July, 2016).
 - 70. M. Volonteri, Formation of supermassive black holes, *A&ARv*. **18**, 279–315 (July, 2010). doi: 10.1007/s00159-010-0029-x.
 - 71. S. E. Woosley, S. Blinnikov, and A. Heger, Pulsational pair instability as an explanation for the most luminous supernovae, *Nature*. **450**, 390–392 (Nov., 2007). doi: 10.1038/nature06333.

72. M. Limongi and A. Chieffi, Presupernova Evolution and Explosive Nucleosynthesis of Zero Metal Massive Stars, *Astrophysical Journal Supplements*. 199:38 (Apr., 2012). doi: 10.1088/0067-0049/199/2/38.
73. A. Loeb and S. R. Furlanetto, *The First Galaxies in the Universe* (2013).
74. L. Mayer, D. Fiacconi, S. Bonoli, T. Quinn, R. Roškar, S. Shen, and J. Wadsley, Direct Formation of Supermassive Black Holes in Metal-enriched Gas at the Heart of High-redshift Galaxy Mergers, *Astrophysical Journal*. 810:51 (Sept., 2015). doi: 10.1088/0004-637X/810/1/51.
75. A. Lupi, M. Colpi, B. Devecchi, G. Galanti, and M. Volonteri, Constraining the high-redshift formation of black hole seeds in nuclear star clusters with gas inflows, *Mon. Not. Roy. Astr. Soc.*. **442**, 3616–3626 (Aug., 2014). doi: 10.1093/mnras/stu1120.
76. A. Lupi, F. Haardt, M. Dotti, D. Fiacconi, L. Mayer, and P. Madau, Growing massive black holes through supercritical accretion of stellar-mass seeds, *Mon. Not. Roy. Astr. Soc.*. **456**, 2993–3003 (Mar., 2016). doi: 10.1093/mnras/stv2877.
77. S. F. Portegies Zwart and S. L. W. McMillan, The Runaway Growth of Intermediate-Mass Black Holes in Dense Star Clusters, *Astrophysical Journal*. **576**, 899–907 (Sept., 2002). doi: 10.1086/341798.
78. B. Devecchi, M. Volonteri, E. M. Rossi, M. Colpi, and S. Portegies Zwart, High-redshift formation and evolution of central massive objects - II. The census of BH seeds, *Mon. Not. Roy. Astr. Soc.*. **421**, 1465–1475 (Apr., 2012). doi: 10.1111/j.1365-2966.2012.20406.x.
79. M. C. Begelman, Evolution of supermassive stars as a pathway to black hole formation, *Mon. Not. Roy. Astr. Soc.*. **402**, 673–681 (Feb., 2010). doi: 10.1111/j.1365-2966.2009.15916.x.
80. D. Fiacconi and E. M. Rossi, Light or heavy supermassive black hole seeds: the role of internal rotation in the fate of supermassive stars, *ArXiv e-prints* (Apr., 2016).
81. Planck Collaboration, P. A. R. Ade, N. Aghanim, C. Armitage-Caplan, M. Arnaud, M. Ashdown, F. Atrio-Barandela, J. Aumont, C. Baccigalupi, A. J. Banday, and et al., Planck 2013 results. XVI. Cosmological parameters, *Astronomy & Astrophysics*. 571:A16 (Nov., 2014). doi: 10.1051/0004-6361/201321591.
82. P. Madau and M. Dickinson, Cosmic Star-Formation History, *ARA&A*. **52**, 415–486 (Aug., 2014). doi: 10.1146/annurev-astro-081811-125615.
83. Planck Collaboration, Planck intermediate results. XLVII. Planck constraints on reionization history, *ArXiv e-prints* (May, 2016).

84. M. Volonteri and P. Natarajan, Journey to the $M_{BH}-\sigma$ relation: the fate of low-mass black holes in the Universe, *Mon. Not. Roy. Astr. Soc.*. **400**, 1911–1918 (Dec., 2009). doi: 10.1111/j.1365-2966.2009.15577.x.
85. M. Colpi, Massive Binary Black Holes in Galactic Nuclei and Their Path to Coalescence, *Space Science Reviews*. **183**, 189–221 (Sept., 2014). doi: 10.1007/s11214-014-0067-1.
86. F. M. Khan, D. Fiacconi, L. Mayer, P. Berczik, and A. Just, Swift coalescence of supermassive black holes in cosmological mergers of massive galaxies, *ArXiv e-prints* (Mar., 2016).
87. Y. Zlochower, M. Campanelli, and C. O. Lousto, Modeling gravitational recoil from black-hole binaries using numerical relativity, *Classical and Quantum Gravity*. **28**(11):114015 (June, 2011). doi: 10.1088/0264-9381/28/11/114015.
88. D. Fiacconi, L. Mayer, R. Roškar, and M. Colpi, Massive Black Hole Pairs in Clumpy, Self-gravitating Circumnuclear Disks: Stochastic Orbital Decay, *Astrophysical Journal, Letters*. **777**:L14 (Nov., 2013). doi: 10.1088/2041-8205/777/1/L14.
89. A. Sesana, M. Volonteri, and F. Haardt, The imprint of massive black hole formation models on the LISA data stream, *Mon. Not. Roy. Astr. Soc.*. **377**, 1711–1716 (June, 2007). doi: 10.1111/j.1365-2966.2007.11734.x.
90. D. V. Martynov, E. D. Hall, B. P. Abbott, R. Abbott, T. D. Abbott, C. Adams, R. X. Adhikari, R. A. Anderson, S. B. Anderson, K. Arai, and et al., Sensitivity of the Advanced LIGO detectors at the beginning of gravitational wave astronomy, *Phys. Rev. D*. **93**(11):112004 (June, 2016). doi: 10.1103/PhysRevD.93.112004.
91. J. Abadie, B. P. Abbott, R. Abbott, T. D. Abbott, M. Abernathy, T. Accadia, F. Acernese, C. Adams, R. Adhikari, C. Affeldt, and et al., Search for gravitational waves from low mass compact binary coalescence in LIGO’s sixth science run and Virgo’s science runs 2 and 3, *Phys. Rev. D*. **85**(8): 082002 (Apr., 2012). doi: 10.1103/PhysRevD.85.082002.
92. B. P. Abbott, R. Abbott, T. D. Abbott, M. R. Abernathy, F. Acernese, K. Ackley, C. Adams, T. Adams, P. Addesso, R. X. Adhikari, and et al., The Rate of Binary Black Hole Mergers Inferred from Advanced LIGO Observations Surrounding GW150914, *ArXiv e-prints* (Feb., 2016).
93. J. Abadie, B. P. Abbott, R. Abbott, M. Abernathy, T. Accadia, F. Acernese, C. Adams, R. Adhikari, P. Ajith, B. Allen, and et al., TOPICAL REVIEW: Predictions for the rates of compact binary coalescences observable by ground-based gravitational-wave detectors, *Classical and Quantum Gravity*. **27**(17):173001 (Sept., 2010). doi: 10.1088/0264-9381/27/17/173001.

94. C. D. Ott, TOPICAL REVIEW: The gravitational-wave signature of core-collapse supernovae, *Classical and Quantum Gravity*. 26(6):063001 (Mar., 2009). doi: 10.1088/0264-9381/26/6/063001.
95. C. L. Fryer and K. C. B. New, Gravitational Waves from Gravitational Collapse, *Living Reviews in Relativity*. 14 (Jan., 2011). doi: 10.12942/lrr-2011-1.
96. N. Andersson, TOPICAL REVIEW: Gravitational waves from instabilities in relativistic stars, *Classical and Quantum Gravity*. 20, R105–R144 (Apr., 2003).
97. L. Stella, S. Dall’Osso, G. L. Israel, and A. Vecchio, Gravitational Radiation from Newborn Magnetars in the Virgo Cluster, *Astrophysical Journal, Letters*. 634, L165–L168 (Dec., 2005). doi: 10.1086/498685.
98. N. Andersson, V. Ferrari, D. I. Jones, K. D. Kokkotas, B. Krishnan, J. S. Read, L. Rezzolla, and B. Zink, Gravitational waves from neutron stars: promises and challenges, *General Relativity and Gravitation*. 43, 409–436 (Feb., 2011). doi: 10.1007/s10714-010-1059-4.
99. B. P. Abbott, R. Abbott, F. Acernese, R. Adhikari, P. Ajith, B. Allen, G. Allen, M. Alshourbagy, R. S. Amin, S. B. Anderson, and et al., Searches for Gravitational Waves from Known Pulsars with Science Run 5 LIGO Data, *Astrophysical Journal*. 713, 671–685 (Apr., 2010). doi: 10.1088/0004-637X/713/1/671.
100. B. Abbott, R. Abbott, R. Adhikari, P. Ajith, B. Allen, G. Allen, R. Amin, S. B. Anderson, W. G. Anderson, M. A. Arain, and et al., Beating the Spin-Down Limit on Gravitational Wave Emission from the Crab Pulsar, *Astrophysical Journal, Letters*. 683:L45 (Aug., 2008). doi: 10.1086/591526.
101. B. P. Abbott, R. Abbott, T. D. Abbott, M. R. Abernathy, F. Acernese, K. Ackley, C. Adams, T. Adams, P. Addesso, R. X. Adhikari, and et al., GW150914: Implications for the Stochastic Gravitational-Wave Background from Binary Black Holes, *Physical Review Letters*. 116(13):131102 (Apr., 2016). doi: 10.1103/PhysRevLett.116.131102.
102. eLISA Consortium, The Gravitational Universe, *ArXiv e-prints* (May, 2013).
103. A. Sesana, J. Gair, E. Berti, and M. Volonteri, Reconstructing the massive black hole cosmic history through gravitational waves, *Phys. Rev. D*. 83 (4):044036 (Feb., 2011). doi: 10.1103/PhysRevD.83.044036.
104. E. Berti and M. Volonteri, Cosmological Black Hole Spin Evolution by Mergers and Accretion, *Astrophysical Journal*. 684:822–828 (Sept., 2008). doi: 10.1086/590379.

105. E. Berti, E. Barausse, V. Cardoso, L. Gualtieri, P. Pani, U. Sperhake, L. C. Stein, N. Wex, K. Yagi, T. Baker, C. P. Burgess, F. S. Coelho, D. Doneva, A. De Felice, P. G. Ferreira, P. C. C. Freire, J. Healy, C. Herdeiro, M. Horbatsch, B. Kleihaus, A. Klein, K. Kokkotas, J. Kunz, P. Laguna, R. N. Lang, T. G. F. Li, T. Littenberg, A. Matas, S. Mirshekari, H. Okawa, E. Radu, R. O'Shaughnessy, B. S. Sathyaprakash, C. Van Den Broeck, H. A. Winther, H. Witek, M. Emad Aghili, J. Alsing, B. Bolen, L. Bombelli, S. Caudill, L. Chen, J. C. Degollado, R. Fujita, C. Gao, D. Gerosa, S. Kamali, H. O. Silva, J. G. Rosa, L. Sadeghian, M. Sampaio, H. Sotani, and M. Zilhao, Testing general relativity with present and future astrophysical observations, *Classical and Quantum Gravity*. 32(24): 243001 (Dec., 2015). doi: 10.1088/0264-9381/32/24/243001.
106. E. Berti, A. Sesana, E. Barausse, V. Cardoso, and K. Belczynski, Spectroscopy of Kerr black holes with Earth- and space-based interferometers, *ArXiv e-prints* (May, 2016).
107. M. Colpi, S. L. Shapiro, and I. Wasserman, Boson stars - Gravitational equilibria of self-interacting scalar fields, *Physical Review Letters*. **57**, 2485–2488 (Nov., 1986). doi: 10.1103/PhysRevLett.57.2485.
108. N. Tamanini, C. Caprini, E. Barausse, A. Sesana, A. Klein, and A. Pettiteau, Science with the space-based interferometer eLISA. III: probing the expansion of the universe using gravitational wave standard sirens, *Journal of Cosmology and Astroparticle Physics*. 4:002 (Apr., 2016). doi: 10.1088/1475-7516/2016/04/002.
109. J. D. Schnittman, Electromagnetic counterparts to black hole mergers, *Classical and Quantum Gravity*. 28(9):094021 (May, 2011). doi: 10.1088/0264-9381/28/9/094021.
110. T. Bogdanović, Supermassive Black Hole Binaries: The Search Continues, *Astrophysics and Space Science Proceedings*. **40**, 103 (2015). doi: 10.1007/978-3-319-10488-1_9.
111. P. Amaro-Seoane, J. R. Gair, M. Freitag, M. C. Miller, I. Mandel, C. J. Cutler, and S. Babak, TOPICAL REVIEW: Intermediate and extreme mass-ratio inspirals astrophysics, science applications and detection using LISA, *Classical and Quantum Gravity*. **24**, R113–R169 (Sept., 2007). doi: 10.1088/0264-9381/24/17/R01.
112. M. J. Rees, Tidal disruption of stars by black holes of 10 to the 6th-10 to the 8th solar masses in nearby galaxies, *Nature*. **333**, 523–528 (June, 1988). doi: 10.1038/333523a0.
113. C. Hopman and T. Alexander, The Effect of Mass Segregation on Gravitational Wave Sources near Massive Black Holes, *Astrophysical Journal, Letters*. **645**, L133–L136 (July, 2006). doi: 10.1086/506273.

114. D. Merritt, T. Alexander, S. Mikkola, and C. M. Will, Stellar dynamics of extreme-mass-ratio inspirals, *Phys. Rev. D.* **84**(4):044024 (Aug., 2011). doi: 10.1103/PhysRevD.84.044024.
115. D. Merritt, Loss-cone dynamics, *Classical and Quantum Gravity.* **30**(24): 244005 (Dec., 2013). doi: 10.1088/0264-9381/30/24/244005.
116. P. Amaro-Seoane, Stellar dynamics and extreme-mass ratio inspirals, *ArXiv e-prints* (May, 2012).
117. P. Amaro-Seoane, C. F. Sopuerta, and M. D. Freitag, The role of the supermassive black hole spin in the estimation of the EMRI event rate, *Mon. Not. Roy. Astr. Soc..* **429**, 3155–3165 (Mar., 2013). doi: 10.1093/mnras/sts572.
118. P. Amaro-Seoane and et al., Low-frequency gravitational-wave science with eLISA/NGO, *Classical and Quantum Gravity.* **29**(12):124016 (June, 2012). doi: 10.1088/0264-9381/29/12/124016.
119. C. Caprini, M. Hindmarsh, S. Huber, T. Konstandin, J. Kozaczuk, G. Nardini, J. M. No, A. Petiteau, P. Schwaller, G. Servant, and D. J. Weir, Science with the space-based interferometer eLISA. II: gravitational waves from cosmological phase transitions, *Journal of Cosmology and Astroparticle Physics.* **4**:001 (Apr., 2016). doi: 10.1088/1475-7516/2016/04/001.
120. L. Lentati, S. R. Taylor, C. M. F. Mingarelli, A. Sesana, S. A. Sanidas, A. Vecchio, R. N. Caballero, K. J. Lee, R. van Haasteren, S. Babak, C. G. Bassa, P. Brem, M. Burgay, D. J. Champion, I. Cognard, G. Desvignes, J. R. Gair, L. Guillemot, J. W. T. Hessels, G. H. Janssen, R. Karuppusamy, M. Kramer, A. Lassus, P. Lazarus, K. Liu, S. Osłowski, D. Perrodin, A. Petiteau, A. Possenti, M. B. Purver, P. A. Rosado, R. Smits, B. Stappers, G. Theureau, C. Tiburzi, and J. P. W. Verbiest, European Pulsar Timing Array limits on an isotropic stochastic gravitational-wave background, *Mon. Not. Roy. Astr. Soc..* **453**, 2576–2598 (Nov., 2015). doi: 10.1093/mnras/stv1538.
121. R. M. Shannon, V. Ravi, L. T. Lentati, P. D. Lasky, G. Hobbs, M. Kerr, R. N. Manchester, W. A. Coles, Y. Levin, M. Bailes, N. D. R. Bhat, S. Burke-Spolaor, S. Dai, M. J. Keith, S. Osłowski, D. J. Reardon, W. van Straten, L. Toomey, J.-B. Wang, L. Wen, J. S. B. Wyithe, and X.-J. Zhu, Gravitational waves from binary supermassive black holes missing in pulsar observations, *Science.* **349**, 1522–1525 (Sept., 2015). doi: 10.1126/science.aab1910.
122. Z. Arzoumanian, A. Brazier, S. Burke-Spolaor, S. J. Chamberlin, S. Chatterjee, B. Christy, J. M. Cordes, N. J. Cornish, K. Crowter, P. B. Demorest, X. Deng, T. Dolch, J. A. Ellis, R. D. Ferdman, E. Fonseca, N. Garver-Daniels, M. E. Gonzalez, F. Jenet, G. Jones, M. L. Jones, V. M. Kaspi, M. Koop, M. T. Lam, T. J. W. Lazio, L. Levin, A. N. Lommen,

- D. R. Lorimer, J. Luo, R. S. Lynch, D. R. Madison, M. A. McLaughlin, S. T. McWilliams, C. M. F. Mingarelli, D. J. Nice, N. Palliyaguru, T. T. Pennucci, S. M. Ransom, L. Sampson, S. A. Sanidas, A. Sesana, X. Siemens, J. Simon, I. H. Stairs, D. R. Stinebring, K. Stovall, J. Swiggum, S. R. Taylor, M. Vallisneri, R. van Haasteren, Y. Wang, W. W. Zhu, and NANOGrav Collaboration, The NANOGrav Nine-year Data Set: Limits on the Isotropic Stochastic Gravitational Wave Background, *Astrophysical Journal*. 821:13 (Apr., 2016). doi: 10.3847/0004-637X/821/1/13.
123. J. P. W. Verbiest, L. Lentati, G. Hobbs, R. van Haasteren, P. B. Demorest, G. H. Janssen, J.-B. Wang, G. Desvignes, R. N. Caballero, M. J. Keith, D. J. Champion, Z. Arzoumanian, S. Babak, C. G. Bassa, N. D. R. Bhat, A. Brazier, P. Brem, M. Burgay, S. Burke-Spolaor, S. J. Chamberlin, S. Chatterjee, B. Christy, I. Cognard, J. M. Cordes, S. Dai, T. Dolch, J. A. Ellis, R. D. Ferdman, E. Fonseca, J. R. Gair, N. E. Garver-Daniels, P. Gentile, M. E. Gonzalez, E. Graikou, L. Guillemot, J. W. T. Hessels, G. Jones, R. Karuppusamy, M. Kerr, M. Kramer, M. T. Lam, P. D. Lasky, A. Lassus, P. Lazarus, T. J. W. Lazio, K. J. Lee, L. Levin, K. Liu, R. S. Lynch, A. G. Lyne, J. McKee, M. A. McLaughlin, S. T. McWilliams, D. R. Madison, R. N. Manchester, C. M. F. Mingarelli, D. J. Nice, S. Osłowski, N. T. Palliyaguru, T. T. Pennucci, B. B. P. Perera, D. Perrodin, A. Possenti, A. Petiteau, S. M. Ransom, D. Reardon, P. A. Rosado, S. A. Sanidas, A. Sesana, G. Shaifullah, R. M. Shannon, X. Siemens, J. Simon, R. Smits, R. Spiewak, I. H. Stairs, B. W. Stappers, D. R. Stinebring, K. Stovall, J. K. Swiggum, S. R. Taylor, G. Theureau, C. Tiburzi, L. Toomey, M. Vallisneri, W. van Straten, A. Vecchio, Y. Wang, L. Wen, X. P. You, W. W. Zhu, and X.-J. Zhu, The International Pulsar Timing Array: First data release, *Mon. Not. Roy. Astr. Soc.*. **458**, 1267–1288 (May, 2016). doi: 10.1093/mnras/stw347.
124. A. Sesana, Insights into the astrophysics of supermassive black hole binaries from pulsar timing observations, *Classical and Quantum Gravity*. 30 (22):224014 (Nov., 2013). doi: 10.1088/0264-9381/30/22/224014.
125. D. Merritt, Mass Deficits, Stalling Radii, and the Merger Histories of Elliptical Galaxies, *Astrophysical Journal*. **648**, 976–986 (Sept., 2006). doi: 10.1086/506139.
126. J. Shangguan, X. Liu, L. C. Ho, Y. Shen, C. Y. Peng, J. E. Greene, and M. A. Strauss, Chandra X-Ray and Hubble Space Telescope Imaging of Optically Selected Kiloparsec-scale Binary Active Galactic Nuclei. II. Host Galaxy Morphology and AGN Activity, *Astrophysical Journal*. 823: 50 (May, 2016). doi: 10.3847/0004-637X/823/1/50.
127. E. Poisson and C. M. Will, *Gravity* (May, 2014).
128. N. Yunes and X. Siemens, Gravitational-Wave Tests of General Relativity with Ground-Based Detectors and Pulsar-Timing Arrays, *Living Reviews in Relativity*. **16** (Nov., 2013). doi: 10.12942/lrr-2013-9.

129. A. Buonanno and T. Damour, Effective one-body approach to general relativistic two-body dynamics, *Phys. Rev. D.* **59**(8):084006 (Apr., 1999). doi: 10.1103/PhysRevD.59.084006.
130. T. Damour and A. Nagar. The Effective-One-Body Approach to the General Relativistic Two Body Problem. In eds. F. Haardt, V. Gorini, U. Moschella, A. Treves, and M. Colpi, *Lecture Notes in Physics, Berlin Springer Verlag*, vol. 905, *Lecture Notes in Physics, Berlin Springer Verlag*, p. 273 (2016). doi: 10.1007/978-3-319-19416-5_-7.
131. M. Hannam, P. Schmidt, A. Bohé, L. Haegel, S. Husa, F. Ohme, G. Pratten, and M. Pürer, Simple Model of Complete Precessing Black-Hole-Binary Gravitational Waveforms, *Physical Review Letters*. **113**(15):151101 (Oct., 2014). doi: 10.1103/PhysRevLett.113.151101.
132. S. Husa, S. Khan, M. Hannam, M. Pürer, F. Ohme, X. J. Forteza, and A. Bohé, Frequency-domain gravitational waves from nonprecessing black-hole binaries. I. New numerical waveforms and anatomy of the signal, *Phys. Rev. D.* **93**(4):044006 (Feb., 2016). doi: 10.1103/PhysRevD.93.044006.
133. S. Bernuzzi, A. Nagar, T. Dietrich, and T. Damour, Modeling the Dynamics of Tidally Interacting Binary Neutron Stars up to the Merger, *Physical Review Letters*. **114**(16):161103 (Apr., 2015). doi: 10.1103/PhysRevLett.114.161103.
134. F. Ohme, Analytical meets numerical relativity: status of complete gravitational waveform models for binary black holes, *Classical and Quantum Gravity*. **29**(12):124002 (June, 2012). doi: 10.1088/0264-9381/29/12/124002.
135. L. Blanchet, Gravitational Radiation from Post-Newtonian Sources and Inspiralling Compact Binaries, *Living Reviews in Relativity*. **17** (Feb., 2014). doi: 10.12942/lrr-2014-2.
136. A. Buonanno and B. S. Sathyaprakash, Sources of Gravitational Waves: Theory and Observations, *ArXiv e-prints* (Oct., 2014).
137. S. Nissanke, D. E. Holz, N. Dalal, S. A. Hughes, J. L. Sievers, and C. M. Hirata, Determining the Hubble constant from gravitational wave observations of merging compact binaries, *ArXiv e-prints* (July, 2013).
138. B. F. Schutz, Determining the Hubble constant from gravitational wave observations, *Nature*. **323**, 310 (Sept., 1986). doi: 10.1038/323310a0.
139. M. Dotti, M. Volonteri, A. Perego, M. Colpi, M. Ruszkowski, and F. Haardt, Dual black holes in merger remnants - II. Spin evolution and gravitational recoil, *Mon. Not. Roy. Astr. Soc.*. **402**, 682–690 (Feb., 2010). doi: 10.1111/j.1365-2966.2009.15922.x.

140. T. Bogdanović, C. S. Reynolds, and M. C. Miller, Alignment of the Spins of Supermassive Black Holes Prior to Coalescence, *Astrophysical Journal, Letters.* **661**, L147–L150 (June, 2007). doi: 10.1086/518769.
141. M. C. Miller and J. H. Krolik, Alignment of Supermassive Black Hole Binary Orbits and Spins, *Astrophysical Journal.* 774:43 (Sept., 2013). doi: 10.1088/0004-637X/774/1/43.
142. J. D. Schnittman, Spin-orbit resonance and the evolution of compact binary systems, *Phys. Rev. D.* 70(12):124020 (Dec., 2004). doi: 10.1103/PhysRevD.70.124020.
143. M. Kesden, U. Sperhake, and E. Berti, Final spins from the merger of precessing binary black holes, *Phys. Rev. D.* 81(8):084054 (Apr., 2010). doi: 10.1103/PhysRevD.81.084054.
144. D. Gerosa, M. Kesden, R. O’Shaughnessy, A. Klein, E. Berti, U. Sperhake, and D. Trifirò, Precessional Instability in Binary Black Holes with Aligned Spins, *Physical Review Letters.* 115(14):141102 (Oct., 2015). doi: 10.1103/PhysRevLett.115.141102.
145. C. O. Lousto and J. Healy, Unstable flip-flopping spinning binary black holes, *Phys. Rev. D.* 93(12):124074 (June, 2016). doi: 10.1103/PhysRevD.93.124074.
146. C. O. Lousto and Y. Zlochower, Black hole binary remnant mass and spin: A new phenomenological formula, *Phys. Rev. D.* 89(10):104052 (May, 2014). doi: 10.1103/PhysRevD.89.104052.
147. C. O. Lousto and Y. Zlochower, Further insight into gravitational recoil, *Phys. Rev. D.* 77(4):044028 (Feb., 2008). doi: 10.1103/PhysRevD.77.044028.
148. C. O. Lousto and Y. Zlochower, Hangup Kicks: Still Larger Recoils by Partial Spin-Orbit Alignment of Black-Hole Binaries, *Physical Review Letters.* 107(23):231102 (Dec., 2011). doi: 10.1103/PhysRevLett.107.231102.
149. A. Gualandris and D. Merritt, Ejection of Supermassive Black Holes from Galaxy Cores, *Astrophysical Journal.* 678:780-797 (May, 2008). doi: 10.1086/586877.
150. S. Komossa, Recoiling Black Holes: Electromagnetic Signatures, Candidates, and Astrophysical Implications, *Advances in Astronomy.* 2012: 364973 (2012). doi: 10.1155/2012/364973.
151. L. Rezzolla, Modelling the final state from binary black-hole coalescences, *Classical and Quantum Gravity.* 26(9):094023 (May, 2009). doi: 10.1088/0264-9381/26/9/094023.

152. L. Rezzolla. An Introduction to Astrophysical Black Holes and Their Dynamical Production. In eds. F. Haardt, V. Gorini, U. Moschella, A. Treves, and M. Colpi, *Lecture Notes in Physics, Berlin Springer Verlag*, vol. 905, *Lecture Notes in Physics, Berlin Springer Verlag*, p. 1 (2016). doi: 10.1007/978-3-319-19416-5__1.
153. F. Hofmann, E. Barausse, and L. Rezzolla, The Final Spin from Binary Black Holes in Quasi-circular Orbits, *Astrophysical Journal, Letters*. 825: L19 (July, 2016). doi: 10.3847/2041-8205/825/2/L19.
154. The LIGO Scientific Collaboration, the Virgo Collaboration, B. P. Abbott, R. Abbott, T. D. Abbott, M. R. Abernathy, F. Acernese, K. Ackley, C. Adams, T. Adams, and et al., An improved analysis of GW150914 using a fully spin-precessing waveform model, *ArXiv e-prints* (June, 2016).
155. E. Barausse, V. Morozova, and L. Rezzolla, On the Mass Radiated by Coalescing Black Hole Binaries, *Astrophysical Journal*. 758:63 (Oct., 2012). doi: 10.1088/0004-637X/758/1/63.
156. C. Reisswig, S. Husa, L. Rezzolla, E. N. Dorband, D. Pollney, and J. Seiler, Gravitational-wave detectability of equal-mass black-hole binaries with aligned spins, *Phys. Rev. D*. 80(12):124026 (Dec., 2009). doi: 10.1103/PhysRevD.80.124026.
157. J. R. Gair, M. Vallisneri, S. L. Larson, and J. G. Baker, Testing General Relativity with Low-Frequency, Space-Based Gravitational-Wave Detectors, *Living Reviews in Relativity*. **16** (Sept., 2013).
158. A. Endrizzi, R. Ciolfi, B. Giacomazzo, W. Kastaun, and T. Kawamura, General Relativistic Magnetohydrodynamic Simulations of Binary Neutron Star Mergers with the APR4 Equation of State, *ArXiv e-prints* (Apr., 2016).
159. T. Binnington and E. Poisson, Relativistic theory of tidal Love numbers, *Phys. Rev. D*. 80(8):084018 (Oct., 2009). doi: 10.1103/PhysRevD.80.084018.
160. T. Damour, A. Nagar, and L. Villain, Measurability of the tidal polarizability of neutron stars in late-inspiral gravitational-wave signals, *Phys. Rev. D*. 85(12):123007 (June, 2012). doi: 10.1103/PhysRevD.85.123007.
161. K. Takami, L. Rezzolla, and L. Baiotti, Constraining the Equation of State of Neutron Stars from Binary Mergers, *Physical Review Letters*. 113(9): 091104 (Aug., 2014). doi: 10.1103/PhysRevLett.113.091104.
162. S. Bernuzzi, T. Dietrich, and A. Nagar, Modeling the Complete Gravitational Wave Spectrum of Neutron Star Mergers, *Physical Review Letters*. 115(9):091101 (Aug., 2015). doi: 10.1103/PhysRevLett.115.091101.

163. V. Paschalidis, M. Ruiz, and S. L. Shapiro, Relativistic Simulations of Black Hole-Neutron Star Coalescence: The Jet Emerges, *Astrophysical Journal, Letters.* 806:L14 (June, 2015). doi: 10.1088/2041-8205/806/1/L14.
164. M. Ruiz, R. N. Lang, V. Paschalidis, and S. L. Shapiro, Binary Neutron Star Mergers: A Jet Engine for Short Gamma-Ray Bursts, *Astrophysical Journal, Letters.* 824:L6 (June, 2016). doi: 10.3847/2041-8205/824/1/L6.
165. E. Berger, Short-Duration Gamma-Ray Bursts, *ARA&A.* **52**, 43–105 (Aug., 2014). doi: 10.1146/annurev-astro-081913-035926.
166. L.-X. Li and B. Paczyński, Transient Events from Neutron Star Mergers, *Astrophysical Journal, Letters.* **507**, L59–L62 (Nov., 1998). doi: 10.1086/311680.
167. E. Nakar and T. Piran, Detectable radio flares following gravitational waves from mergers of binary neutron stars, *Nature.* **478**, 82–84 (Oct., 2011). doi: 10.1038/nature10365.
168. S. E. Gossan, P. Sutton, A. Stuver, M. Zanolin, K. Gill, and C. D. Ott, Observing gravitational waves from core-collapse supernovae in the advanced detector era, *Phys. Rev. D.* 93(4):042002 (Feb., 2016). doi: 10.1103/PhysRevD.93.042002.
169. A. Sesana, A. Vecchio, and C. N. Colacino, The stochastic gravitational-wave background from massive black hole binary systems: implications for observations with Pulsar Timing Arrays, *Mon. Not. Roy. Astr. Soc..* **390**, 192–209 (Oct., 2008). doi: 10.1111/j.1365-2966.2008.13682.x.
170. G. Janssen, G. Hobbs, M. McLaughlin, C. Bassa, A. Deller, M. Kramer, K. Lee, C. Mingarelli, P. Rosado, S. Sanidas, A. Sesana, L. Shao, I. Stairs, B. Stappers, and J. P. W. Verbiest, Gravitational Wave Astronomy with the SKA, *Advancing Astrophysics with the Square Kilometre Array (AASKA14)*. art. 37 (2015).
171. A. Petiteau, S. Babak, A. Sesana, and M. de Araújo, Resolving multiple supermassive black hole binaries with pulsar timing arrays. II. Genetic algorithm implementation, *Phys. Rev. D.* 87(6):064036 (Mar., 2013). doi: 10.1103/PhysRevD.87.064036.
172. B. P. Abbott, R. Abbott, T. D. Abbott, M. R. Abernathy, F. Acernese, K. Ackley, C. Adams, T. Adams, P. Addesso, R. X. Adhikari, and et al., GW150914: The Advanced LIGO Detectors in the Era of First Discoveries, *Physical Review Letters.* 116(13):131103 (Apr., 2016). doi: 10.1103/PhysRevLett.116.131103.
173. M. Armano and et al., Sub-Femto-g Free Fall for Space-Based Gravitational Wave Observatories: LISA Pathfinder Results, *Physical Review Letters.* 116(23):231101 (June, 2016). doi: 10.1103/PhysRevLett.116.231101.

174. A. Sesana, The promise of multi-band gravitational wave astronomy, *ArXiv e-prints* (Feb., 2016).
175. A. Klein, E. Barausse, A. Sesana, A. Petiteau, E. Berti, S. Babak, J. Gair, S. Aoudia, I. Hinder, F. Ohme, and B. Wardell, Science with the space-based interferometer eLISA: Supermassive black hole binaries, *Phys. Rev. D* 93(2):024003 (Jan., 2016). doi: 10.1103/PhysRevD.93.024003.